A FUNDAMENTAL STUDY OF ADVANCE RATIO, SOLIDITY, TURBINE RADIUS, AND BLADE PROFILE ON THE PERFORMANCE CHARACTERISTICS OF VERTICAL AXIS TURBINES (VATs)

Adam Norman

Thesis submitted to the faculty of the Virginia Polytechnic Institute and State University in partial fulfillment of the requirements for the degree of

Master of Science

in

Mechanical Engineering

Danesh K. Tafti – Chair

Francine Battaglia

Lei Zuo

June 29th, 2016

Blacksburg, Virginia, USA

Keywords: Computational Fluid Dynamics (CFD), Reynolds Averaged Navier-Stokes (RANS), Large Eddy Simulation (LES) vertical axis turbine, dynamics stall, advance ratio, solidity, wake

A FUNDAMENTAL STUDY OF ADVANCE RATIO, SOLIDITY, TURBINE RADIUS, AND BLADE PROFILE ON THE PERFORMANCE CHARACTERISTICS OF VERTICAL AXIS TURBINES (VATs)

Adam Norman

Abstract

In this dissertation, various VAT parameters are investigated to determine the effect of the overall efficiency of the turbine at a high Reynolds number. To increase the efficiency of the vertical axis turbines, 2D CFD simulations are completed in an effort to better understand the physics behind the operation of these turbines. Specifically, the effect of advance ratio, solidity, and wake interactions were investigated. Simulations were completed in OpenFOAM using the k-ω SST turbulence model at a nominal Reynolds number of 500,000 using a NACA 0015 airfoil. To simulate the motion of the turbine, Arbitrary Mesh Interfacing (AMI) was used. For all of the parameters tested, it was found that the geometric effective angle of attack seen by the turbine blades had a significant impact on the power extracted from the flow. The range of effective angles of attack was found to decrease as the advance ratio increased. In spite of this, a severe loss in the power coefficient occurred at an advance ratio of 2.5 during which the blade experienced dynamic stall. This effect was also seen when the number of turbine blades was changed to four, at a solidity of 1.08. This negative impact on performance was found to be due to the increase in the drag component of the tangential force when dynamic stall occurs. Results indicate that wake interactions between subsequent blades have a large impact on performance especially when the wake interaction alters the flow direction sufficiently to create conditions for dynamic stall.

To improve the performance of the VAT in the presence of dynamic stall, calculations were completed of a static twisted blade profile using GenIDLEST and OpenFOAM. There was found to be no improvement in the lift coefficient when comparing the twisted blade profile with a 2D blade at the same median angle of attack as the twisted blade. To further see the effects of the twisted blade, an effective

VAT pitching motion was given to the blade and again compared to a 2D blade with the same motion. In this case there was significant improvement seen in the performance of the twisted blade.

Dedicated to Mom, Dad, and Michael

Acknowledgements

First, I would like to use this opportunity to thank Dr. Danesh Tafti for outstanding guidance, patience, motivation and for providing me with the tools to succeed in my research. In the past two years he has been a great source of knowledge and insight, and has always made himself available for any questions and discussion. Without his guidance and continued support, this dissertation would not be possible.

I would also like to thank Dr. Francine Battaglia and Dr. Lei Zou for taking time from their busy schedules to be on my committee and for reviewing my work.

I would also like to thank all of my colleagues in the lab throughout the past two years – Amit, Husam, Hamid, Long, Keyur, Cody, Peter, Steven , Susheel, and Dr. Kuahai Yu, who have shared their knowledge and helpful discussion about my research . I would also like to thank the support provided by the Advanced Research Computing community here at Virginia Tech.

Finally, I would like to thank my family, friends, and girlfriend, who have supported me through the struggles of graduate school. Their love and support throughout this time have made the difference.

Table of Contents

List of Figures

List of Tables

Chapter 1

Introduction

1.1 Motivation

With the ever increasing demand for energy for the world's growing population, renewable energy has become a popular research area. The International Energy Agency (IEA) estimated in 2014 that the global energy demand will grow by 37% by the year 2040. By this year it is also estimated that the world's supply of energy will be equally divided into four parts: oil, gas, coal, and low-carbon sources. Fossil fuels will still account for 75% of the world energy supply, leading to an estimated average temperature increase of 3.6°C globally. To reduce this temperature increase to only 2°C, and minimize extensive climate change effects, the worldwide CO_2 emissions cannot reach 1,000 gigatonnes starting in 2014 [1]. There have been numerous different sources of renewable energy that have been tapped into including wind, biomass, solar, etc. However, one of the largely untapped areas of renewable energy has been river and tidal flows. The tide phenomena occur due to the gravitational force of the moon on the earth combined with the centrifugal force produced by the earth rotating. The tide occurs approximately twice a day resulting in two high tides and two low tides throughout a 24 hour time lapse [2]. For tidal flows, energy can be extracted one of two ways: tidal barrages and tidal turbines, which use principles of potential and kinetic energy respectively [2]. A tidal flow is similar to the flow seen by a wind turbine with a few differences. Water is almost 1000x denser than air and the flow velocity is generally less. The difference in density causes the turbine blades in water to experience much larger forces and moments when compared to wind turbines. A tidal turbine also needs to be able to handle different flow directions depending whether it is a flood or ebb tide (high tide or low tide) [2]. There are two main types of turbines used in tidal flow applications: horizontal and vertical axis turbines. Horizontal axis turbine's (HAT) axis of rotation is parallel to that of the incoming flow, while vertical axis turbine's (VAT) axis of rotation is perpendicular to the incoming flow, seen in Figure 1.

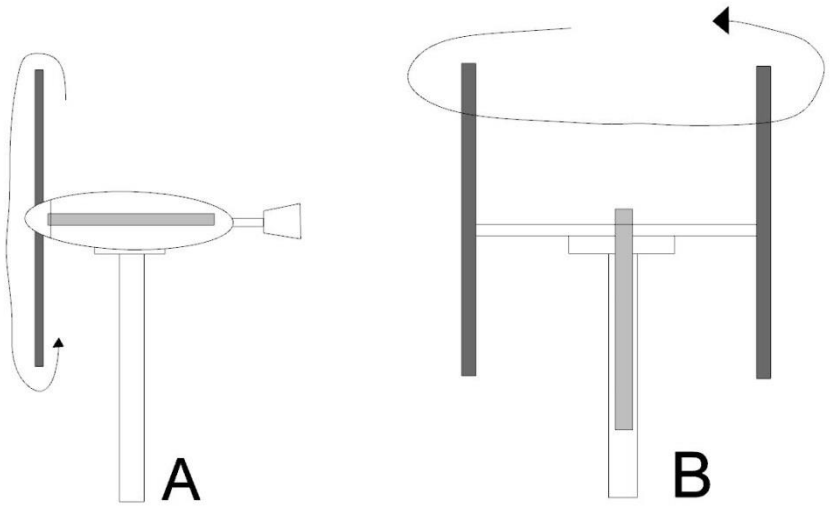

Figure 1.1 Set up of a horizontal axis turbine (A) vs an H-rotor vertical axis turbine (B)

The HAT and VAT both have their advantages and disadvantages. VAT blade designs are much simpler and easier to manufacture when compared to HAT blades. The VAT also has a favorable generator coupling when considering hydrokinetic flows. Because the axis of a HAT is parallel to the incoming flow, there has to be a gearbox to allow a 90° turn to get to the water surface. This adds complications to the design of the HAT and must account for sealing. The rotation axis of a VAT allows the shaft to go directly to the surface without any complications. VATs operate at lower speeds which reduces the amount of noise emitted from the turbine. It has been shown by Iida et al. [3] through numerical simulations that the predicted noise level of vertical axis turbines was 10dB lower than horizontal axis turbines. VATs can operate with the flow coming from any direction. This offers major advantages over HATs since they will not require a yaw system, saving power and complexity [4]. In river or tidal flow, the velocity profile of the flow can vary with depth. Mertens et al. [5] studied the performance of VATs in a skewed flows numerically. They showed that the efficiency of the VAT increased when the flow was skewed.

In the category of VATs, there are three main types of turbines: Savonius, Darrieus and H-rotor. The H-rotor has a simplistic geometry and high energy efficiency for VATs. The base geometry of an H-rotor VAT is an airfoil cross-section that rotates while connected to a center shaft. Further features can be added

by increasing the number of blades, the airfoil profile, etc. Although the geometry of the H-rotor turbine is simplistic it has very complex flow phenomena that give way to unsteady aero/hydro-dynamics.

In this thesis, various VAT parameters are investigated to determine the effect of the overall efficiency of the turbine at a high Reynolds number. The effects of advance ratio, solidity, and downstream wake interactions are investigated using 2D calculations. The OpenFOAM PimpleDyMFoam solver is used to solve the unsteady, incompressible Navier-Stokes Equations and the turbulence quantities are modeled using the k-ω SST turbulence model. To simulate the movement of the VAT blades, Arbitrary Mesh Interfacing (AMI) is utilized. To improve the performance of the VAT in the presence of dynamic stall, calculations were completed both a static twisted blade profile using GenIDLEST and OpenFOAM. A calculation was also done with a twisted blade profile and an effective VAT motion with GenIDLEST.

The thesis is organized as follows:

- In Chapter 2, the solver, solution methods, and turbulence modeling parameters used to solve for the flow around the VAT will be discussed. The method of simulating the VAT motion will also be described.
- In Chapter 3, the aerodynamics behind VAT performance will be presented and the previously discussed solution methods will be compared to experimental values to validate the computational setup. A 2D analysis of the VAT is then presented along with the effects the advance ratio, solidity, and downstream wake on the turbine performance at a Reynolds number of 500,000.
- In Chapter 4, 3D calculation using both OpenFOAM and GenIDLEST were completed on a static twisted blade with various maximum twist angles. These results were then compared to static 2D blades to see if the blade profiles showed any improvements. To simulate the motion of a VAT, an effective VAT pitching motion was tested on both 2D and the 3D twisted blade profile.
- The thesis is summarized in Chapter 5 with concluding remarks.
- Appendix A: Nomenclature

- Appendix B: Forces experienced by the VAT blade during a part of the cycle are shown along with the decomposition of the x and y forces into lift and drag forces
- Appendix C: Comparisons between the ideal lift coefficients, drag coefficients, lift force in the tangential direction, drag force in the tangential direction, total force in the tangential direction, as well as lift and drag force in the tangential direction throughout the cycle and the actual values from calculations

1.2 Literature Review

Many researches have conducted experiments in an effort to gain a better understanding of the physics behind VATs, and have worked on improving their overall efficiency. Kireke and Lazauskas [6] showed that fixed pitch turbines do not produce a high enough starting torque and also perform poorly in strong currents. If a variable pitch turbine were to be used, however, it could produce a high enough starting torque and higher overall efficiency. Kjellin et al [7] performed measurements on a 12kW H-rotor VAT to find optimal operating conditions to achieve the highest overall efficiency. Ferriera et al [8,9] used PIV experiments to visualize dynamic stall on an H-rotor VAT and then simulated the effects using large eddy simulation (LES), detached eddy simulation (DES), and unsteady Reynolds averaged Navier-Stokes (URANS). Overall it was determined that DES most closely matched the results from the PIV experiment. Takao et al. [10] conducted experiments in a wind tunnel to see the effects of guide van geometry on VAT performance. It was shown that by adding guide vanes, the overall efficiency could be increased at high advance ratios. Armstrong et al. [11] investigated the effects of canted blades and canted blades with fences on VAT performance at a Reynolds number of 500,000.

Starting in the late 1900s, there have been various numerical methods used to study VATs. Templin [12] presented the single streamtube model to analyze VAT performance that was derived from blade element momentum theory. The model was shown to over predict the power when compared to experiments. Wilson and Lissaman [13] presented an improvement to the single streamtube model. In the

multiple streamtube model, the swept area of the turbine is divided into multiple streamtubes. Blade element momentum theory is then applied to each of the individual streamtubes. The multiple streamtube model was shown to better predict the forces experienced by the turbine blades and induced velocity than the single streamtube model. Paraschivoiu [14] then introduced another improvement to the numerical simulation of VATs with the double-multiple streamtube model (DMSM). In the DMSM the wind turbine is separated into a pair of actuator disks at each level of the rotor and then divided into multiple streamtubes. This model again showed better comparisons to experiments than previous models. Bianchini et al. [15] implemented the DMSM to evaluate the effect of virtual camber on the performance of VATs. It was shown that by including the virtual camber effect for transient simulations greatly increased the accuracy of the predicted turbine revolution speed. Rathi [16] used the DMSM to investigate H-rotor VAT performance with active blade pitch control. It was shown that with active blade pitching, a rotor could have self-starting characteristics.

Vortex models have also been used to aide in the study of VATs. Larsen [17] applied a vortex model to study a single blade on a VAT. However, the model assumed a small angle of attack and the effect of stall was not included. Strickland et al. [18] added the effects of dynamic stall, pitching circulation, and added mass to improve the vortex model. Cardona [19] modified the dynamic stall effect of the vortex model which showed better predictions of the instantaneous forces seen by the turbine blades. In 2006 Wang et al. [20] used 2D vortex panel methods to simulate a variable pitch straight blade VAT. It showed good results compared to previous models and significantly reduced the computation time. However, it did not include dynamic stall effects and was limited to 2D analysis.

With the improvement of computing power, computational fluid dynamics (CFD) has become a largely used instrument to study VATs. Almohammadi et al. [21] performed mesh independency studies for 1^{st} and 2^{nd} order accurate schemes on a 2D H-rotor VAT. It was found that a second order accurate scheme produced a slightly smaller standard error than the 1^{st} order scheme when comparing the efficiencies at different advance ratios. Balduzzi et al. [22,23] compared the pressure based RANS/SST solver used in Fluent to a compressible density based research code COSA for VATs. Different mesh

techniques were also used in the study: a sliding mesh technique with Fluent, and Arbitrary Eulerian Langrangian (ALE) with COSA. Both gave similar results that compared well to experimental data. Critical issues in CFD when simulating a 2D VAT was also investigated. It was found that a pressure based solver with a 2nd order upwind scheme for spatial discretization of all transport equations and bounded 2nd order implicit time stepping produced the best results. The k-ω SST turbulent model was used in the study based on the ability to perform well with separated and free-shear flows. It was also shown that the time step requirement to acquire accurate results was a function of the rotational speed of the turbine. Castellie et al. [24,25] looked at the effect of grid size on the airfoil wall with different turbulence models in relation to replicating VAT experimental data. Also investigated was the effect of the number of blades on VAT performance, showing that the peak efficiency decreased with an increasing number of blades and shifted to a lower advance ratio. The role of curvature effects relating to airfoils rotating cycloidally has been investigated by [26] and [27]. Benedict et al. [28] showed that the efficiency of a VAT is largely a function of the blade pitching amplitude and that performance could be further improved by using cambered airfoils. It was also shown that when increasing the Reynolds number from 40,000 to 300,000 the maximum power extracted increased by 15%. Carrigan et al. [29] used an optimization tool based on the advance ratio, solidity, and blade profile to generate an optimized airfoil cross section. It was shown that the efficiency could be increased by a small percentage when compared to a standard blade geometry, which was theorized to be due to elimination of leading edge separation. Previous parametric studies have been done by both [30] and [31]. The effects of advance ratio, solidity, airfoil type, and Reynolds number were all shown to have a significant impact on the VAT efficiency. Howell et al. [32] performed 2D and 3D simulation of an H-rotor VAT. Large differences in the efficiency between the 2D and 3D simulations were rationalized to be due to the presence of tip vortices in 3D simulations. It was also shown that the phases where large amounts of lift were generated also generated stronger tip vortices. Liang et al [33] looked at the aerodynamic performance of an H-rotor VAT. It was shown that the turbine blades experience attached flow, mild stall, deep stall, and reattached flow all in one cycle. Tsai and Colonius [34] investigated the flow of a VAT at a low Reynolds number

using the Immersed Boundary Method (IBM). The motion of a VAT blade was simplified by decomposing into surging motions, pitching motions, and a Coriolis force. It was shown that this motion estimated the lift coefficient well during the upstroke phase, but overestimated during the downstroke phase.

Chapter 2

Numerical Methodology

All calculations are performed using the open source code OpenFOAM and in house code GenIDLEST. The details of the framework and methodology used in OpenFOAM can be found in Weller et al [35]. In this chapter the relevant governing equations and the modified URANS governing equations are given. The solution algorithm PimpleDyMFOAM used to solve the governing equations along with the k-ω SST turbulence model will be presented. The AMI method used for mesh motion will be discussed. Finally, the aspects of GenIDLEST pertinent to this research are outlined.

2.1 OpenFOAM

2.1.1 Governing Equations

The form of the Navier-Stokes equations for incompressible flow in conservative form is as follows:

Continuity:

$$\frac{\partial u_i}{\partial x_i} = 0 \qquad \textbf{Equation 2.1}$$

Momentum:

$$\rho \frac{\partial u_i}{\partial t} + \rho \frac{\partial}{\partial x_j}\left(u_j u_i\right) = -\frac{\partial p}{\partial x_i} + \frac{\partial}{\partial x_j}\left(2\mu S_{ij}\right) \qquad \textbf{Equation 2.2}$$

where μ is the molecular viscosity and S_{ij} is the strain rate tensor ,

$$S_{ij} = \frac{1}{2}\left(\frac{\partial u_j}{\partial x_i} + \frac{\partial u_i}{\partial x_j}\right) \qquad \textbf{Equation 2.3}$$

The energy equation was not solved due to low Mach number and incompressible assumption, no body forces were included as well. Turbulence is modeled in the framework of the Unsteady Reynolds

Averaged Navier-Stokes equations (URANS) formulation. The equations are derived by decomposing the instantaneous velocity components into an averaged and fluctuating quantity

$$u_i(\boldsymbol{x}, t) = U_i(\boldsymbol{x}, \boldsymbol{t}) + u_i'(\boldsymbol{x}, t) \qquad \textbf{Equation 2.4}$$

This term is inserted into the Navier-Stokes equations and time averaged.

$$\frac{\partial U_i}{\partial x_i} = 0 \qquad \textbf{Equation 2.}$$

$$\rho \frac{\partial U_i}{\partial t} + \rho U_j \frac{\partial U_i}{\partial x_j} = -\frac{\partial P}{\partial x_i} + \frac{\partial}{\partial x_j}\left(2\mu S_{ij} - \overline{\rho u_i' u_j'}\right) \qquad \textbf{Equation 2.6}$$

After the time averaging is performed the Reynolds stress tensor appears in the equations, $-\overline{\rho u_i' u_j'}$ which is represented as τ_{ij} . The addition of the stress tensor requires closure which is done by relating the Reynolds stress tensor to the velocity gradient using the Boussinesq eddy-viscosity assumption

$$\overline{-\rho u_i' u_j'} = 2\mu_t S_{ij} - \frac{2}{3}\rho \delta_{i,j} k \qquad \textbf{Equation 2.6}$$

This assumption models the Reynolds stress tensor based on the eddy viscosity, μ_t. The eddy viscosity is defined as

$$\mu_t = \frac{\rho k}{\omega} \qquad \textbf{Equation 2.7}$$

where k is the turbulent kinetic energy and ω is the specific turbulent kinetic energy dissipation rate. The eddy viscosity is modeled using the two equation k-ω SST turbulence model based on previous work showing good comparisons to experimental results. In the SST model a blending function is used to combine elements from the k-ε and k-ω models. The k-ω model has been shown to be more accurate than the k-ε in near wall layers, but does not do well in free shear layers. The k-ω equation has been shown to

be extremely sensitive to values of ω in the free stream outside of the boundary layer. The blending function F_1 is formulated to use the k-ω model near walls, and to gradually blend in the k-ε model away from walls. With this approach the superior near wall performance of the k-ω model is employed together with the superior performance of the k-ε model in the free-stream [36].

$$\frac{\partial(\rho k)}{\partial t} + \frac{\partial(\rho U_j k)}{\partial x_j} = \widetilde{P_k} - \beta^* \rho\omega k + \frac{\partial}{\partial x_j}\left(\Gamma_k \frac{\partial k}{\partial x_j}\right) \qquad \textbf{Equation 2.8}$$

$$\frac{\partial(\rho\omega)}{\partial t} + \frac{\partial(\rho U_j \omega)}{\partial x_j} = \frac{\gamma}{\nu_t} P_k - \beta\rho\omega^2 + \frac{\partial}{\partial x_j}\left(\Gamma_\omega \frac{\partial \omega}{\partial_{x_j}}\right) + (1 - F_1) 2\rho\sigma_{\omega 2} \frac{1}{\omega} \frac{\partial k}{\partial x_j} \frac{\partial \omega}{\partial x_j} \qquad \textbf{Equation 2.9}$$

with

$$\Gamma_k = \mu + \frac{\mu_T}{\sigma_k}, \quad \Gamma_\omega = \mu + \frac{\mu_T}{\sigma_\omega}, \; P_k = \tau_{ij} \frac{\partial U_i}{\partial x_j}, \widetilde{P_k} = \min(P_k, c_l \epsilon) \qquad \textbf{Equation 2.10}$$

2.1.2 PimpleDyMFoam Solver

The unsteady Navier-Stokes equations were solved using the open source finite-volume code OpenFOAM [35]. OpenFOAM is a C++ library that is used to create executables that fall into two categories: solvers and utilities. The solvers are used to solve problems in continuum mechanics while the utilities perform data manipulation tasks. A main advantage with OpenFOAM is that users can create and edit solvers as well as utilities once some understanding of the underlying method used in OpenFOAM has been gained. For the problem at hand the PimpleDyMFoam solver provided by OpenFOAM was used based on the large time step ability and the dynamic mesh solver capabilities.

The PimpleDyMFoam algorithm is a merged version of the transient SIMPLE and PISO algorithms. A simplified mapping of the solver can be seen in Figure 2.1. At the start of each time step the mesh motion is activated and the absolute flux from the mapped velocity is calculated. This flux is then made relative to that mesh motion. The pressure-velocity coupled loop is started where the momentum equation is

solved first and then the pressure corrector loop is entered. Inside this loop the pressure equation is solved and then the velocity field is corrected. Lastly the turbulence modeling equations are solved and the next time step ensues [37] [38]. OpenFOAM allows the user to specify the number of pressure-corrector loops as well as the number of pressure-velocity coupling loops. If the number of pressure-corrector loops is set to one, the solver is operating in SIMPLE mode. If the number of pressure-velocity coupled loops is set to one, the solver is operating in PISO mode. To allow for a large time step a mixture of pressure corrector and pressure-velocity loops should be employed.

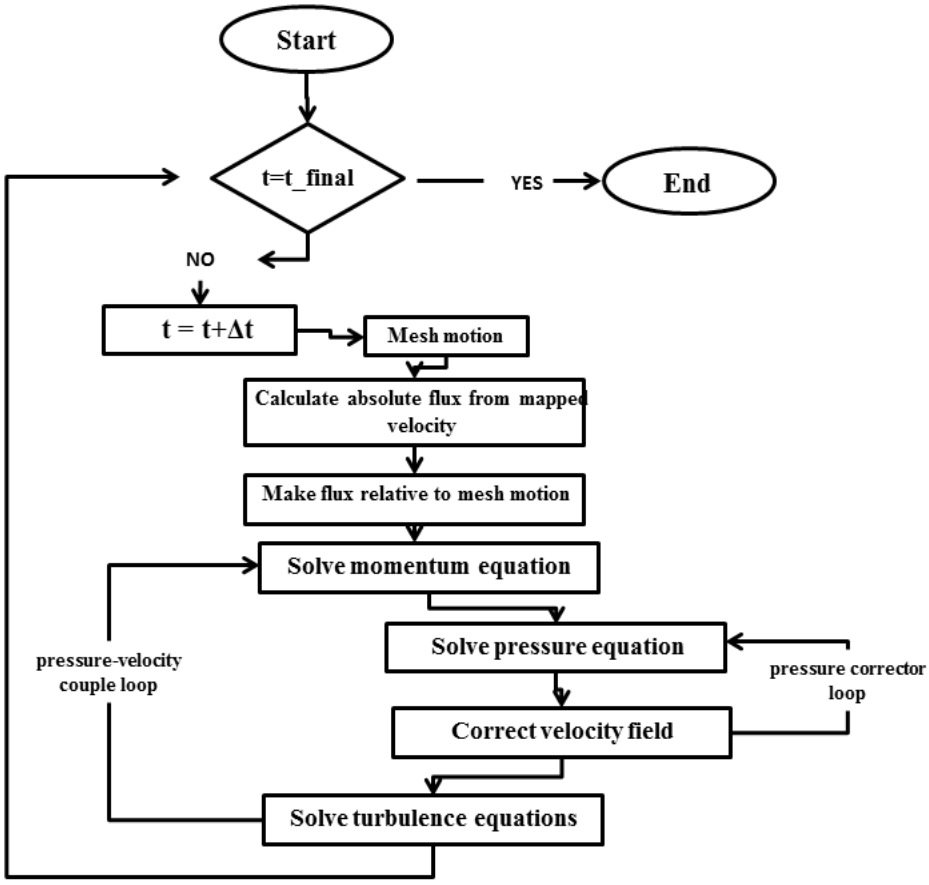

Figure 2.1. PimpleFyMFoam solver tree used in OpenFOAM

2.1.3 Arbitrary Mesh Interface

To simulate the motion of an H-rotor VAT a mesh motion had to be implemented. To simulate this motion, the Arbitrary Mesh Interface (AMI) method was used. The AMI method allows for simulation across disconnected, but adjacent meshes. These domains can be either stationary or move relative to one another. Standard interpolation of a field q_D from a donor mesh (T_D) to a target mesh (T_T) receiving field q_T suffers from certain disadvantages. These include not being conservative, the minimum and maximum are eroded, and not being able to handle discontinuous fields well. In AMI a Galerkin projection is used with the projection from T_D to T_T being accurate in the L_2 norm. The Galerkin projection gives rise to the matrix form of the donor and target fields

$$M_T q_T = M_{TD} q_D \qquad \textbf{Equation 2.11}$$

Matrix M_{TD} is a mixed mass matrix between the two meshes T_D and T_T. Once this matrix is assembled Equation 2.14 can be solved using a standard iterative solver to compute q_T [39]

The setup of the AMI method for the case of a 2D H-rotor VAT involved having two separate zones in the mesh: stationary and rotating. The rotating zone contains the blades and surrounding mesh to a value of 1.7R. The stationary mesh is set from the boundaries to the circle containing the rotating mesh. At the interface of the two zones the values between cells are interpolated as described above. The rotating mesh was given a rotational velocity that varied for different cases run.

2.2 GenIDLEST

To better resolve the flow over the twisted blades, an in-house code –Generalized Incompressible Direct and Large Eddy Simulation of Turbulence (GenIDLEST) was used. The details of the framework and methodology used in GenIDLEST can be found in Tafti [40] and Tafti [41]. In this section the relevant governing equations is given with elements of the immersed boundary method (IBM) [42] that was used.

2.2.1 Governing Equations

The non-dimensional form of the Navier-Stokes equations for incompressible flow is as follows:

Continuity:

$$\frac{\partial u_i}{\partial x_i} = 0 \qquad \textbf{Equation 2.12}$$

Momentum:

$$\frac{\partial u_i}{\partial t} + \frac{\partial (u_j u_i)}{\partial x_j} = -\frac{\partial P}{\partial x_i} + \frac{1}{Re}\left(\frac{\partial^2 u_i}{\partial x_j \partial x_j}\right) \qquad \textbf{Equation 2.13}$$

Where the non-dimensionalizations are:

$$x_i = \frac{x_i^*}{L_{ref}^*}; u_i = \frac{u_i^*}{L_{ref}^*}; t = \frac{t^* u_{ref}^*}{L_{ref}^*}; p = \frac{P^* - P_{ref}^*}{\rho_{ref}^* u_{ref}^{*2}}; Re = \frac{\rho_{ref}^* u_{ref}^* L_{ref}^*}{\mu_{ref}^*}$$

The above governing equation are transformed to generalized coordinates and discretized with a conservative finite-volume formulation using a second-order central (SOC) difference scheme on a non-staggered grid topology. The Cartesian velocities and pressure are calculated and stored at the cell center, whereas the fluxes are calculated and stored at cell faces. A projection method using second order predictor-corrector step is used for the time integration for the continuity and momentum equations. In the

predictor step, an intermediate velocity field is calculated; and in the corrector step, the updated divergence free velocity is calculated at the new time-step by solving a pressure-Poisson equation.

2.2.2 Immersed boundary method

The immersed boundary method (IBM) is an extension of a scheme that was initially proposed by Gilmanov and Sotiropoulos [43] to a non-staggered grid with a curvilinear coordinate system. In the method used, the governing equations are solved without modification for the nodes in the fluid domain, with special treatment applied solely to the first layer of fluid nodes next to the immersed boundary. This allows a number of different turbulence models to be used in parallel with IBM such as DNS, LES, RANS, etc. The details and framework can be found in Nagendra et al. [42]

In the first step of IBM, the solid boundary modeled as the immersed boundary is provided as an input in a discretized form. Each segment contains location information with respect to the fixed background fluid grid, normal, and length/area (2D/3D). The normal is used to describe the solid side of the immersed boundary and the length/area of the surface grid is used for post processing to calculate surface forces, heat flux, etc. A search-locate and interpolate algorithm is used to mark the nodes of the background mesh in the proximity of the immersed boundary. The type of node (fluid or solid) is determined based on the surface grid and will form a fluid/solid boundary on the background mesh. The fluid/solid nodes that are in the immediate vicinity of the immersed surface are defined as fluid/solid IB nodes. All of the nodes in the background mesh are assigned one of the following nodetypes: fluid, solid, fluid IB, or solid IB node (the solid IB nodes are only defined for conjugate heat transfer).

Once all of the nodes have been assigned a type, the governing equations are solved for all of the fluid nodes. The nodes marked IB nodes are then modified to see the presence of the immersed surface. A probe in the surface grid normal direction with a distance of one cell is assigned to each of the IB nodes seen. A tri-linear interpolation method is used to determine the value of the desired primitive flow variable at the probe location from the surrounding nodes. The probe value is then used to find the value

at the IB node that satisfies the proper boundary condition. For Dirichelt condition, it is assumed that the gradient between the IB surface and probe location is constant giving:

$$\phi_{ib} = \frac{d_{ib} * \phi_{p1} + (d_{p1} - d_{ib}) * \phi_{BC}}{d_{p1}} \qquad \textbf{Equation 2.14}$$

For a Neumann boundary condition, the formulation is written as:

$$\phi_{ib} = \phi_{p1} - (d_{p1} - d_{ib}) * \left.\frac{\partial \phi}{\partial n}\right|_{BC} \qquad \textbf{Equation 2.15}$$

When the governing equations are solved at the fluid nodes in the following time step, these IB values will be used. Therefore, the immersed boundary will be seen by the nodes in the fluid region. Validation of IBM framework used for fully developed channel flow and pipe flow can be seen in He [44].

Chapter 3

2D Rotating VAT Calculations

To increase the efficiency of the vertical axis turbines, 2D CFD simulations are completed in an effort to better understand the physics behind the operation of these turbines. Specifically, the effect of advance ratio, solidity, and wake interactions were investigated. Simulations were completed in OpenFOAM using the k-ω SST turbulence model at a nominal Reynolds number of 500,000 using a NACA 0015 airfoil. To simulate the motion of the turbine, Arbitrary Mesh Interfacing (AMI) was used. For all of the parameters tested, it was found that the effective angle of attack seen by the turbine blades had a significant impact on the power extracted from the flow. The range of effective angles of attack was found to decrease as the advance ratio increased. In spite of this, a severe loss in the power coefficient occurred at an advance ratio of 2.5 during which the blade experienced dynamic stall. This effect was also seen when the number of turbine blades was changed to four, at a solidity of 1.08. This negative impact was found to be due to the increase in the drag component of the tangential force when dynamic stall occurs. Results indicate that wake interactions between subsequent blades have a large impact on performance especially when the wake interaction alters the flow direction sufficiently to create conditions for dynamic stall.

3.1 VAT Aerodynamics

The type of VAT analyzed was an H-rotor which consists of straight blades with a constant cross section of a NACA 0015 airfoil at a Reynolds number of 500,000. When a fluid flows past the blades a pressure differential is created on the blades that causes both lift and thrust forces to be generated. Because the blade is rotating it experiences different velocities and angles of attack during the cycle, which leads to varying lift and thrust forces. The blade sees a relative velocity, W, which is based off of the free stream velocity U_∞, and the instantaneous speed of the blade itself ωR. The altered angle of attack

denoted the ideal effective angle of attack, α_{eff}, is the angle between the blade chord line and the instantaneous relative velocity the blade sees. The quantities can be seen at various points in the cycle in Figure 3.1. Note that the start of the cycle for Blade 1, the reference blade for all plots hereafter, is at θ=90°.

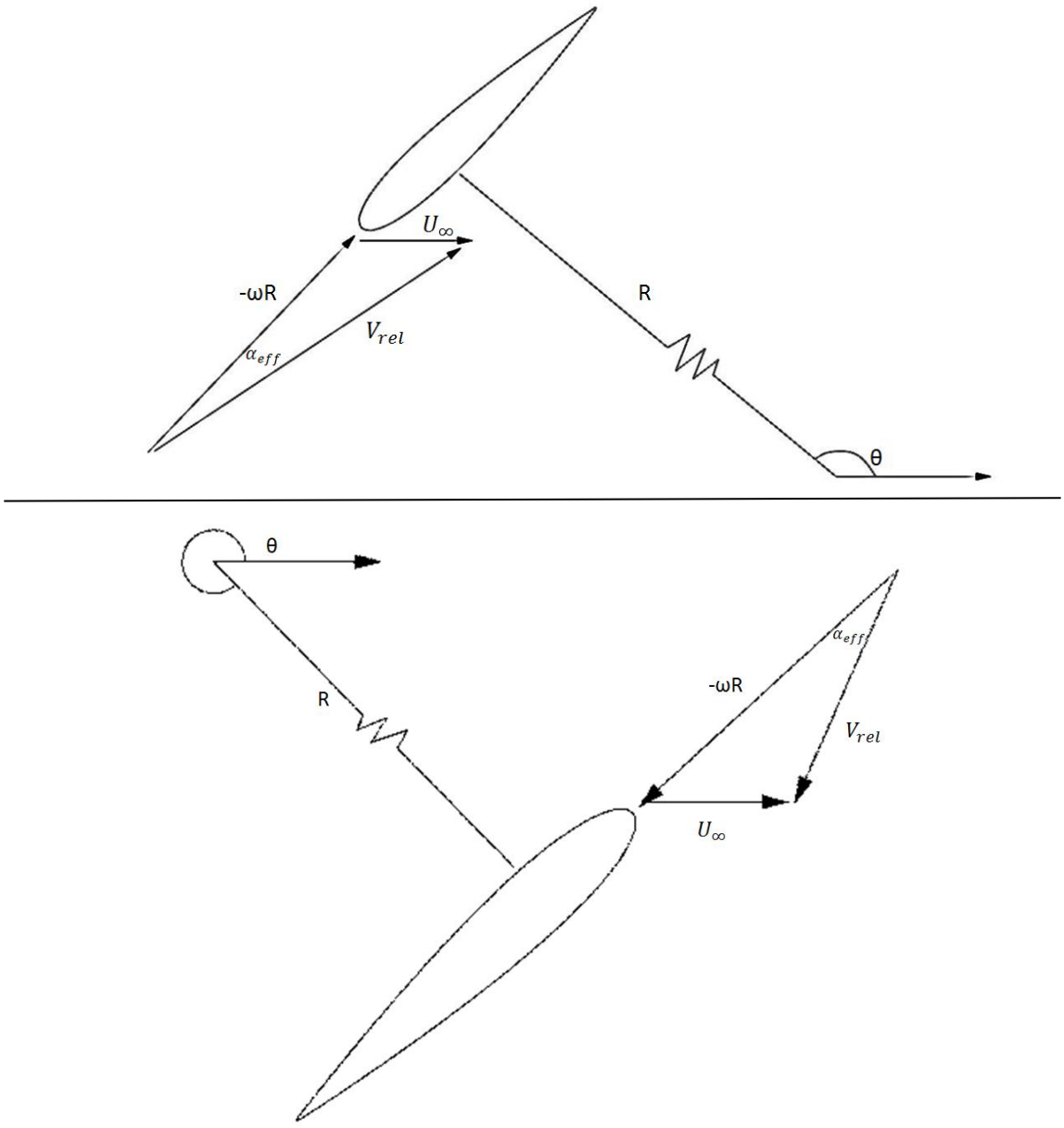

Figure 3.1 Relative velocity, V_{rel}, seen by the VAT blades and ideal effective angle of attack (labeled α in this figure) at two different azimuthal positions

Barring other induced velocities, the ideal effective angle of attack for an H-rotor VAT is both a function of the azimuthal position, θ and the relative velocity of the blade seen below:

$$\alpha_{eff} = \cos^{-1}\left(\frac{\overrightarrow{V_{rel}}\cdot\vec{t}}{|\overrightarrow{V_{rel}}||\vec{t}|}\right) \quad \textbf{Equation 3.1}$$

where $\vec{t}$ is the tangential unit vector of the blade. Since the relative velocity is a function of the advance ratio seen below:

$$\lambda = \frac{\omega R}{U_\infty}, \quad \textbf{Equation 3.2}$$

the ideal effective angle of attack is also a function of the advance ratio of the turbine. For small values of λ the range of α_{eff} is very large with sharp gradients near an azimuthal angle of 270°. As the value of λ increases, the range of α_{eff} decreases as well as does the gradient of angle change near 270° seen in Figure 3.2. It is important to note that for a NACA 0015 airfoil at Re = 500,000, the static stall angle of attack occurs at about 15° [45]. It is also important to define the solidity of a VAT define as:

$$\sigma = \frac{Nc}{R} \quad \textbf{Equation 3.3}$$

where N is the number of blades and c is the blade chord length.

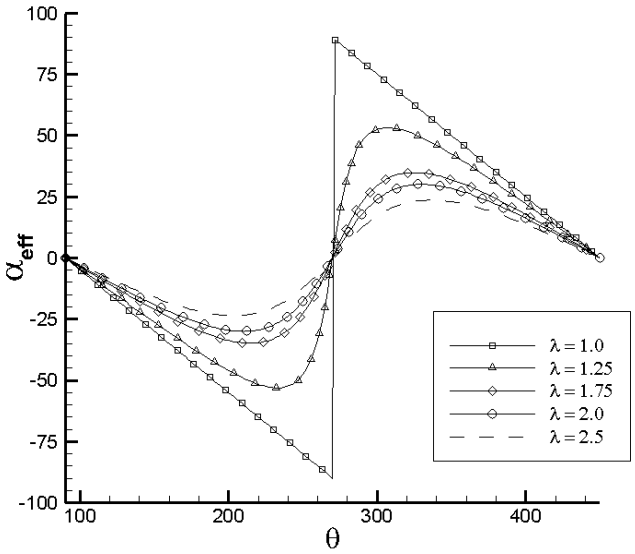

Figure 3.2 The ideal effective angles of attack versus the azimuthal angle at various advance ratios

Since the blades of a VAT are rotating with a changing ideal effective angle of attack, and not stationary, they will experience dynamic stall instead of static stall. When the airfoil's angle of attack is increasing/decreasing rapidly, the onset of stall is delayed from the static stall angle. Dynamic stall then occurs which in most cases is more severe and persistent than static stall. While a dynamic airfoil delays stall and results in much higher lift coefficients than a static airfoil at the same angle of attack, once dynamic stall sets in, there is a sharp drop in the lift coefficient. The degree of loss of lift (light versus deep stall) is a function of the airfoil shape, Reynolds number, angle of attack, and the rate of change of the angle of attack. Dynamic stall begins at the leading edge of the airfoil and has six distinct phases [46]. It starts with an attached boundary layer that then has a flow reversal inside the boundary layer as the angle of attack increases. A leading edge vortex (LEV) then forms and detaches from the airfoil and starts to move over its surface. As it moves towards the trailing edge a secondary vortex then forms at the leading edge. Finally, as the ideal effective angle of attack decreases, the flow reattaches at the leading edge [46]. Because dynamic stall influences the lift and drag force, it will have an impact on the overall efficiency of the VAT.

Figure 3.3 shows the lift and drag forces, as well as the normal and tangential unit vectors of a blade. As the blade rotates throughout the cycle the normal force will always be perpendicular to direction of motion. Since it is always perpendicular to the direction of motion it does not contribute to the torque generated, the torque generated is solely due to the thrust force.

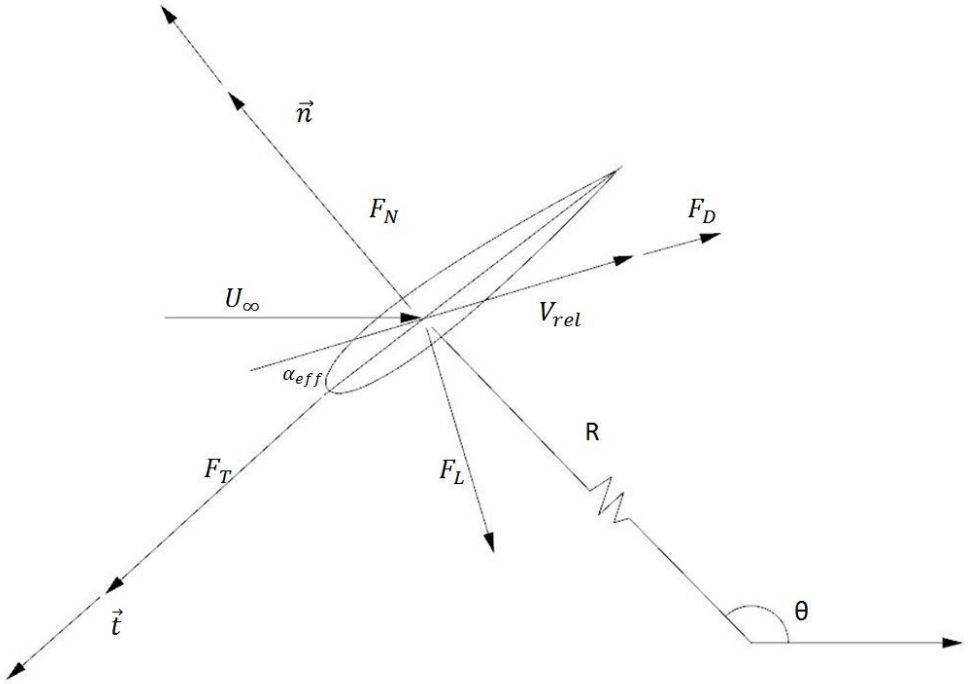

Figure 3.3 Instantaneous forces felt by VAT blade

The thrust force F_T and the normal force F_N can be expressed as below:

$$F_T = F_L * cos\left(\frac{\pi}{2} - \alpha_{eff}\right) - F_D * cos(\alpha_{eff}) \quad \textbf{Equation 3.4}$$

$$F_N = F_L * \sin\left(\frac{\pi}{2} - \alpha_{eff}\right) + F_D * \sin(\alpha_{eff}) \quad \textbf{Equation 3.5}$$

where F_L and F_D are lift and drag forces, measured normal and tangent to the approach velocity defined by the effective angle of attack (α_{eff}) , respectively. The lift and drag coefficients per unit span C_L and C_D can be expressed as:

$$C_L = \frac{F_L}{\frac{1}{2}\rho(\omega R)^2 c} \quad \textbf{Equation 3.6}$$

$$C_D = \frac{F_D}{\frac{1}{2}\rho(\omega R)^2 c} \quad \textbf{Equation 3.7}$$

where c is the turbine blade chord. Note that the reference velocity in the denominator is the rotational velocity which is a better measure of the dynamic head than the freestream velocity. The torque τ for a single blade is solely due to the tangential force and can be calculated as:

$$\tau = RF_T \quad \textbf{Equation 3.8}$$

where R is the radius of the turbine as shown in Figure 3.1. The torque coefficient is then expressed as:

$$C_\tau = \frac{\tau}{\frac{1}{2}\rho RAU_\infty^2} \quad \textbf{Equation 3.9}$$

For 2D simulations the span of the blades is considered to be of unit length so A can be expressed as:

$$A = 2R \quad \textbf{Equation 3.10}$$

Therefore, the power for each blade in the turbine is

$$P = \tau\omega \quad \textbf{Equation 3.11}$$

and then power coefficient for each blade is defined as:

$$C_{p,blade} = \frac{P}{\frac{1}{2}\rho A U_{\infty}^{3}} \qquad \textbf{Equation 3.12}$$

To find the efficiency for the turbine, all of the power coefficients for each blade in the turbine must be summed up and then averaged over one cycle:

$$C_P = \frac{1}{2\pi}\int_0^{2\pi}(\sum_{i=1}^{n} C_{p_n}(\theta))d\theta \qquad \textbf{Equation 3.13}$$

3.2 Computational Domain

Figure 3.4 shows the two-dimensional VAT geometry used for the calculations where c is the blade chord length, 0.4m, and R = 3.6875c. The setup of the AMI method for the case of a 2D H-rotor VAT involved having two separate zones in the mesh: stationary and rotating. The rotating zone contains the blades and surrounding mesh to a value of 6.25c, or approximately 1.7R. The stationary mesh is set from the boundaries to the circle containing the rotating mesh. At the interface of the two zones the values between cells are interpolated as described in Chapter 2. The rotating mesh was given a rotational velocity that varied for different cases run. The inlet of the domain was 16c and the outlet was a distance of 24c from the rotating region. The calculations were run for four full rotations of the VAT at a Re = 500,000. The Reynolds number is calculated based on: $Re = \frac{U_{\infty} c}{\nu}$, where c is the chord length of the VAT blades.

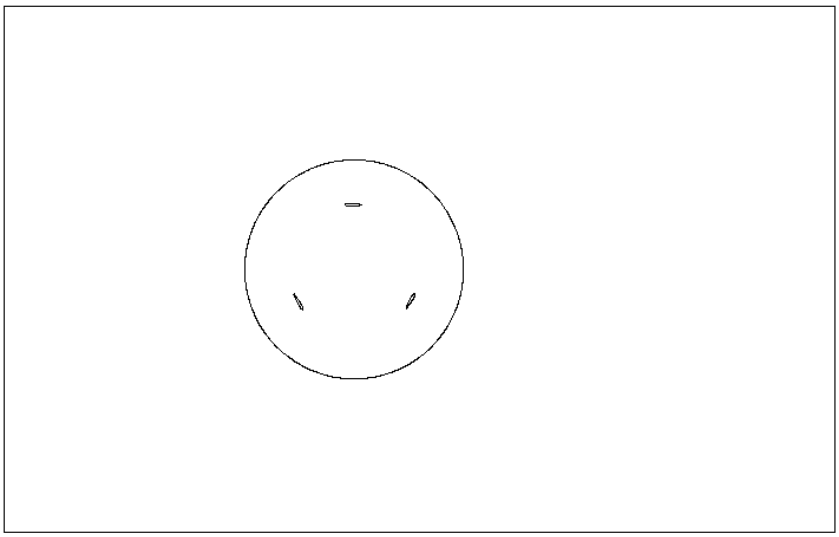

Figure 3.4. The computational domain used for calculations

To ensure that the k-ω SST model correctly models the turbulence near the blades a y+ value of 1 was set for the mesh at the wall. A triangular unstructured mesh was used everywhere except in the near the blades where a quadrilateral mesh was implemented as seen in Figure 3.5. The average number of cells for each case was about 300,000 and took about 14 days to run through 4 cycles on 16 processors. This varied for the case of examining the solidity where the number of airfoils was altered by changing the number of blades in the VAT, and thus the number of computational cells increased to 363,000 for 4 blades and 510,000 for 6 blades, respectively. After each case ran through four cycles it was determined that the results had converged based on the small amount of variation in the C_p for each blade between two consecutive cycles.

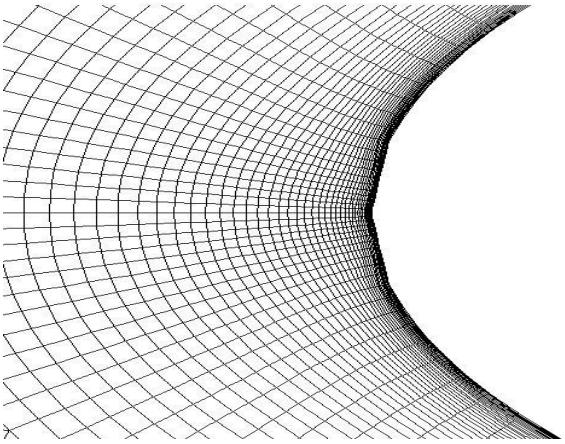

Figure 3.5. Close up of the quadrilateral mesh on the blade surface at a $y^+ = 1$

A grid independency study was conducted to determine the effect of the grid size on the results. Three different grids were used varying in the number of total cells shown in Table 3.1. The fineness of the grid was increased by increasing the number of points along the surface of each VAT blade while keeping the y^+ value equal to one. This in turn increased the resolution in the near blade region inside of the rotating domain. The number of cells was kept constant in the stationary region of the computational domain.

Table 3.1. Grid sizes used for grid independency study

Grid	# Points Along Blade	Total Cell Count
Grid 1	100	100k cells
Grid 2	350	220k cells
Grid 3	750	350k cells

The results of the grid sensitivity study can be seen in Figure 3.6. Grid 2 and 3 gave back very similar results with a difference in the overall power coefficient of about 1%, while Grid 1 had a difference of over 20% from the finest grid. Grid 2 was run on 32 processors taking about 124 hours to run four cycles at about one second per time step. Grid 3 was also run on 32 processors taking almost 360 hours to complete four cycles, taking about three seconds per time step. Because of the increased performance and

small difference in overall pressure coefficient, the final computations were run on Grid 2. Validation of this mesh with experimental results can be seen in Figure 3.8.

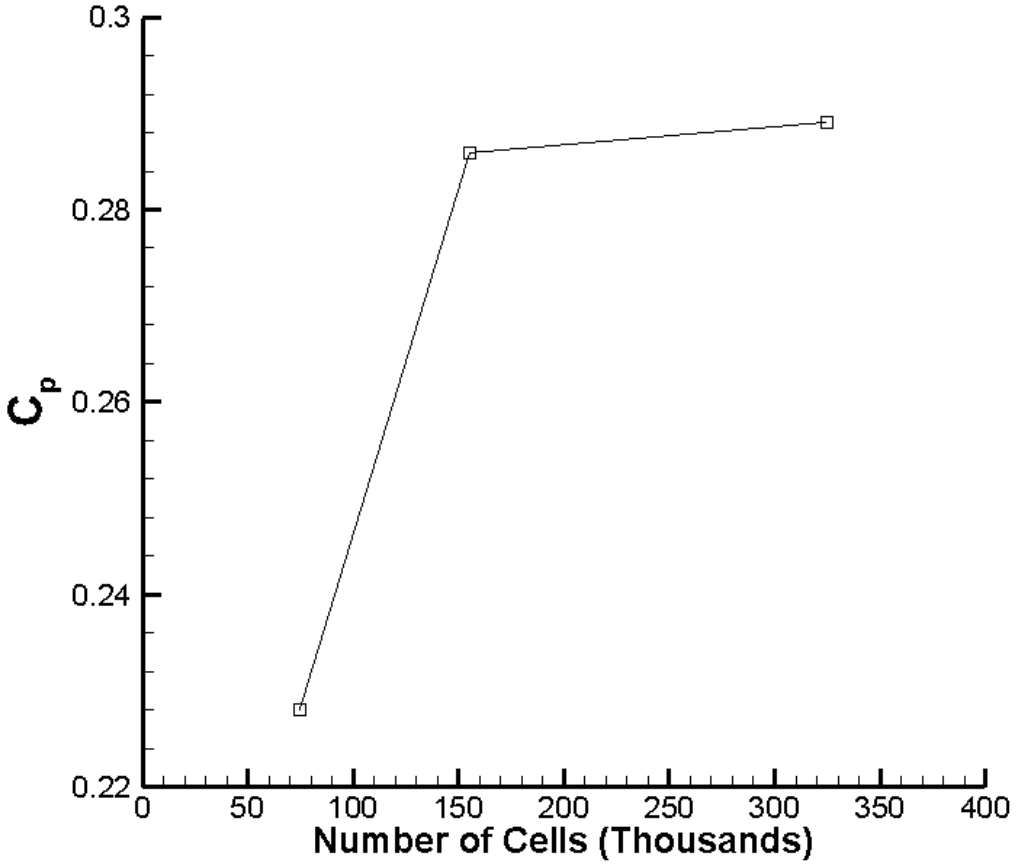

Figure 3.6. Overall power coefficient for difference mesh sizes

Three different convective schemes were also tested to determine the effect on the results: second order central (SOC), second-order upwind, and first-order upwind. SOC is dispersive giving rise to oscillations, the first and second-order upwind schemes are dissipative damping out any oscillations that may arise by introducing dissipation of $O(\Delta)$ and $O(\Delta^2)$, respectively. All three cases were tested; however, the SOC scheme was not stable and caused the solution to diverge. The comparison between the first-order and second-order upwind scheme for a single blade can be seen in Figure 3.7. The second order scheme shows a larger peak in the power coefficient at an azimuthal angle of about 190° than first order upwind. In the second half of the cycle there is also a slightly higher power coefficient with the

second order scheme. The overall turbine power coefficient for both cases can be seen in Table 3.2. The second order upwind scheme predicted a higher overall power coefficient than the first order scheme,

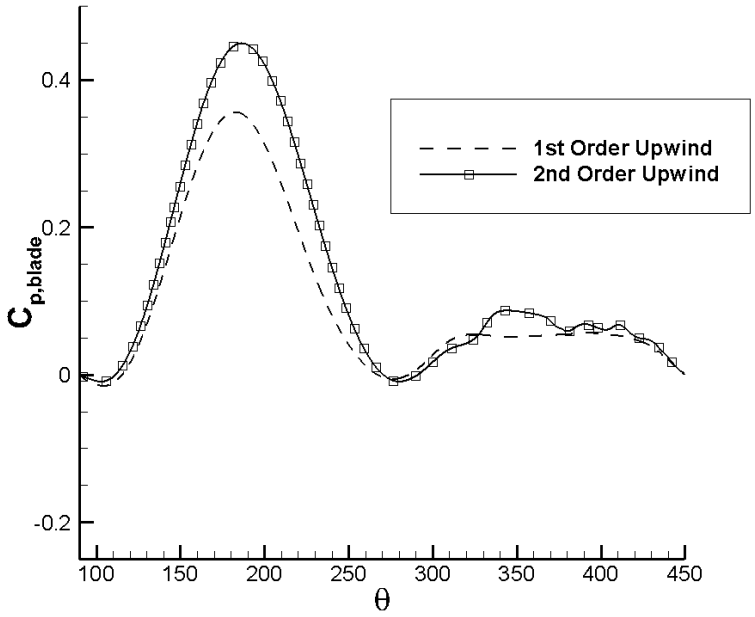

Figure 3.7. Comparison of power coefficient for first and second order upwind scheme for a single blade

as expected from the blade power coefficient plot. Since the first order scheme is more dissipative, it dampens out some of the viscous effects near the blades leading to a lower power coefficient per blade. The overall power coefficient for the second order scheme was about 6% higher than that of the first order scheme. When the second order scheme was tested at high advance ratios however, it became unstable and the calculation diverged. Since the first order scheme gave similar results to the second order scheme and was more stable at higher advance ratios, it was used for all final calculations.

Table 3.2.The overall power coefficient for first and second order upwind schemes

Convective Scheme	Cp	% Diff
1st Order Upwind	0.286	5.92
2nd Order Upwind	0.304	0

3.3 Effects of Advance Ratio

To validate the computational methods and problem set up, the effect of advance ratio on cycle averaged C_p was investigated. Armstong et al. [11] experimentally investigated the effect of canted blades on VAT performance. The control case of blades with a canting angle of $\beta = 0$, Re = 500,000 and σ = 0.81was used to validate the computational method. Five different cases of λ were run (seen in Table 3.3) and the values of cycle-averaged C_p were compared to the experimental values seen in Figure 3.8.

Table 3.3. The advance ratio with corresponding rotational velocity

Advance Ratio	ω (rad/s)
1.0	0.678
1.25	0.847
1.75	1.186
2.0	1.356
2.5	1.695

It was found that the results from the simulations matched well with the experimental values. A maximum C_p value of 0.28 was found at an advance ratio of λ = 2.0, which was slightly higher than the experimental values. The computational model was also able to capture the steep decrease in C_p occurring at high advance ratios of 2.5. While the power coefficients are predicted quite accurately at small λ, the current calculations over-predict the values at large λ greater than 2. This could be due to the inability of the model to predict the post-stall dynamics accurately.

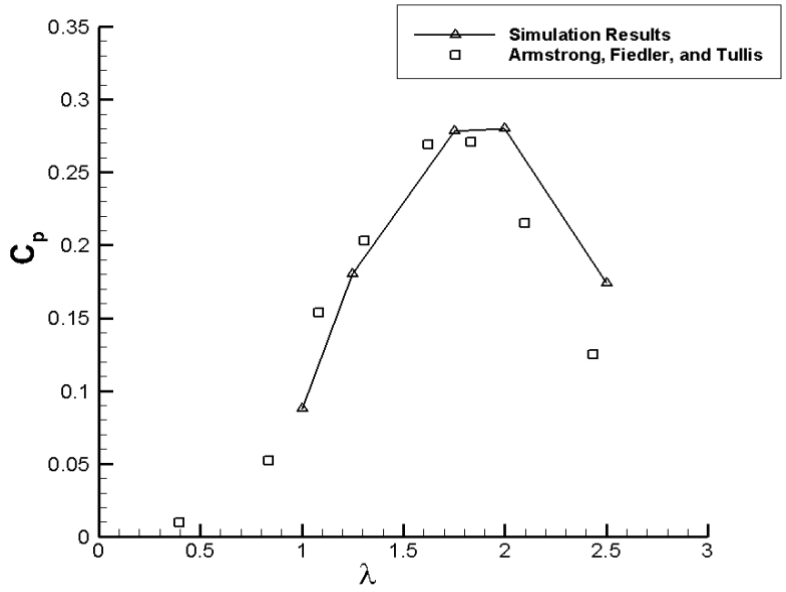

Figure 3.8. Cycle-averaged power coefficient variation with advance ratio compared to experiments.

As was shown in Figure 3.2, the advance ratio influences the range of the effective angles of attack the blades experience through the cycle. This causes the power coefficient for a single blade to vary throughout the cycle for a given advance ratio. At different advance ratios, the $C_{p,blade}$ variation changes as seen in Figure 3.9 which begins at 90^o. As the blade moves counter-clockwise, the power coefficient increases steadily to reach a peak value between 160^o and 200^o depending on the advance ratio. It is found that as the advance ratio increases, the peak C_p value increases and the azimuthal angle at which this peak occurs also increases. Note that as the advance ratio increases, the blade approach velocity increases, increasing the Reynolds number and the dynamic head seen by the blade. Thus, barring any drastic changes in the flow around the blade, the power (P in Eqn. 3.10) increases. While C_p includes the effect of rotational velocity, the torque coefficient ($C_{\tau,blade}$) gives a better representation of the tangential force acting on the blade.

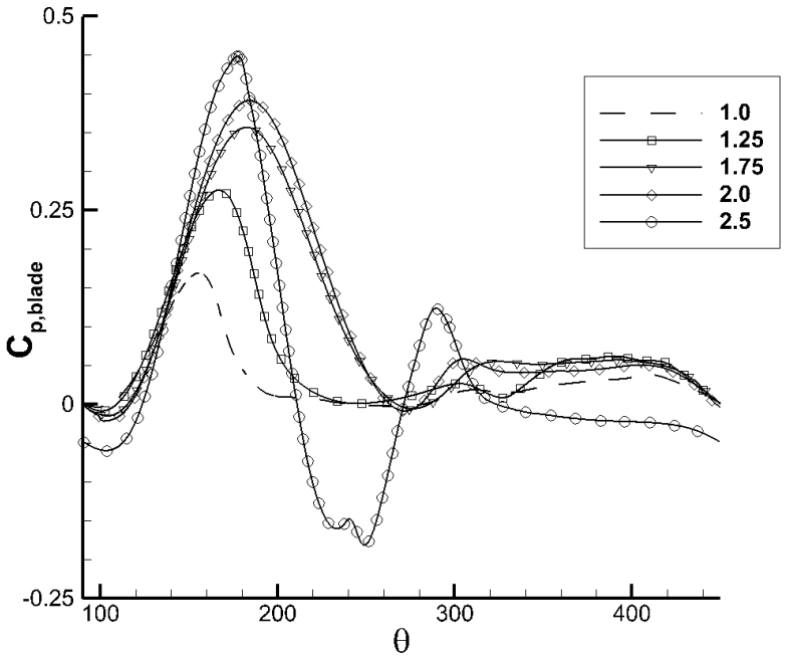

Figure 3.9. Power coefficient variation per cycle for different advance ratios

The magnitude of the tangential force acting on the airfoil is primarily dependent on the lift force produced normal to the effective direction of motion of the airfoil (effective velocity) and the orientation of the lift force w.r.t. the tangential direction or the ideal effective angle of attack (α_{eff}). The contribution of lift towards the tangential force increases with α_{eff} and the negative impact of drag also decreases with increase in α_{eff}. Thus as high as possible α_{eff} is desirable that can sustain high lift and low drag for maximizing the tangential force, i.e, without going into dynamic stall which would drastically decrease lift and increase drag. In Figure 3.2, the ideal effective angle of attack increases from zero at 90^o to a maximum value and decreases again as the airfoil approaches 270^o. Thus during the first half of motion, the contribution of lift force to tangential force increases, but then starts to decrease as α_{eff} decreases. Comparing different advance ratios, as λ increases, the contribution of lift force to tangential force decreases, but this is countered by the increase in lift force as the dynamic head increases. In travelling from 270 back to 360 degrees, the same dynamics hold true, however, the physics of torque production is further complicated by wake interactions which would not only reduce the dynamic head of the approach

flow but also impact the ideal effective angle of attack by changing the incident flow direction. Thus most of the torque production occurs during the traverse from 90 to 270 degrees, while the rest of the cycle contributes minimally to the power cycle.

There is a very small difference between the torque coefficients for different advance ratios in the first 70° of the cycle (90°-160°) as shown in Figure 3.10. The lower advance ratios do have a slightly higher value of C_τ for this part of the cycle. This could result from the higher α_{eff} as seen in Figure 3.2. For the case of $\lambda = 1$ there is then a sharp decrease in the torque coefficient after $\theta = 160^{\circ}$. At this point the ideal effective angle of attack is at about 40°, after which the lift coefficient of a NACA 0015 airfoil decreases [45]. This in turn causes the torque for $\lambda = 1$ to decrease before the other cases, and the same can be said for $\lambda = 1.25$. At higher advance ratios (1.75 and 2.0), the increase in torque is sustained longer till about 190° at which the respective α_{eff} have values between 25 and 30° close to the peak values which occur at about 220°. Beyond 190°, there is a steady decrease in the torque coefficient, most probably due to the combined effect of decrease in α_{eff} and decrease in lift.

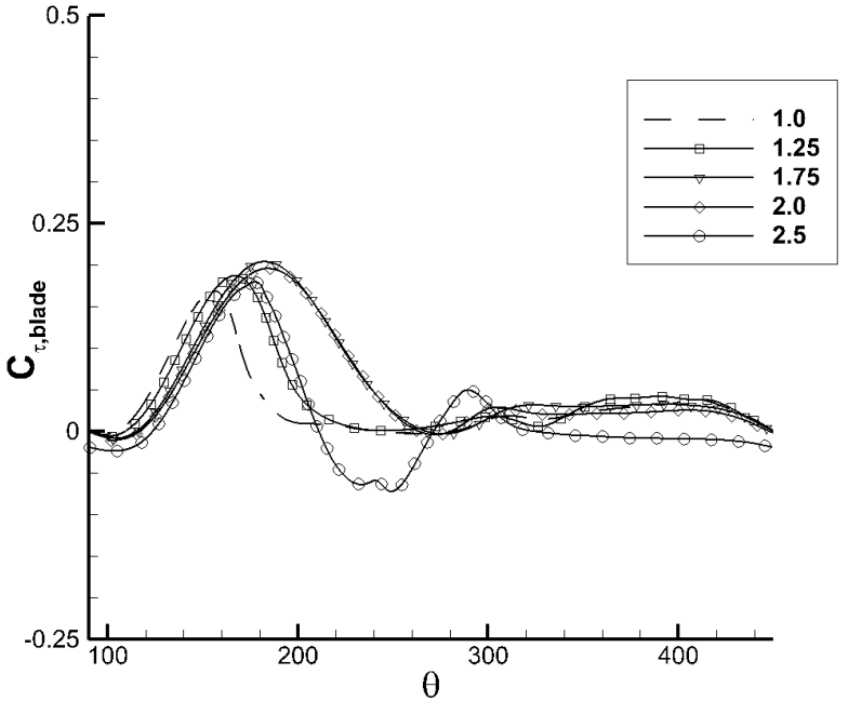

Figure 3.10. Torque coefficient variation per cycle for different advance ratios

At $\lambda = 2.5$, it can be seen in Figure 3.9 that the power coefficient decreases sharply at $\theta = 185°$ and so does the torque coefficient. Not only is there a sharp drop, but the power coefficient and torque become negative between 210 to 270^o, indicating either a negative lift and/or a large increase in the drag. Further investigation reveals that the airfoil goes through dynamic stall during this period. This is shown in Figure 3.11 comparing the vorticity dynamics to λ=1.75 during the same period (184^o – 233^o). It can be clearly seen that a stalled leading edge vortex (LEV) starts to form at 194^o, and grows over the subsequent time frames and is about to separate at 233^o, coinciding with the peak negative value of torque. In contrast, the flow field for λ =1.75 shows a strong shear layer formed on the suction side, which gradually moves away from the surface as θ increases but there is no massive separation as seen for λ=2.5.

One could ask the question, as to what leads to dynamic stall for this case given that α_{eff} is bounded between ±23^o which is less than that realized with the smaller advance ratios, and that the dynamic head

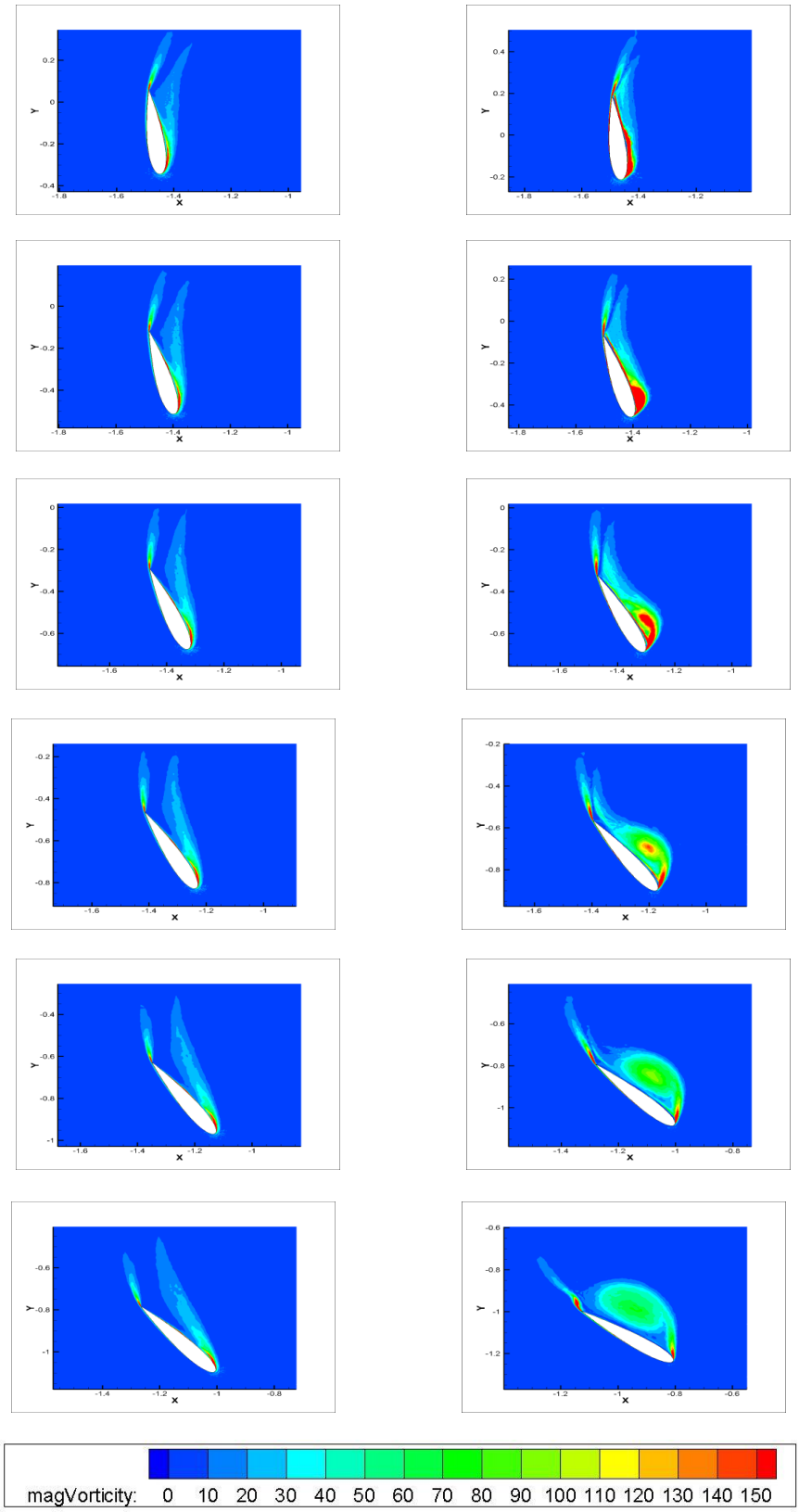

Figure 3.11. Comparison between λ=1.75 (left) and λ=2.5 (right) at the same circumferential positions. The case of λ=2.5 is showing the evolution of dynamic stall from θ = 184° to θ = 233° which leads to the large drop in power coefficient discussed previously. For the same angles the case of λ=1.75 a LEV does not form and eventually separate, thus the power coefficient does not experience the dramatic drop.

(or Reynolds number) has increased, both of which are favorable conditions towards prolonging the onset of dynamic stall. While we do not have a clear answer, it is suspected that the high rate of rotation could lead to conditions in which blade wakes start interacting with each other and could induce conditions favorable to the onset of dynamic stall.

To investigate this further, an actual representation of the velocities and effective angles were sought. Data was extracted from a distance of c/4 in front of blade 1 at various points throughout the fourth cycle of the VAT. From this data the relative velocity magnitude was plotted for the advance ratios of $\lambda = 1.0$, 1.75, and 2.5 and compared to what is expected based on the ideal effective angle of attack seen in Figure 3.12. For the advance ratio of 1.0 there is very poor agreement with the expected relative velocity magnitude throughout the entire cycle. Because of the low advance ratio, the rotational effects of the VAT do not dominate the flow, causing the difference. Advance ratios of 1.75 and 2.5 show much better comparison to the expected values especially during the first half of the cycle. During the first half the effects of the wake do not have as large of an impact on the relative velocity as compared to the second half of the turbine cycle. It is also noted that the advance ratio of 2.5 compares very well to the expected values during this first half. This further solidifies the theory that when the rotational effects dominate the flow, a more accurate representation of the relative velocity magnitude can be expected during the first half of the cycle.

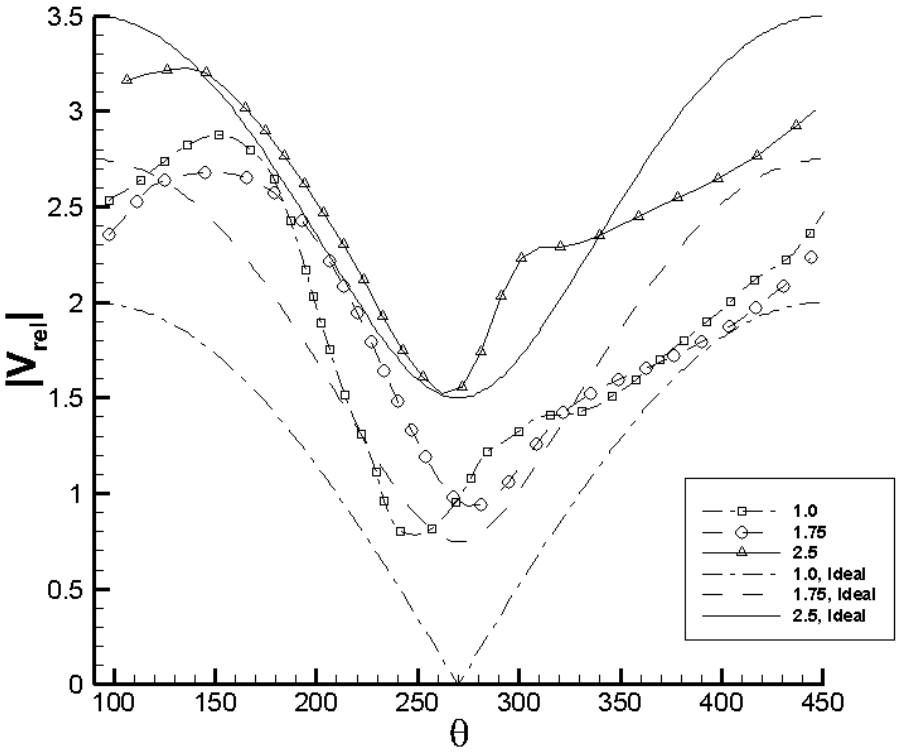

Figure 3.12. The relative velocity magnitude seen by blade 1 compared to the expected idealized velocity magnitude for advance ratios of 1.0, 1.75, and 2.5

The effective angle of attack for the same three advance ratios was then compared to the expected ideal effective angle of attack seen in Figure 3.13. The same general trends that were seen with the relative velocity magnitude can be seen in the comparison of effective angles of attack. There is good comparison in the first half of the cycle with the ideal effective angle of attack but deviates in the second half of the cycle because of the wake interactions. For all three advance ratios the ideal effective angle of attack over predicts the actual effective angle of attack seen by the blade. As seen previously there was dynamic stall seen in the case of $\lambda = 2.5$ from 184° to 233°. During this part of the cycle the blade experiences effective angles of attack that go from -23°, to a peak value of -26°, and then back down to -24°. However, when looking at lower advance ratios over this portion of the cycle the range and magnitude of effective angles of attack is much larger and should therefore lead to dynamic stall. This leads us to believe that the larger rotational speed has an impact on the occurrence of dynamic stall, but to what extent is still not clear.

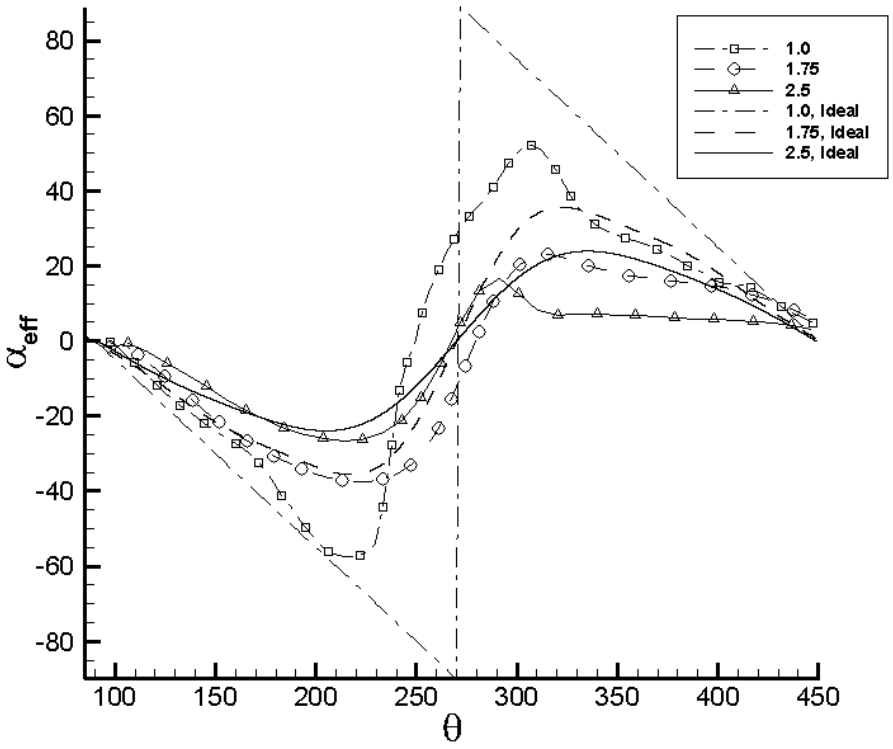

Figure 3.13. The effective angle of attack seen by blade 1 compared to the geometric effective angle of attack for advance ratios of 1.0, 1.75, and 2.5

The lift and drag coefficients for a single blade, as defined in Equation 3.6 and 3.7 respectively, averaged over the entire cycle were compared for the different advance ratios tested seen in Figure 3.12. The expression used to obtain lift and drag from the x- and y- components of the force vector are given in Appendix B. It is noted that in calculating the lift and drag forces, the idealized effective angle of attack and approach velocity are used in Figures 3.14 to 3.17. Appendix C shows results with the actual effective angle of attack and approach velocity from Figure 3.12 and 3.13. While there are differences between the two approaches, the general trends are quite similar. This, together with the sensitivity of the extracted approach velocity and effective angle to the measurement location, we have chosen to present the results in the idealized setting.

Both the lift and drag coefficients decrease with an increase in the advance ratio with a maximum lift coefficient of 1.04 for $\lambda = 1.0$ and a minimum of 0.26 occurring for $\lambda = 2.5$. The cases with a higher λ will

see a much larger nominal velocity, ωR, which accounts for the drop in the coefficients based on the definition seen in Equations 3.6 and 3.7. The actual lift force increases almost linearly by a factor of 2.4 from λ =1.0 to 2.5 caused by an increase in the dynamic head. On the other hand, the drag force decreases up to λ = 1.75 as a result of a decreasing angle of attack, after which there is a sharp increase as dynamic stall sets in at λ = 2.5.

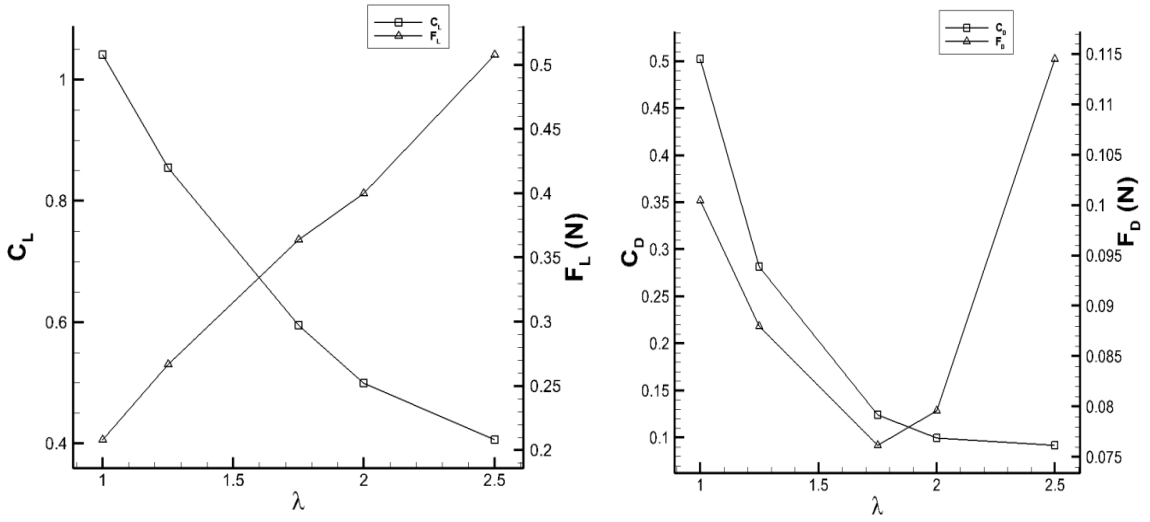

Figure 3.14. The cycle averaged lift (left) and drag (right) for a single blade at various advance ratios.

While lift and drag coefficients on a blade are good indicators of aerodynamic performance, their contributions to the tangential thrust force in Figure 3.15 directly impact the performance of the turbine. For each value of λ the cycle averaged lift and drag component of the thrust force is shown. Every value of λ shows that the total thrust force is lower than that of the lift component. This is due to the negative effects of drag on the thrust production throughout the cycle. At each advance ratio the ideal effective angle of attack varies significantly as seen in Figure 3.2. This variation in ideal effective angle of attack impacts whether the lift and drag components are acting in favor of or opposing thrust. As the advance ratio increases the contribution of lift to the tangential force increases until a value of λ = 2.0. There is then a slight drop in the lift contribution, but a large drop in the total tangential force. The negative effects of drag on the tangential force continue to increase at a higher rate than lift component with the advance

ratio. It should be noted that there is a significant increase in the magnitude of the drag component for the case of $\lambda = 2.5$.To further investigate the effects of lift and drag on the performance of the turbine, the two components are shown throughout the entire cycle in Figures 3.14 and 3.15,respectively. The lift component of thrust has the same general shape as that of the power coefficient for each value of λ seen in Figure 3.9.

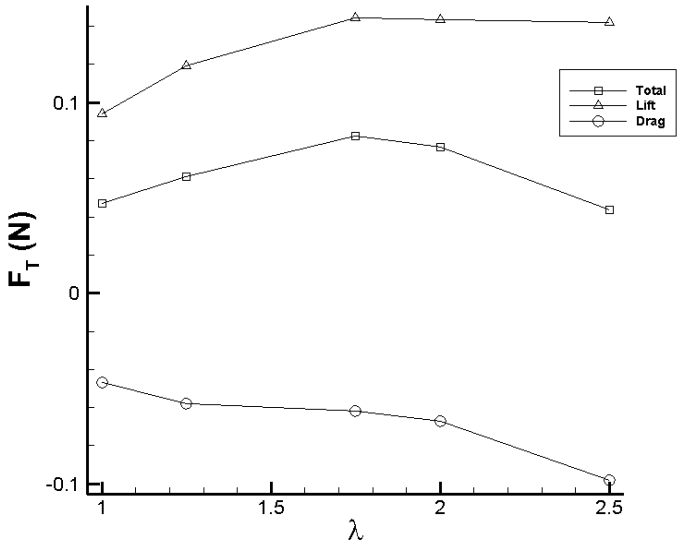

Figure 3.15. The cycle averaged components of lift and drag forces in the tangential direction and total tangential force for different advance ratios

As the advance ratio increases, the peak value of the lift component does as well with a slight phase shift in the azimuthal position where it occurs. This is followed by a drop in the lift component until $\theta = 270°$. For all of the cases except $\lambda = 2.5$, there is another rise in the lift component that continues through the remainder of the cycle that is not reflected in the power coefficient. This is because of the drag component of thrust being negative in that portion. The drag component follows a similar trend to the lift coefficient except with negative effects on the thrust production. There is a large peak that occurs at approximately $\theta = 170°$ and then a drop off until about 270°. There is then another negative increase in the drag component for the remainder of the cycle. There is a noticeably different trend with the drag profile for the case of $\lambda = 2.5$ where dynamic stall was seen to occur. At 170°, instead of a reduction in the magnitude of the drag component there is another large spike from 180° to 240°. This is the same

range that the dynamic stall phenomena was seen to occur in Figure 3.11. For all the cases there is significant reduction in the force produced during the second half of the cycle due to the blade interaction with the wake from the first half traveling downstream. The case of $\lambda = 2.5$ does not show the slight positive lift/ negative thrust in the second half of the cycle. When the blade experiences dynamic stall the separated vortices continue to travel downstream further altering the downstream wake, accounting for this difference.

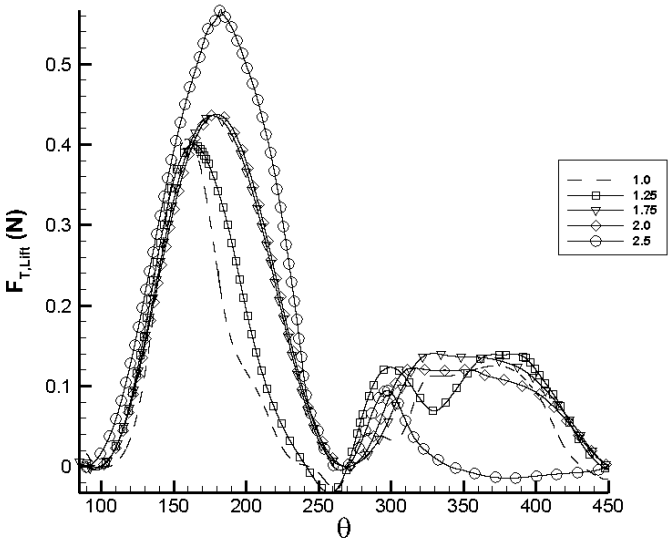

Figure 3.16. The lift component of thrust force in the tangential direction throughout the cycle for different advance ratios

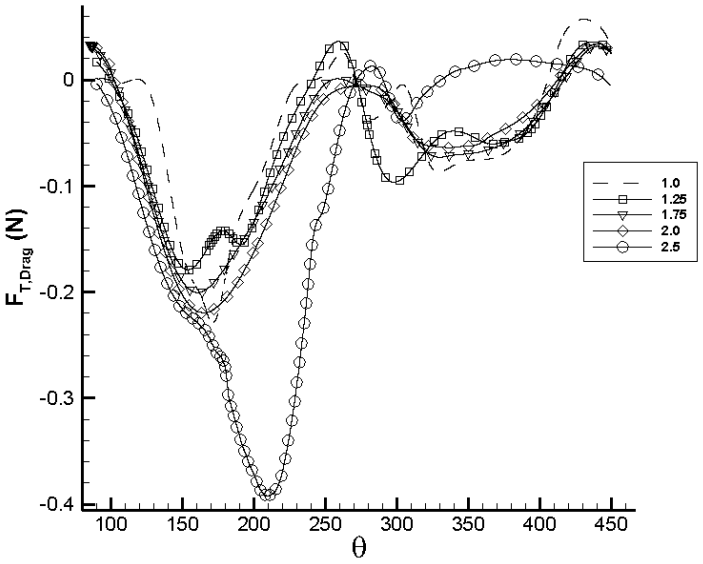

Figure 3.17. The drag component of thrust force in the tangential direction throughout the cycle for different advance ratios

3.4 Effects of Solidity

To study the effect of solidity on a VAT the number of blades in the VAT was altered as seen in Table 3.4. All cases maintained an advance ratio of $\lambda = 1.75$.

Table 3.4 The number of blades with corresponding solidities

Number of Blades (N)	σ
2	0.54
3	0.81
4	1.08
6	1.63

The effect of the number of blades on the power coefficient can be seen in Figure 3.16. As the number of blades increase, the potential to harvest more power should increase in direct proportion to the number of blades. However, as the number of blades increase, blade interactions will also increase having a detrimental effect on the overall power coefficient hence in general the power coefficient of each blade

will decrease but the overall power coefficient should increase. This trend should continue to a point where the solidity is too great and the power coefficient begins to decrease. When the solidity gets large enough there will not be enough flow through the VAT to rotate it. Effectively the turbine will act like a circular cylinder and generate very little torque. While the above arguments would predict an increasing overall power coefficient with increasing solidity till an optimum solidity was reached and then a subsequent decline, the result in Figure 3.18 shows a sharp drop in the power coefficient to 0.077 at N=4, with a subsequent recovery at N=6.

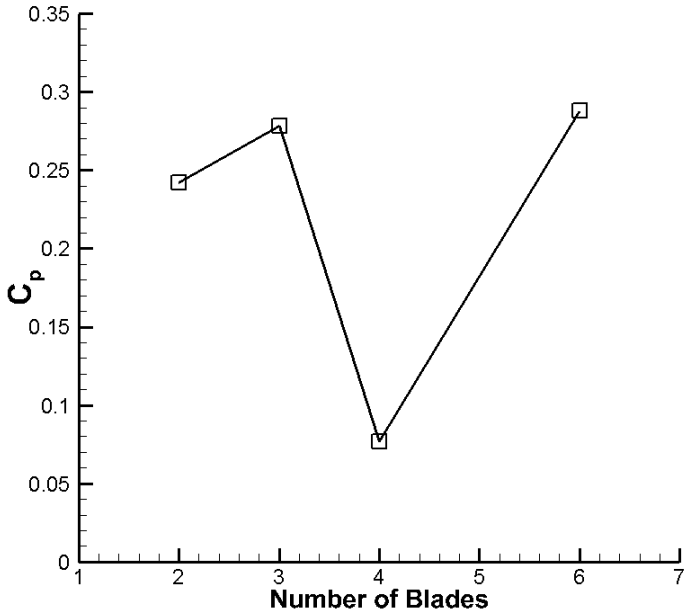

Figure 3.18. Power coefficient variation for different numbers of blades

Further investigation into the effects of the number of blades/solidity can be done by looking at the $C_{p,blade}$ variation on a single blade throughout a cycle as shown in Figure 3.19. The first aspect to notice is that for a smaller number of blades, the peak power coefficient is much higher. This is due to the fact that with a smaller number of blades, there is less interaction with the trailing wake from the blade in front, and also less wake interaction in the second half of the cycle from the upstream wake. For example, with N = 2 the blades are separated by 180° compared to N = 6 where the blades are separated by only 60°.

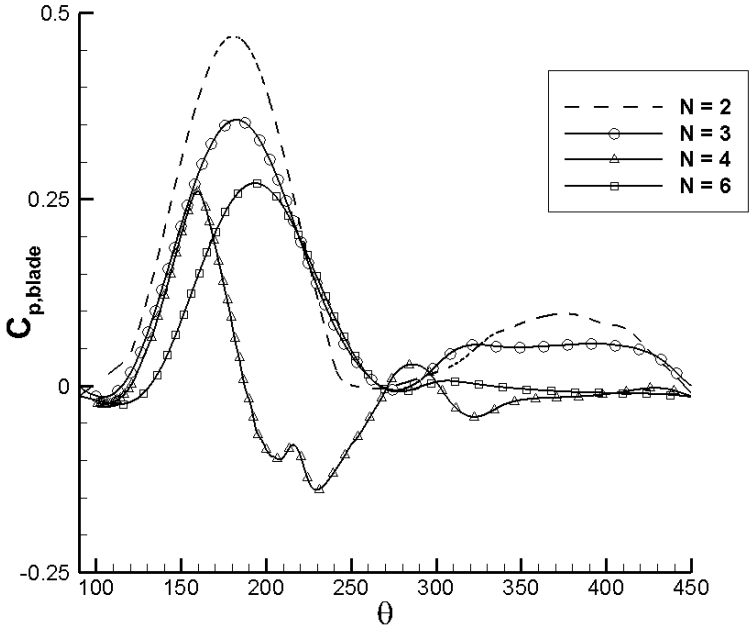

Figure 3.19. Power coefficient variation per cycle for different number of blades

The detrimental effect of blade proximity on harvesting energy is also reflected in the power coefficient when the blade traverses the second half of the cycle. For N = 2 there is a significant amount of power extracted, compared to essentially zero power for the case of N = 6. Due to the larger number of blades there is significantly more wake interactions in the second half of the cycle. This effect can be seen in Figure 3.20. For N = 2 the streamlines in the second half of the cycle are relatively uniform and straight. When the number of airfoils is increased to six, the direction of the streamlines varies between the upper and lower half of the cycle. They are also at a much higher angle than when compared to N = 2. The magnitude of the streamwise velocity is very close to the freestream velocity U_∞ for the case of N = 2. In contrast for N = 6, the velocity encountered by the blades in the second half of the cycle is significantly less than U_∞.

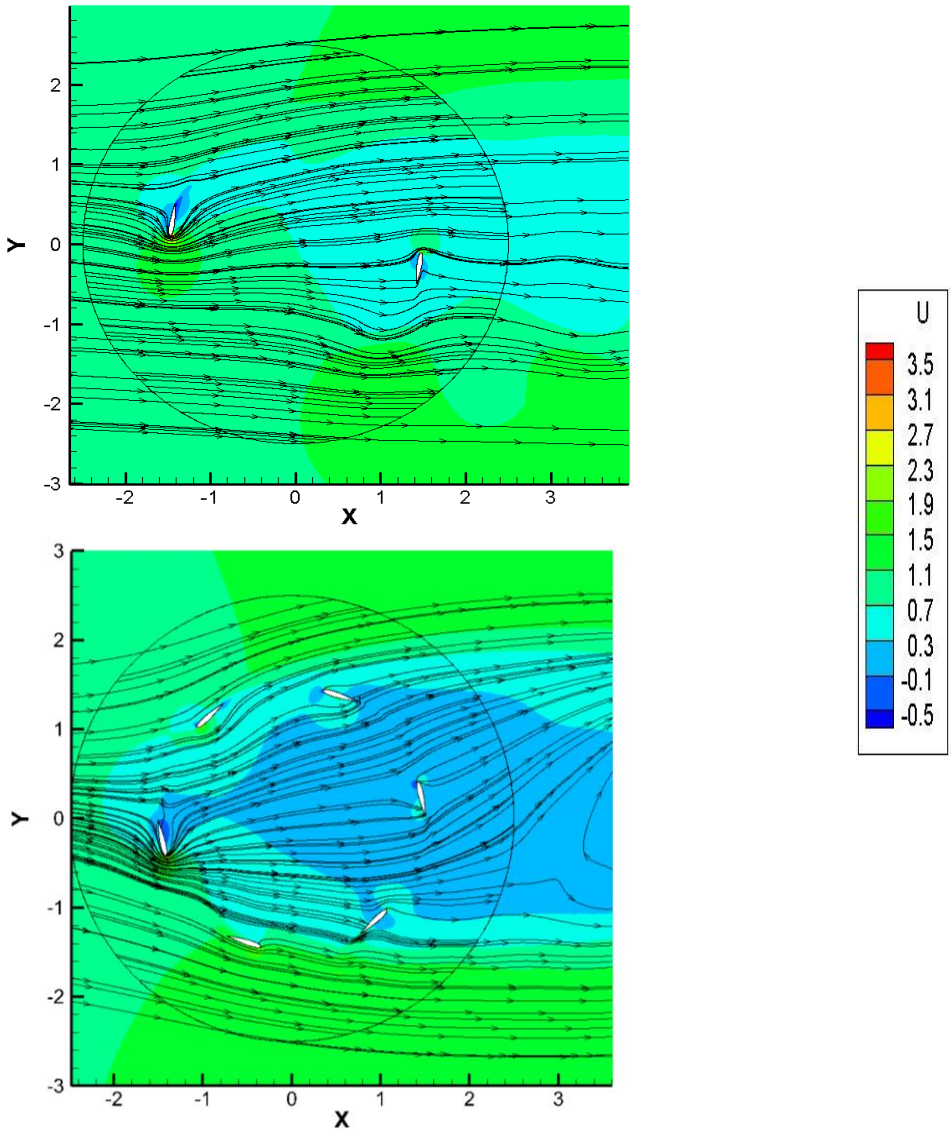

Figure 3.20. Streamwise velocity and streamline comparison between N = 2 (top) and N = 6 (bottom)

The case of N = 4 does not follow the trend seen in the other solidity cases but follows a trend very similar to that observed earlier for $\lambda = 2.5$. There is not only a steep drop in the power coefficient before it reaches the expected peak position relative to the other cases, but the power coefficient also becomes

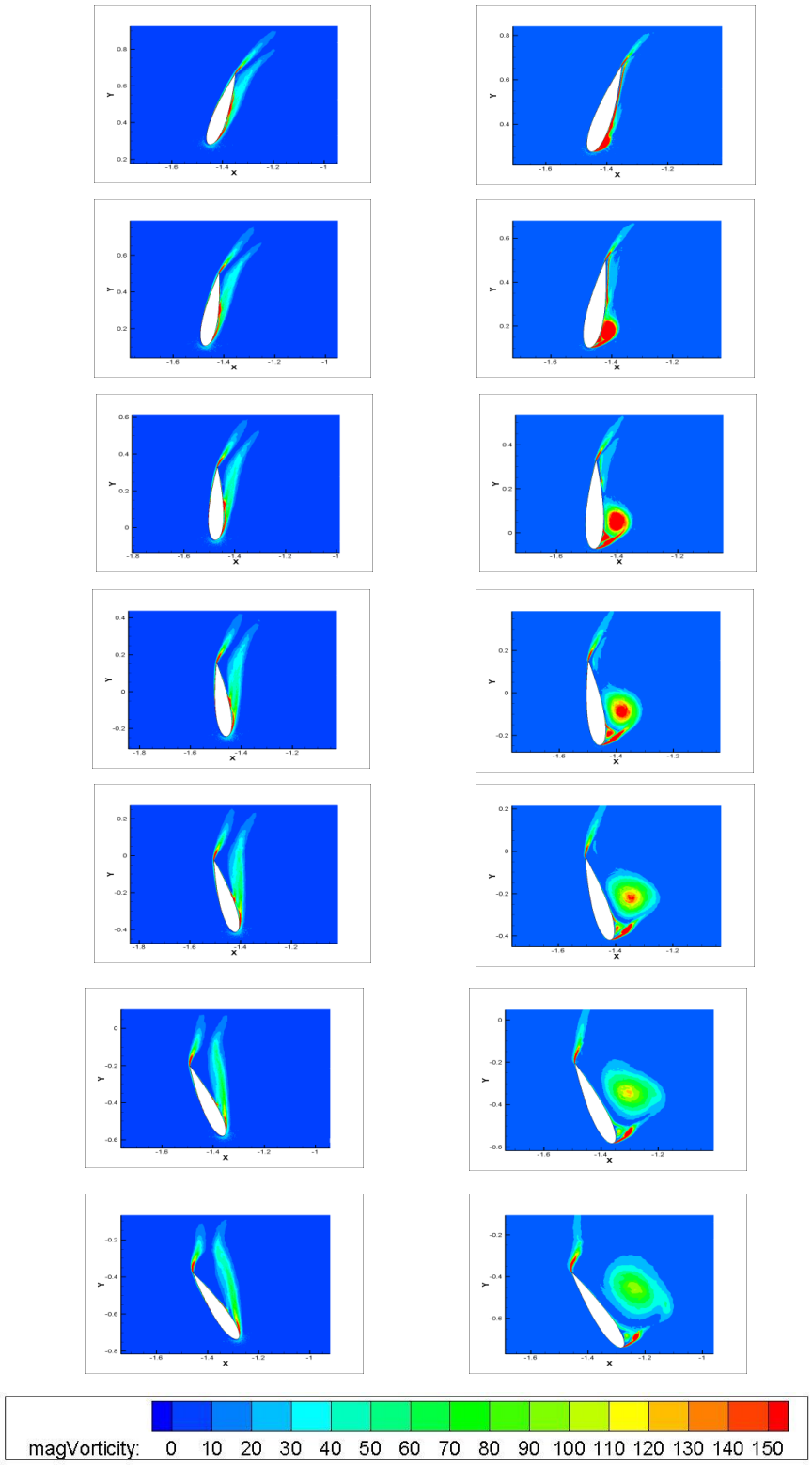

Figure 3.21. Comparison between N = 2 (left) and N = 4 (right) at the same circumferential positions. The case of N = 4 is showing the evolution of dynamic stall from θ = 166° to θ = 207° which leads to the large drop in power coefficient discussed previously. For the same angles the case of N = 2 a LEV does not form and eventually separate even though they are at the same advance ratio of λ = 1.75

negative pointing to dynamic stall. On plotting vorticity contours between θ = 166° and 207°, the formation and shedding of a stalled LEV is clearly evident in Figure 3.21. In contrast when only two blades are present (N=2), no such phenomenon is observed. Once again, there is no obvious explanation as to why dynamic stall occurs for N=4 but not for N=6 which would have more wake interactions between consecutive blades and thus have a greater propensity towards stall. This interaction can be seen in the form of streamlines shown in Figure 3.22. For N=4, there is clear indication of large scale vortex structures in the streamline patterns.

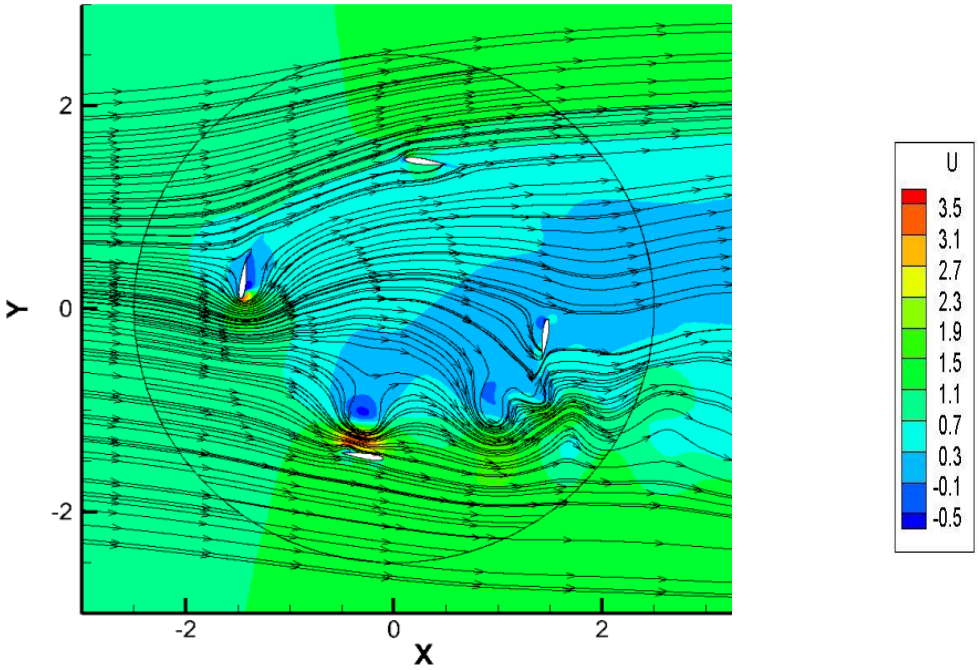

Figure 3.22. Streamwise velocity and streamlines for N = 4

A more accurate representation of the velocities and effective angles of the blades of the VAT were desired to gain a better understanding of what causes the different lift and drag profiles, as well as dynamic stall. Data was extracted from a distance of c/4 in front of blade 1 at various points throughout the fourth cycle of the VAT. From this data the relative velocity magnitude was plotted for values of N = 2, 3, 4, 6 and compared to the expected idealized value for the advance ratio of 1.75 seen below in Figure 3.23. For the first half of the cycle all of the cases match reasonably well with the expected relative velocity magnitude with the exception of N = 4, where dynamic stall was seen. For the other cases the

expected trend was followed for the most part. In general, more blades in the turbine, lead to more interactions between the blades, larger wakes, leading to a larger difference in the second half of the cycle. It should be noted that in the last quarter of the cycle, the case of N = 6 shows better comparison than the other cases which is not expected.

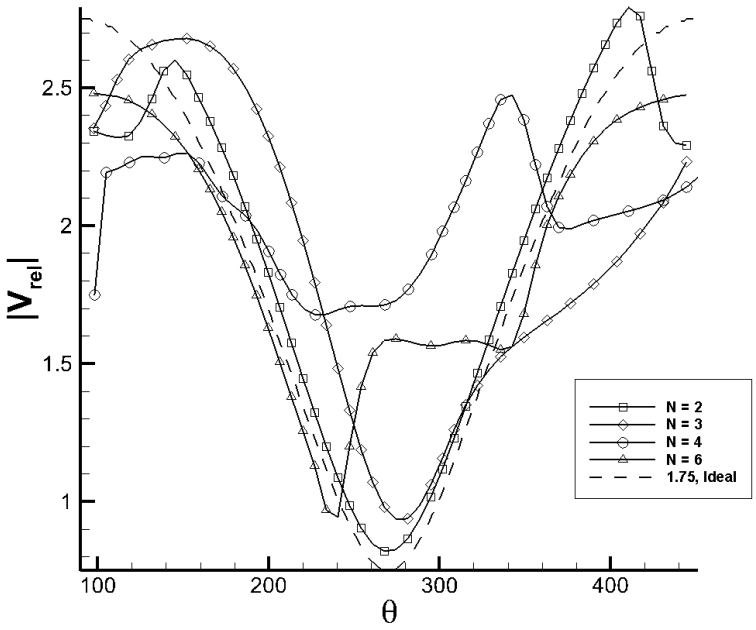

Figure 3.23. The relative velocity magnitude seen by blade 1 compared to the expected idealized velocity magnitude for values of N = 2, 3, 4, 6

The effective angle of attack for the same four cases was then compared to the expected ideal effective angle of attack in Figure 3.24. For all of the cases except N = 4 it is shown that as the number of blades increase, the deviation from the ideal effective angle of attack increases. This is again believed to be due to more interactions between the blades and the larger wake that travels downstream. For the entire cycle, the case of N = 2 almost exactly matches the expected ideal effective angle of attack, similar to what was seen when looking at the relative velocity magnitude. For the cases of N = 3 and N = 6,the ideal effective angle of attack under predicts the effective angle of attack in the first half of the cycle and over predicts it for the majority of the second half of the cycle. The case of N = 4 shows a large deviation from the ideal effective angle of attack throughout the entire cycle. Dynamic stall was seen to occur between

166° and 207°. During this period of the cycle the blade sees an effective angle of attack that changes from -12°, to -15°, and then back to -13°. This is the same general pattern (at a different azimuthal position and different magnitude of effective angle of attack) that was seen in the case of $\lambda = 2.5$.

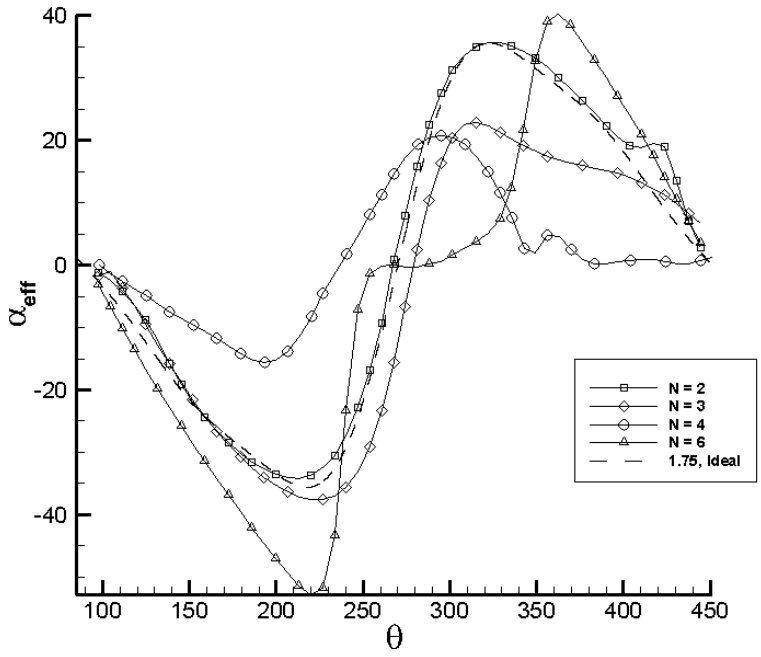

Figure 3.24. The effective angle of attack seen by blade 1 compared to the ideal effective angle of attack for cases of N = 2, 3, 4, 6

The lift and drag for a single blade averaged over the entire cycle were compared for the different solidities seen in Figure 3.21. The expression used to obtain lift and drag from the x- and y- components of the force vector are given in Appendix B. It is noted that in calculating the lift and drag forces, the idealized effective angle of attack and approach velocity are used in Figures 3.25 to 3.28. Appendix C shows results with the actual effective angle of attack and approach velocity from Figure 3.23 and 3.24. While there are differences between the two approaches, the results show the same trends and thus we have chosen to present the results in the idealized setting.

In these cases, both the coefficients and forces follow the same trends. The lift coefficient drops as the number of blades in the turbine increase except in the case of N = 4 where there is a slight increase, which

is consistent with the earlier result that shows that dynamic stall does not have a large impact on the lift force. The decrease in the lift coefficient as the solidity increases is a result of increased interaction with trailing wakes of blades in front. With a larger number of blades there is a smaller phase difference between the blades causing more interaction. The drag profile shows an interesting trend. There is a slight increase from N = 2 to N = 3, a large jump from N = 3 to N = 4, followed by a large drop from N = 4 to N = 6. This large peak in the drag coefficient is due to the occurrence of dynamic stall seen for the case of N = 4 in Figure 3.21.

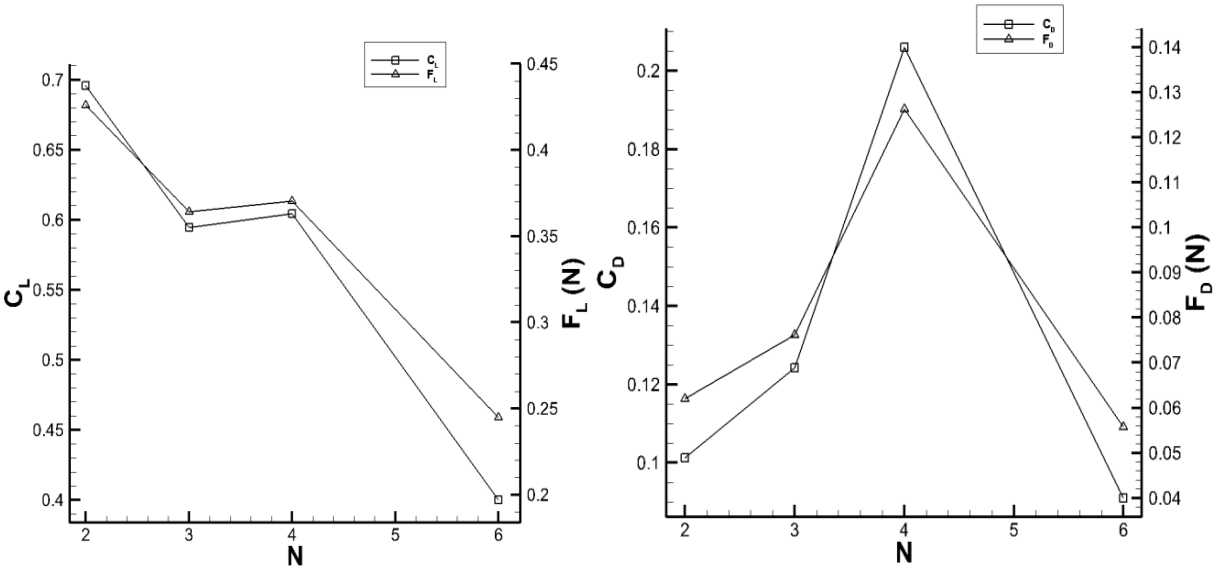

Figure 3.25. The cycle averaged lift (left) and drag (right) for a single blade at different solidities

To get a more in depth look at the effects of lift and drag on the turbine performance the tangential thrust force is broken down into its lift and drag components seen in Figure 3.26. As with the cases of different advance ratios, the lift component of the tangential force is larger than the total tangential force. Again this is due to the negative effects of the drag component. The lift component decreases as the number of blades increase, at an almost constant rate. However, the total tangential force stays almost constant from N = 4 to N = 6. For the case of N = 6 there is a significant reduction in the magnitude of the drag component of the tangential force. The case of N = 4 shows the largest negative drag component due to dynamic stall. The variation of the lift and drag components of the tangential force

can be analyzed to get additional information on this effect in Figures 3.27 and 3.28 respectively. For the first half of the cycle the lift component is largely positive with the case of N = 2 having the largest force. The next highest case is N = 4 which is surprising since N = 3 showed a higher average lift force for the entire cycle. The cause for this is shown in the second half of the cycle where the case of N = 3 gives a period of positive component of lift.

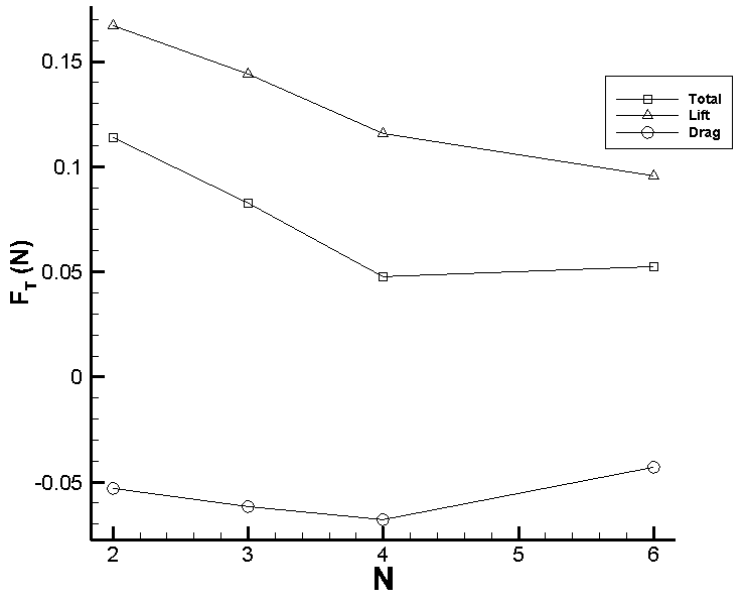

Figure 3.26. The cycle averaged lift and drag forces in the tangential direction and total tangential force for different number of blades

In this region from θ = 270° to 400° there is a large positive spike in the lift component followed by a large negative spike for the case of N = 4. The stall experienced in this case allows for separated vortices to travel downstream and distort the flow more as shown in the streamlines from Figure 3.22. This is thought to cause the strange trend seen in the lift component of the tangential force during this period of the cycle. The drag component shows a similar trend to the lift component but with negative contributions to the tangential force. There is a negative peak at θ = 170° followed by a drop in the magnitude until about 270°. The case of N = 4 shows the same trend in the first half of the cycle as for the case of λ = 2.5. Instead of a drop in the magnitude of the drag component, there is another peak due to dynamic stall

occurring in the range of θ = 170° to 200°. In the second half of the cycle the cases of N = 2 and N = 3 show the slight negative impacts of drag. The case of N = 4, just as with the lift component of the tangential force, there is a large negative peak followed by a large positive peak from θ = 270° until about 400°. This is again thought to be due to the separated vortices traveling downstream and interacting with the blade. For the case of N = 6 there is almost zero thrust contribution from both lift and drag in the second half of the cycle. This shows that all of the power extracted for this case (and presumably cases with a larger number of blades) solely comes from the first half of the turbine. The large wake in the second half of the turbine, seen in Figure 3.20, encompassing the back of the turbine has close to zero streamwise velocity. The blades essentially see no flow causing the zero net force in this region.

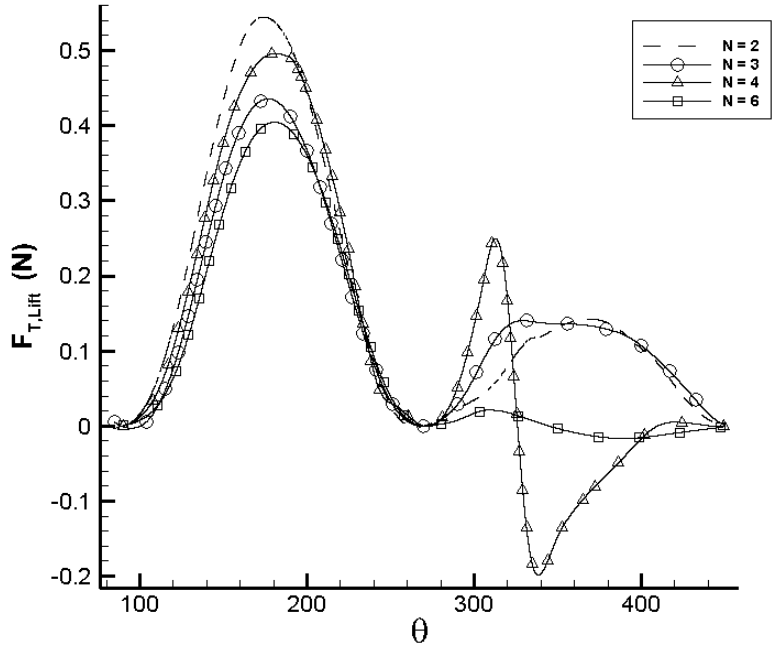

Figure 3.27. The lift component of tangential thrust force throughout the cycle for different number of blades

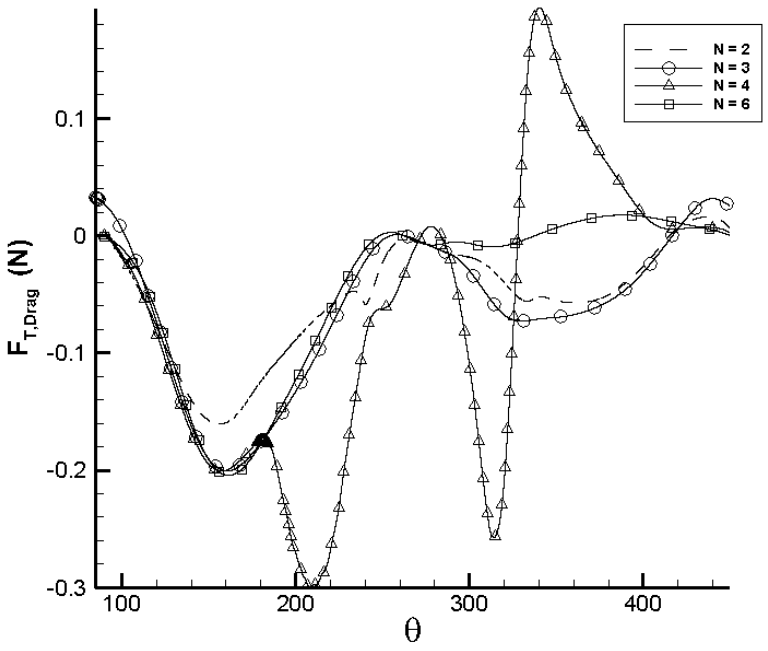

Figure 3.28. The drag component of tangential thrust throughout the cycle for different number of blades

3.5 Effects of Downstream Wake Interactions

The effect of downstream wake interactions on VAT was studied by altering the radius of the turbine. The solidity and advance ratio were kept constant at 0.81 and 1.75 respectively, while increasing the radius of the turbine. The solidity was kept constant by altering the chord length of the blade for the different cases of the radius as seen in Table 3.5.

Table 3.5. The chord length, solidity, and turbine radius to measure the effects of wake interactions

R	c	σ
0.7375	0.2	0.81
1.475	0.4	0.81
2.95	0.8	0.81

As the radius of the turbine was increased the overall power coefficient for the turbine increased as shown in Figure 3.29. It was thought that as the radius of the turbine increased, the wake from the blades on the

half would have to travel further downstream. This extra time to travel downstream would allow the wake to dissipate and thus raise the power extracted in the second half of the turbine.

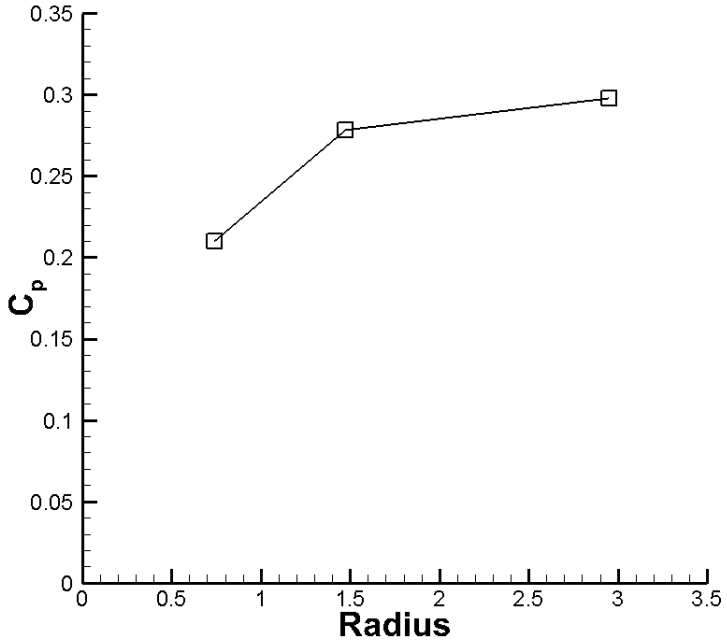

Figure 3.29. The effect of increasing the radius on the overall power coefficient of the turbine

However, when the power coefficient for a single blade is compared over a cycle for the different cases in Figure 3.30, this seems to not be the cause of the increased C_p value seen. Looking at the second half of the cycle from $\theta = 270°$ to $\theta = 450°$ there is little variation between the three cases. This is more clearly seen when comparing the streamwise velocity and streamlines between the cases of R = 0.7375 and R = 2.95 in Figure 3.31. The streamwise velocity contours between the two cases are both of the same magnitude. Looking at the second half of the cycle the contours are both of similar shape as well, with a large region of low velocity trailing from the upstream half of the turbine. The streamlines for this case are also both very similar, being almost aligned to the streamwise direction in the second half of the VAT. This effect or lack thereof points to the solidity as the important parameter which impacts wake interference in the downstream half of the turbine.

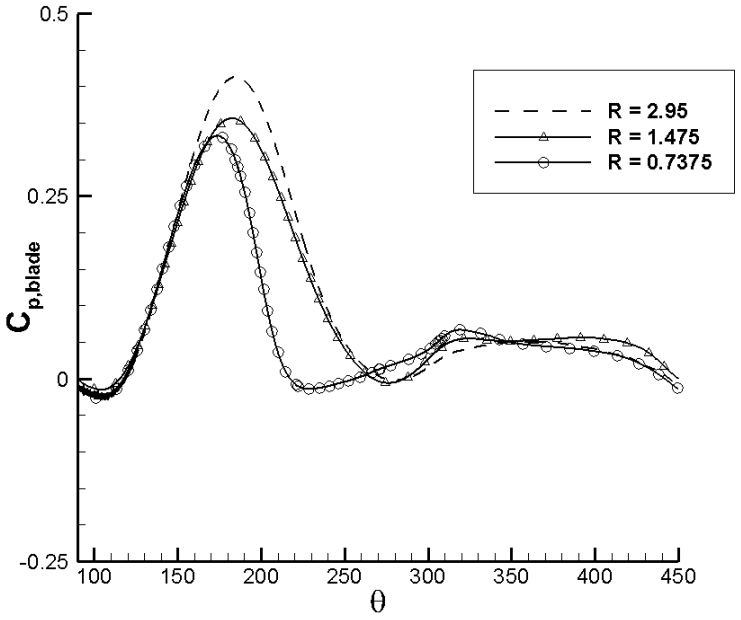

Figure 3.30. The power coefficient curve over a cycle for turbines of different radii

To determine the cause for the difference in the power coefficients, the first half of the cycle is analyzed. For the first 70° of the cycle, each of the three cases shows the same trend and magnitude of C_p. After this point the three curves diverge from one another. The case of R = 0.7375 reaches a peak and then begins to drop, while the other two cases continue to rise to a peak at a larger azimuthal angle. This effect is due to the blade interaction with the trailing wake of the blade in front. For a turbine of a smaller radius, the arc distance between two blades will be smaller and the blades will be rotating at a higher angular velocity to keep the advance ratio equal. This results in more interactions with trailing wakes thus altering the power coefficient for parts of the cycle. This interaction along with the relative velocity alters the ideal effective angle of attack at the blade and reduces the amount of torque produced.

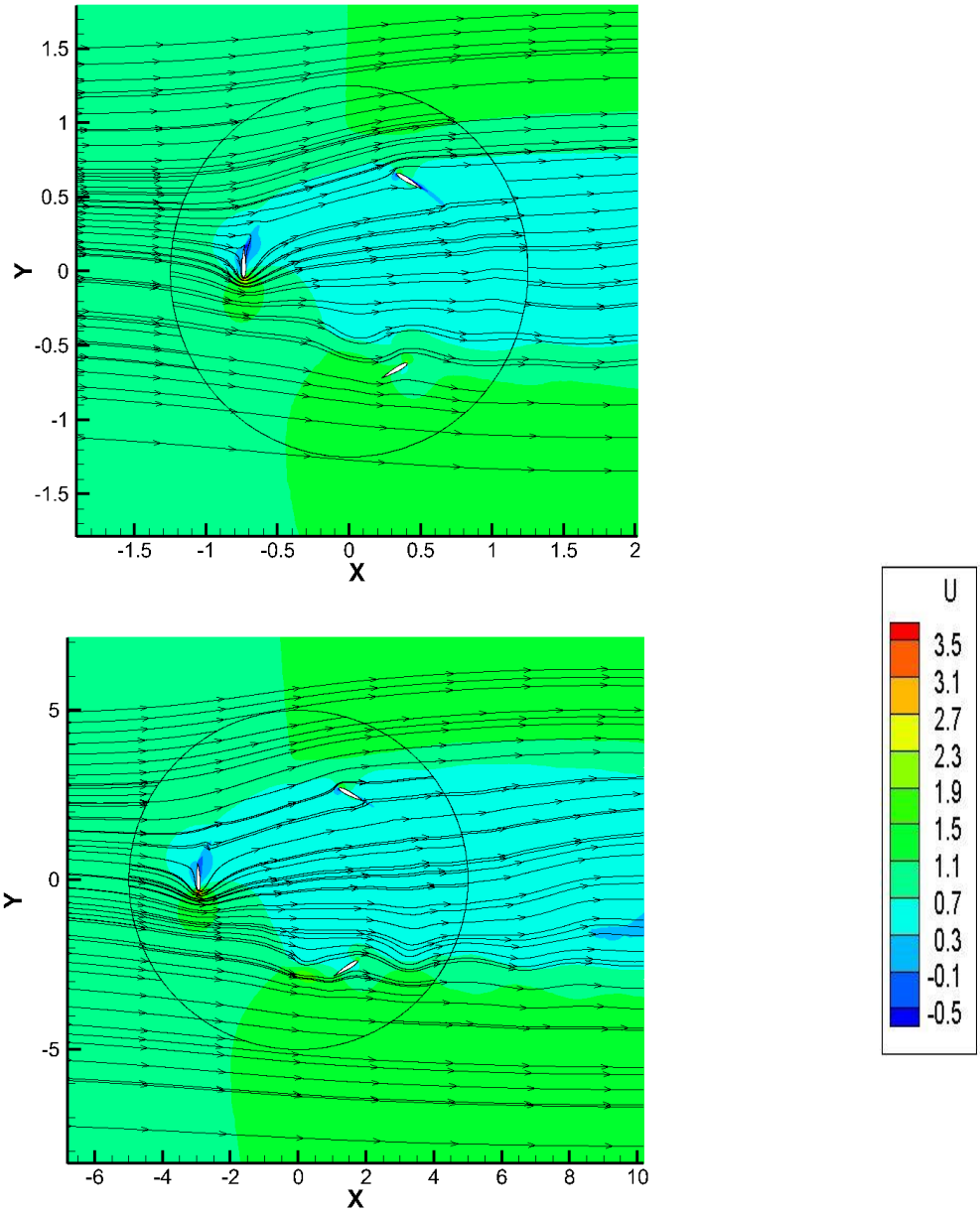

Figure 3.31. Comparison of the streamlines and streamwise velocity for R = 0.7375 (top) and R = 2.95 (bottom)

The actual angle of attack and approach velocity was extracted from a distance of c/4 in front of blade 1 at various points throughout the fourth cycle of the VAT. From this data the relative velocity magnitude was plotted for values of R = 0.7375, 1.475, 2.95 and compared to the expected idealized value for the advance ratio of 1.75 seen below in Figure 3.32. The case of R = 0.7375 has a slightly lower relative

velocity magnitude at the start of the cycle but shows otherwise good comparison to the idealized value for the remainder of the cycle. The largest radius matched the trend of the idealized profile in the first half and then slightly deviates in the second half. It should also be noted that the relative velocity magnitude for this case reaches a higher value at the start/end and a lower value at approximately halfway through the cycle.

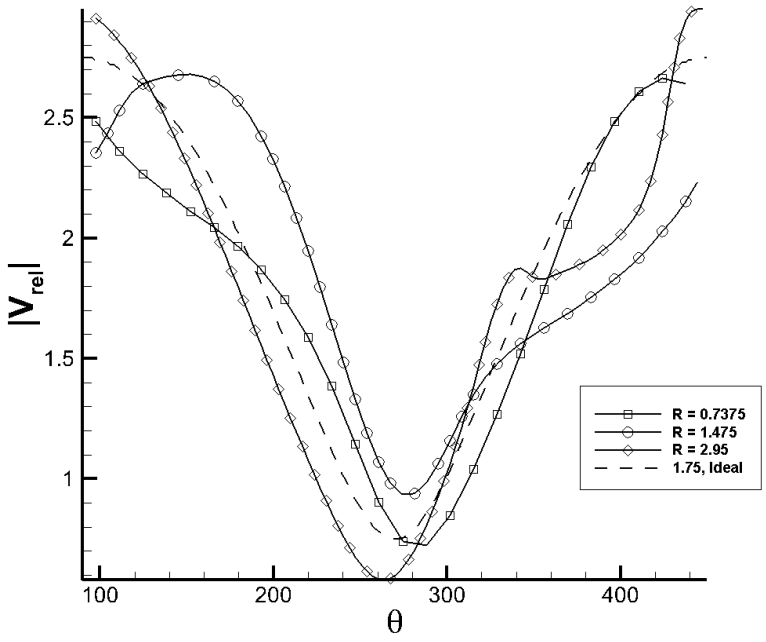

Figure 3.32. The relative velocity magnitude seen by blade 1 compared to the expected idealized velocity magnitude for values of R = 0.7375, 1.475, 2.95

The effective angle of attack was then compared to the expected ideal effective angle of attack seen in Figure 3.33. The smallest radius shows a much lower effective angle of attack than the ideal effective angle of attack expected for the case of $\lambda = 1.75$ in the first half of the cycle. During the second half, however, the ideal effective angle of attack under predicts what is seen for the case of R = 0.7375. The trend is the opposite for the other two cases of R = 1.475 and 2.95. For the first half, both of the cases show good comparison to the ideal effective angle of attack but then are higher during the second half of the cycle. From Figure 3.30 it was shown that during the first half of the cycle there was a noticeable

difference between the power coefficients for the three different radii. During the first half of the cycle, the effective angle of attack for R = 0.7375 is much smaller than the other two cases. However, the angular velocity is much larger for this case. As seen in section 3.3 the angular velocity has a large impact in the power coefficient of the turbine. Even though R = 0.7375 shows a much lower effective angle of attack in the front half of the turbine, the power coefficient is still similar because of the larger angular velocity.

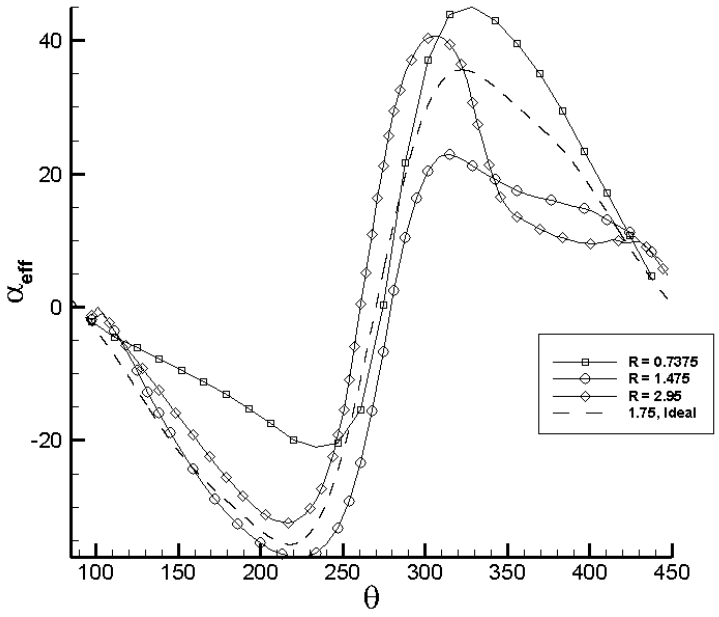

Figure 3.33. The effective angle of attack seen by blade 1 compared to the ideal effective angle of attack for cases of R = 0.7375, 1.475, 2.95

The lift and drag coefficients for the different radii can be seen in Figure 3.34. The expression used to obtain lift and drag from the x- and y- components of the force vector are given in Appendix B. It is noted that in calculating the lift and drag forces, the idealized effective angle of attack and approach velocity are used in Figures 3.34 to 3.37. Appendix C shows results with the actual effective angle of attack and approach velocity from Figure 3.32 and 3.33. Like before, we have chosen to present the results in the idealized setting.

The lift coefficient increases by 5% from the case of R = 0.7375 to R = 1.475, whereas the lift force increases by a factor of 4.5, mainly due to the increase in chord length as the radius increases (Table 3.4). The drag coefficient decreases by about 30% from the case of R = 0.7375 to R = 2.95. This decrease in drag is due to the larger distance between the blades as the radius of the turbine increases, reducing the impact of the trailing wake of the blade in front. At the same time, the drag force increases with radius due to the increase in chord length of individual blades.

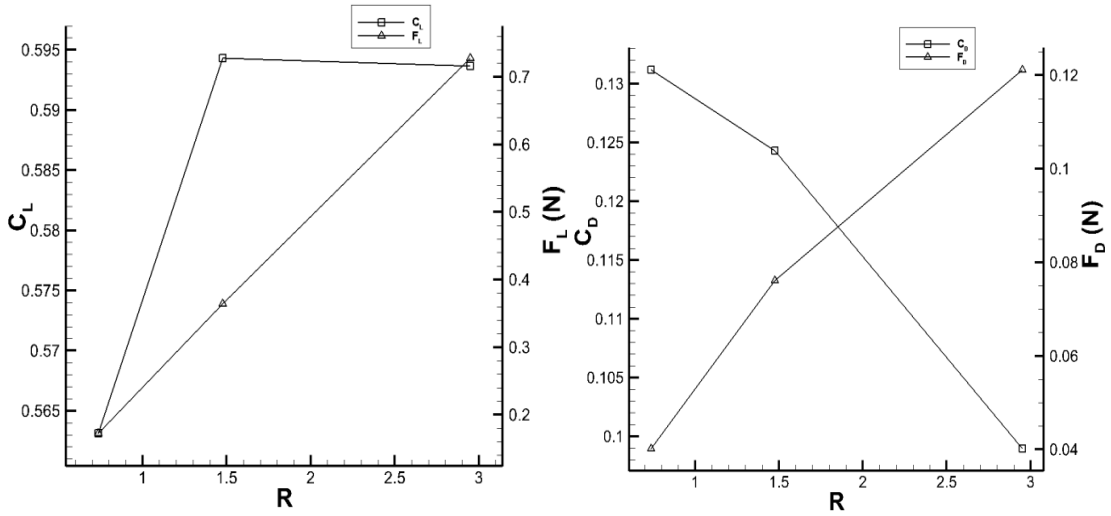

Figure 3.34. The cycle averaged lift (left) and drag (right) for a single blade at three different radii

The tangential thrust force is broken down into components of lift and drag to determine the impact these forces have on the performance of the turbine in Figure 3.35. As the radius of the turbine increases, the lift component of the tangential force greatly increases, while the drag component becomes increasingly negative. The cause of this can be better seen by examining the lift and drag component of the tangential force throughout the entire cycle in Figures 3.36 and 3.37 respectively. All three of the turbine radii cases show similar trends in both lift and drag. For the first 100° of the cycle there is a large spike in the lift component of thrust force.

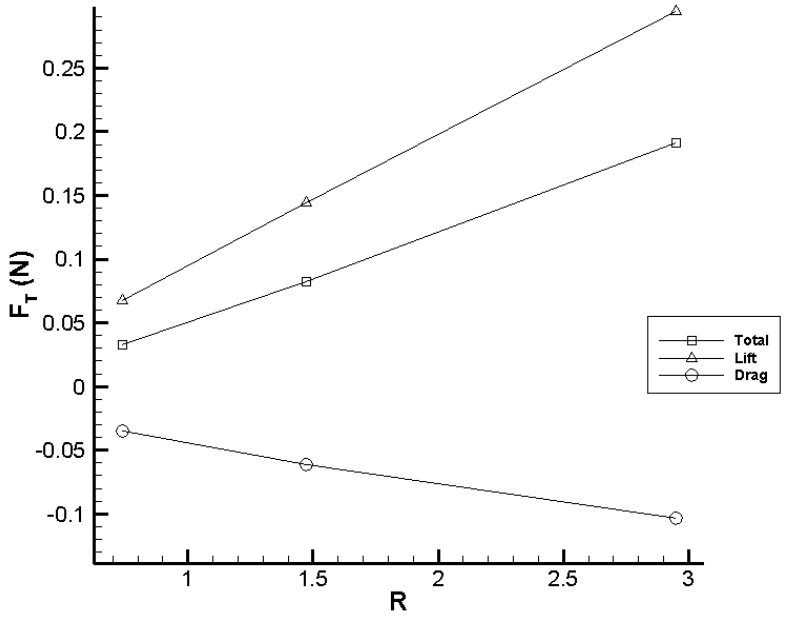

Figure 3.35. The cycle averaged lift and drag components and total thrust force for different turbine radii

There is then a period between 210° and 300° where there is no generation of lift forces in the tangential direction. For the remainder of the cycle there is a slight production of lift in the tangential direction. The larger radius turbine generates more tangential lift than that of the smaller radius turbine. The efficiency of the larger turbine is only slightly larger than the smallest because it also generates a large negative drag thrust force that offsets the positive thrust. The difference in the power coefficient curve in Figure 3.30 occurs at value of $\theta = 160°$. At this point the case of $R = 2.95$ is generating a significantly larger drag and lift in the tangential direction. There is also a larger difference between the case of $R = 0.7375$ and the larger radii because of the second negative peak seen at $\theta = 200°$ for $R = 0.7375$. This accounts for the difference in the power coefficient in the first half of the cycle and increased overall efficiency of the turbine.

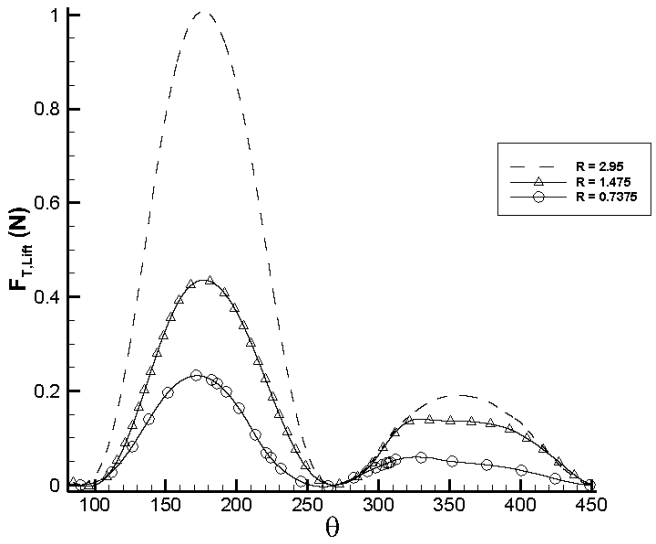

Figure 3.36. The lift component of thrust force throughout the cycle for different turbine radii

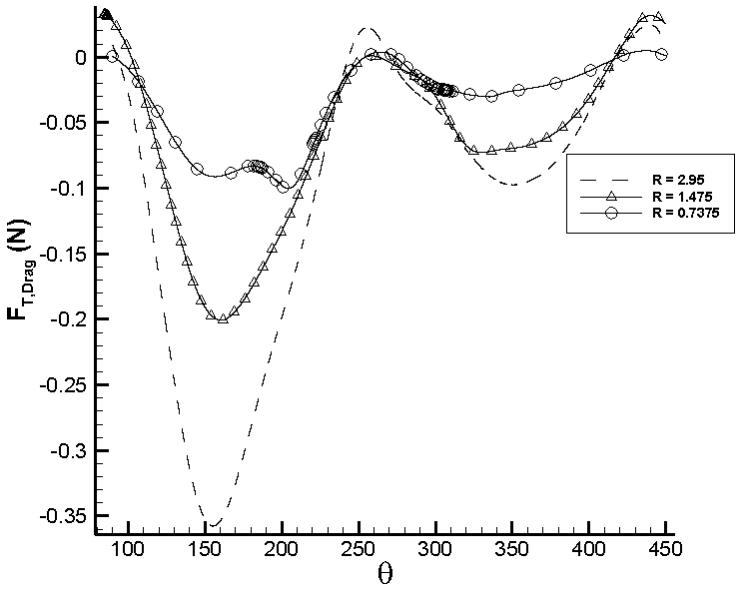

Figure 3.37. The drag component of thrust force throughout the cycle for different turbine radii

3.6 Conclusions

The aerodynamic performance of an H-rotor VAT was studied at a nominal Reynolds number of 500,000 using the PimpleDyMFoam solver in OpenFOAM. To simulate the movement of the VAT the

AMI method was used to rotate the mesh. The k-ω SST turbulence model was used to model the turbulence based on previous studies showing good representation with experimental results.

To test the effect of the advance ratio on VAT performance the rotational velocity of the turbine was altered. It was found that as the advance ratio increased, the power coefficient increased. This trend continued to a point where the power coefficient dropped off steeply. This was shown to be a result of dynamic stall in the front half of the turbine. The phenomenon of dynamic stall causes a steep decrease and negative values of the power coefficient as the LEV forms and separates from the blade surface.

The impact of solidity on VAT performance was tested by changing the number of blades in the turbine. As the number of blades in the turbine increase, the amount of power extracted per blade decreases. However, since there are more blades in the turbine the overall power coefficient for the turbine increases. When there are fewer blades in the turbine there is less interaction with the trailing wake of the blade in front, causing a larger power coefficient per blade. When the number of blades was increased to four, the blades experienced dynamic stall in the front half of the cycle. This is interesting since this is the only case where this was seen. It is thought to be due to a combination of the relative velocity and the trailing wake altering the ideal effective angle of attack to the dynamic stall point.

Lastly the effect of downstream wake interaction on the turbine performance was investigated by increasing the radius of the turbine while keeping all other non-dimensional parameters equal. As the radius of the turbine increased, the overall power coefficient did as well. It was seen that the radius did not have an impact on the blade performance in the second half of the turbine. Instead, there was a significant impact during the front half of the cycle. This was hypothesized to be due to the trailing wake of the blades having less of an impact on the turbine with a larger radius.

For all cases it was shown that the lift force on individual blades generate a large positive thrust in the tangential direction that is slightly offset due to the overall negative thrust from the drag force throughout the cycle. In all the cases studied in this paper, starting at approximately $\theta = 200°$ there is a small positive thrust generated from the drag that helps to increase the efficiency of the turbine. When dynamic stall occurs for the cases of $\lambda = 2.5$ and $N = 4$, it was found that the drop in efficiency is due to the large

increase in drag force rather than a precipitous drop in lift. Instead of the drag in the tangential direction dropping (as with all other cases) there is a second, larger spike in the drag component. The exact reason as to what conditions lead to dynamic stall in these cases remains unclear.

The idealized relative velocity magnitude and ideal effective angle of attack was compared to the actual values found from the computations. For most of the cases there was a deviation from the expected idealized values. There was good comparison for both the relative velocity magnitude and effective angle of attack during the first half of the cycle where downstream wake effects are minimal. The second half showed a much larger difference from the expected values, again due to the wake effects. From this data the cause of dynamics stall was further investigated in the cases of $\lambda = 2.5$ and $N = 4$. A single explanation for the onset of dynamic stall in the VAT was not found. A combination of the effective angle of attack, rotational velocity, and blade to blade complex interactions all contribute to the onset of the dynamic stall phenomena.

At specific H-rotor VAT parameters, it was found that the turbine experiences dynamic stall that significantly decreased the amount of power extracted from the flow. It is recommended that future work be conducted to further investigate the conditions that lead to dynamic stall in H-rotor VATs.

Chapter 4

VAT Twisted Blade Profile

In the previous section it was found that when dynamic stall occurred in the VAT cycle, it had a large negative impact on the power coefficient of the turbine. This chapter investigates blade profiles which are tolerant to dynamic stall and maintain high lift over a range of Reynolds numbers and angles of attack. The modified blade was twisted along the span in a way that one end remained at an angle of attack of 0° to the incoming flow and the opposite end was at some maximum angle of attack on a symmetry plane giving it a three-dimensional profile. Instead of simulating the full VAT motion, in an effort to reduce the computational cost, two separate tests were run: a static twisted blade, as well as a twisted blade with an effective VAT motion. To test to see if the twisted blade profile showed improvements, 2D cases at various angles of attack were also run for comparison. For the static test both OpenFOAM and GenIDLEST were used to perform calculations at Reynolds number 10,000. It was found that for the static twisted blade profile the lift to drag coefficient ratio showed similar results when compared to a 2D blade at an angle of attack that was half of the maximum twist angle. An effective VAT pitching motion was given to the twisted blade at a maximum twist angle of 20° and compared to a 2D blade with the same motion. There was a large performance increase for the twisted blade due to high lift production during the downstroke. This was a result of a large stalled vortex which remained in the vicinity of the blade surface during the downstroke increasing the pressure differential between the upper and lower surface of the blade.

4.1 Computational Domain

4.1.1 OpenFOAM

To simulate the VAT motion for three 2D blades at different advance ratios a mesh size of 220,000 quadrilateral cells was used and took approximately 124 hours to run on 32 processors. To extend this to

the twisted blade profile there would be a requirement of about 300 cells in the z-direction to resolve the flow in the spanwise direction. The size of the mesh would then come out to about 66 million cells which was deemed too computationally expensive to calculate. Instead the flow over a single, stationary blade was calculated with a mesh size of about 8 million cells. The mesh in the near region of the blade and the mesh in the boundary layer can be seen in Figure 1. The domain extended 20 chords in the streamwise and cross-stream direction. There was also an area of refinement up to a radius of one chord around the blade to capture the vortex shedding. A wall boundary was placed on the end of the blade at an angle of attack of 0° and a symmetry condition was placed on the opposite end of the span. Because the blade was static, and a RANS procedure was used, no time integration was done, greatly reducing the run time for all cases. For each blade profile tested, 64 processors were used with a run time of about 36 hours.

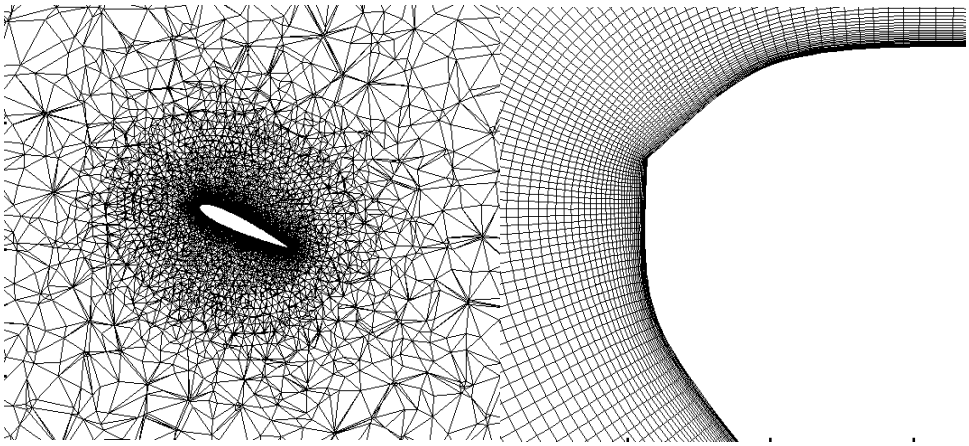

Figure 4.1. The mesh of the near region of the twisted blade (left) and the boundary layer mesh (right) used in OpenFOAM.

4.1.2 GenIDLEST96

For all calculations done in GenIDLEST a Large Eddy Simulation (LES) was used with the Dynamic Smagorinsky sub-grid scale (SGS) model in conjunction with the Immersed Boundary Method (IBM) to solve the flow around the twisted blade. An orthogonal mesh was used with approximately 50 million cells for all calculations with dimensions 520 x 420 x 250 in the x, y, and z-direction. Plots of the grid resolution with space can be seen in Figure 2 with the blade location marked in each figure. The domain

extended 19 chords in the streamwise direction and 15 chords in the cross-streamwise direction. In the region close to the blade a constant mesh size of 5.25×10^{-3} was used so that the y-plus on the surface of the blade was on the order of 1.0. The static calculations were time-integrated until a stationary state was reached based on the lift and drag profile; the effective VAT motion case was time-integrated for three cycles. Static cases were run on 200 processors and took about 96 hours to reach a stationary state and, the effective motion case was also run on 200 processors and took about 72 hours to run three cycles.

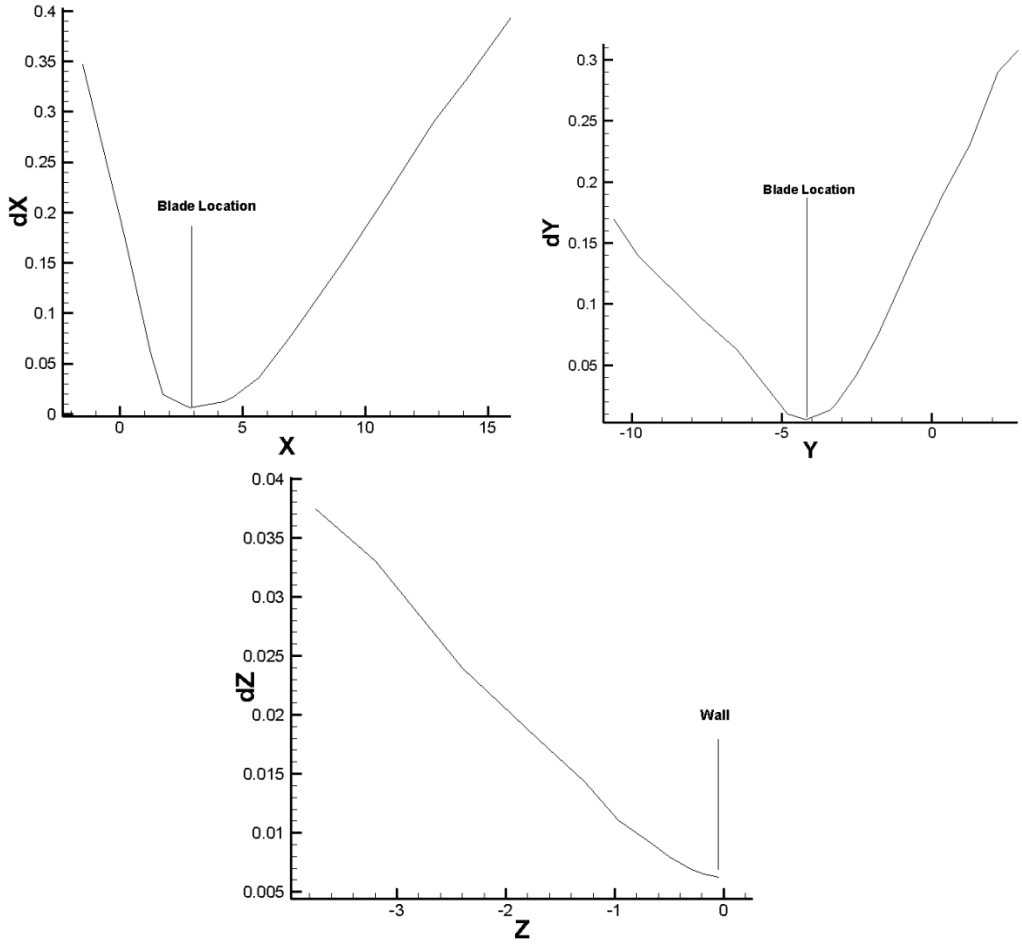

Figure 4.2. The cell size with respect to grid location in the x, y, and z direction for the orthogonal Cartesian mesh used with GenIDLEST

4.2 Stationary Twisted Blade

The CAD model of one of the twisted blade profiles (50° max twist angle) can be seen in Figure 4.3. Starting from 0º, the span the blade is slowly twisted upward until a maximum angle is reached. Once that point has been reached (half the span) the blade is then twisted back until it reaches 0° angle of attack. A symmetry condition is enforced at the maximum angle so only half of the blade is simulated. By twisting the blade, the effective flow angle of attack changes with its spanwise distance. This was done in an effort to give some stabilization to the Leading Edge Vortex (LEV) that forms in certain VAT configurations (as shown in Chapter 3) and increase the overall efficiency of the turbine.

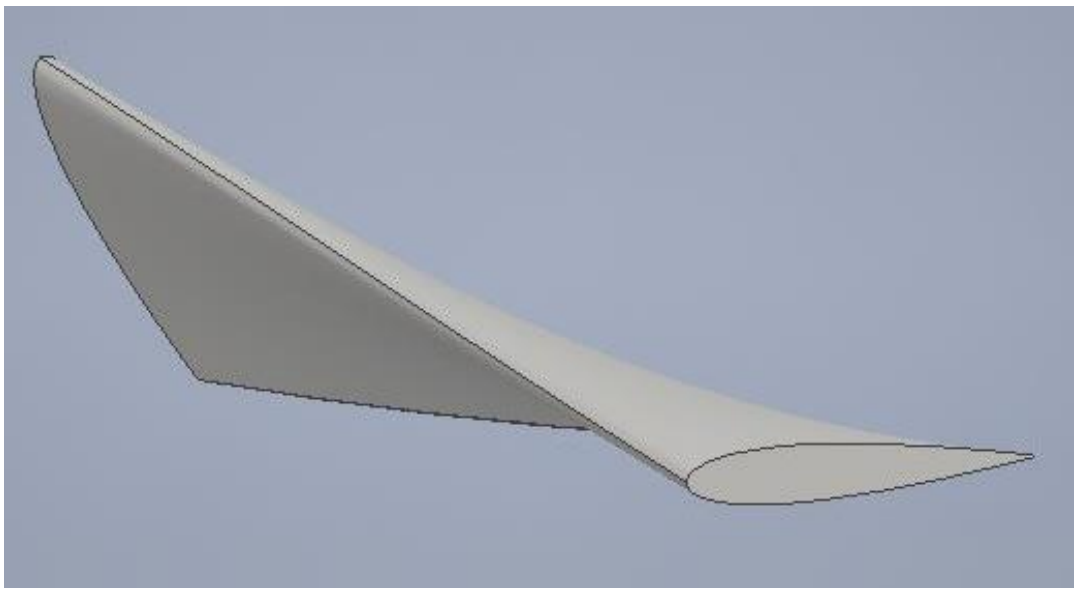

Figure 4.3. CAD model of twisted blade profile with 50° maximum twist angle

Before the twisted blade profile tests were run, the mesh was validated in 2D space with an airfoil at static angles of attack in both OpenFOAM and GenIDLEST. In OpenFOAM three 2D cases were done at Re = 160,000 to compare to experimental data from Sheldahl and Klimas [45]. No experimental data could be found for NACA 0015 airfoils at Re = 10,000 so results from OpenFOAM and GenIDLEST were compared to one another. A summary of all of the static runs can be seen in Table 1.

Table 4.1. A list of all of the static cases that were run using both GenIDLEST and OpenFOAM

Reynolds Number	2D/3D	Static Angle/Max Twist Angle	Code
160,000	2D	10	OpenFOAM
160,000	2D	20	OpenFOAM
160,000	2D	40	OpenFOAM
10,000	2D	5	GenIDLEST
10,000	2D	10	GenIDLEST
10,000	2D	20	GenIDLEST
10,000	2D	30	GenIDLEST
10,000	2D	5	OpenFOAM
10,000	2D	15	OpenFOAM
10,000	2D	20	OpenFOAM
10,000	2D	30	OpenFOAM
10,000	3D	20	GenIDLEST
10,000	3D	50	GenIDLEST
10,000	3D	30	OpenFOAM
10,000	3D	40	OpenFOAM
10,000	3D	50	OpenFOAM

The comparison of the lift and drag coefficients for the 2D static blade at Re = 160,000 can be seen in Figure 4.4. The lift coefficient shows deviation from the experimental data while the drag coefficient shows good comparison at all the angles of attack tested. The lift coefficient shows about a 12% difference from the experimental data at both 10° and 40° angles of attack. However, there is a much larger discrepancy shown at 20°. From Sheldahl and Klimas it was shown that this is the region where static stall occurs for a NACA 0015 airfoil at Re = 160,000. In the case of static stall the k-ω SST model must show significantly less separation to account for the lift coefficient error of 34%. This leads to the

conclusion that the k-ω SST model as implemented in OpenFOAM does not perform well when massive separation occurs.

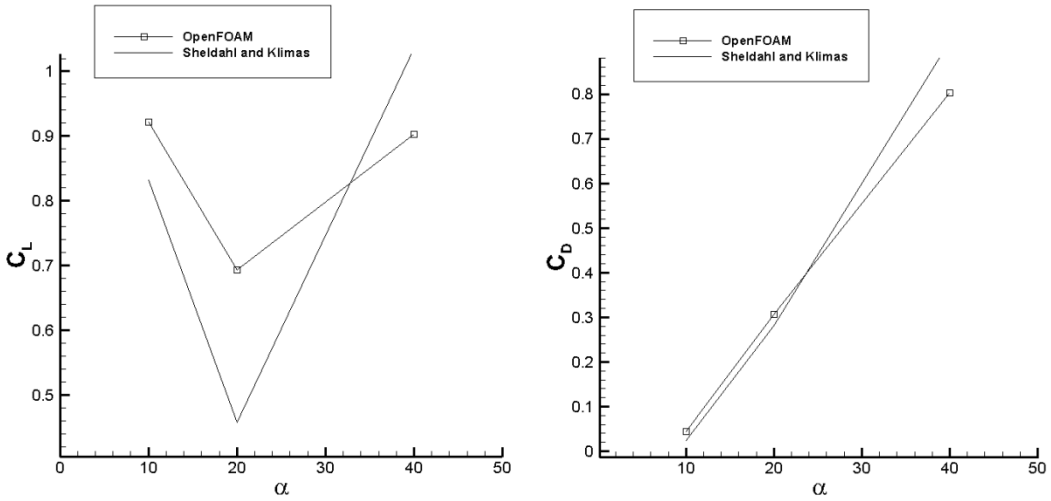

Figure 4.4. Lift and drag coefficient comparisons with experimental data at Re = 160,000

The lift and drag coefficient at Re=10,000 for the 2D static cases are shown in Figures 4.5 and 4.6, respectively. Both OpenFOAM and GenIDLEST show almost identical results for the drag coefficient, with the results from OpenFOAM showing a slightly higher value. However, there are differences in the lift coefficient prediction. For all angles of attack GenIDLEST shows a lower overall lift coefficient, most notably at the lower angles of attack. The calculations in OpenFOAM are done with RANS using the k-ω SST turbulence model which models all of the turbulence in the flow and tends to dampen out the solution. For the 2D static blade a DNS was done with GenIDLEST to resolve all of the scales. The fact that a RANS model was used when the flow is essentially laminar (Re = 10,000) could also be a cause for the larger lift coefficients seen, especially at low angles of attack where little or no separation occurs. Another factor that could impact the solution was that in OpenFOAM, first order upwinding was used as compared to second-order central difference in GenIDLEST. Since the results from OpenFOAM and GenIDLEST show reasonable agreement, it was determined the current mesh was acceptable for the twisted blade calculations.

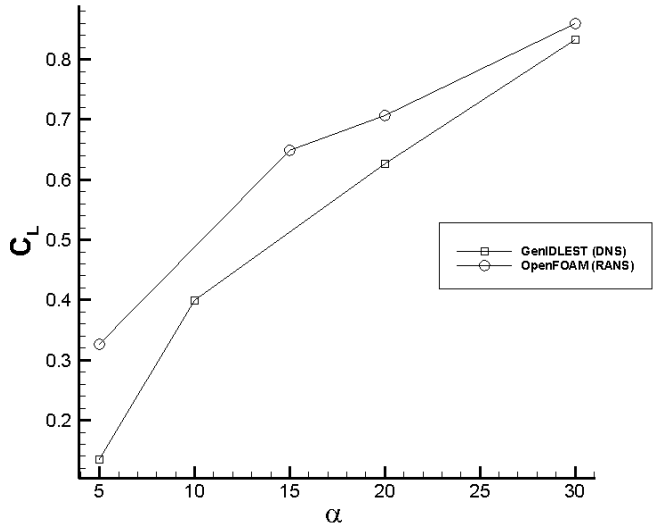

Figure 4.5. Lift coefficient comparison between OpenFOAM and GenIDLEST at Re = 10,000

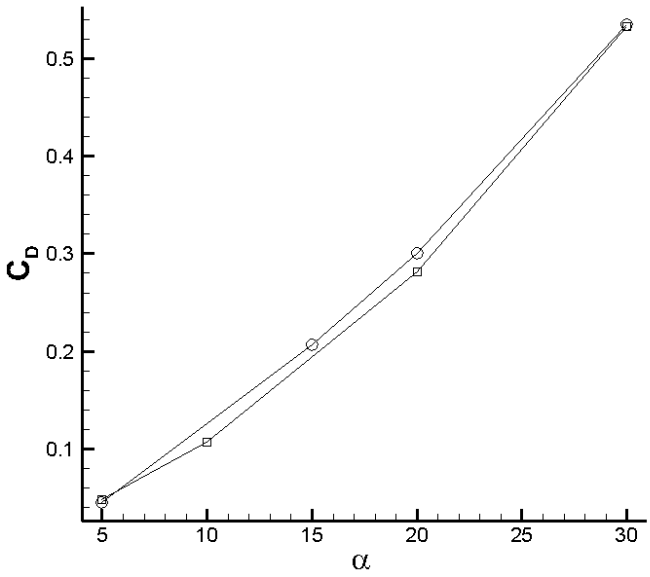

Figure 4.6. Drag coefficient comparison between OpenFOAM and GenIDLEST at Re = 10,000

In OpenFOAM three cases were run with maximum twist angles of 30°, 40°, and 50°, in GenIDLEST two cases were run at maximum twist angles of 20°and 50°.The comparison between the lift and drag coefficient of the twisted blade profiles can be seen in Figures 4.7 and 4.8, respectively. For all of the twisted blade profiles the cases run in OpenFOAM showed a much higher lift coefficient than that from GenIDLEST. When comparing the maximum twist angle of 50° at a Reynolds number of 10,000 OpenFOAM gave a lift coefficient that was 1.44 times larger. As was the case with the 2D static angles of

attack, this difference is due to how the different programs handle the turbulence. In OpenFOAM the k-ω SST RANS model was used to model all scales of turbulence and in GenIDLEST LES was used to resolve the large scales and model the small scales. It was also shown in the 2D cases that OpenFOAM predicted a much larger lift coefficient than GenIDLEST at lower angles of attack. Again this could be due to using a RANS model and its limitation in adjusting to the relatively low Reynold's number. Also it was shown that when comparing the lift coefficient at Re = 160,000 to experimental results, the model performed poorly when separation was seen at the static stall angle of attack. The model predicted a lift coefficient that was 34% higher than the experimental value. It can be concluded from that result that the model predicts significantly less separation when stall occurs. The drag coefficient trends are similar between both OpenFOAM and GenIDLEST, with GenIDLEST giving a slightly higher overall drag coefficient, opposite of what was seen from the 2D static blade calculations.

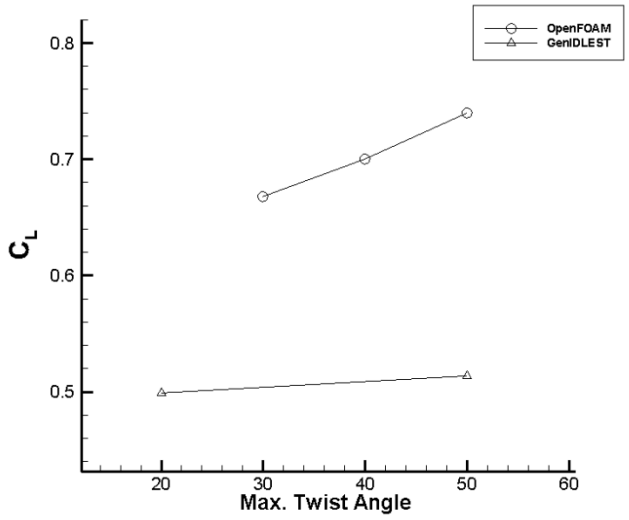

Figure 4.7. Lift coefficient comparison between OpenFOAM and GenIDLEST for different twisted blade profiles

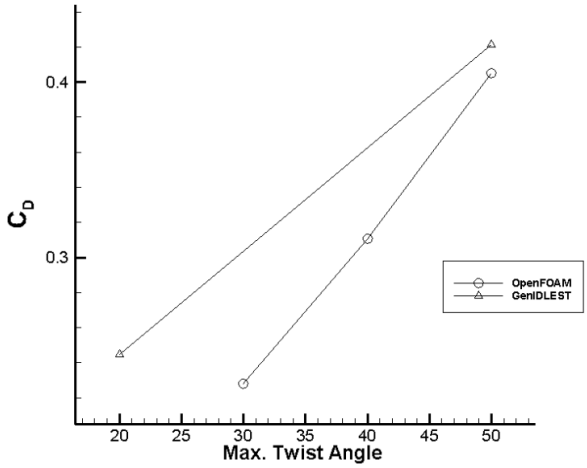

Figure 4.8. Drag coefficient comparison between OpenFOAM and GenIDLEST for different twisted blade profiles

To better understand the differences between the results seen in OpenFOAM and GenIDLEST a comparison of the vorticity contours are shown in Figure 4.9. Results from GenIDLEST were time averaged for two time units to compare to OpenFOAM. Slices at three different spanwise locations were compared for the blade with a maximum twist angle of 50°. The three slices used for comparison are at the 0° side of the blade, half of the span (25°), and at the maximum twist side (50°). It should be noted that in OpenFOAM the vorticity magnitude is presented and in GenIDLEST the extracted coherent vorticity is presented. For all three slices taken along the span there is more separation seen in GenIDLEST than in the OpenFOAM results. At 0° OpenFOAM is still showing that the flow is attached on the surface of the blade. At the same plane we see the flow separating at approximately c/4 and a large wake forming downstream of the blade in GenIDLEST. Halfway down the span at 25° the flow has now separated from the surface forming shear layers on the leading and trailing ends of the blade in OpenFOAM. A recirculation zone is also seen near the blade surface. However there is a much larger zone of separation in GenIDLEST at the same plane with the recirculation zone stretching much further downstream. The downstream wake is also much larger than what is seen with OpenFOAM. At the 50° plane the flow has detached even further and the recirculation zone has grown in the OpenFOAM results.

At the same plane in GenIDLEST there is a large turbulent zone downstream from the blade that travels multiple cord lengths downstream with a strong recirculation zone close to the blade surface.

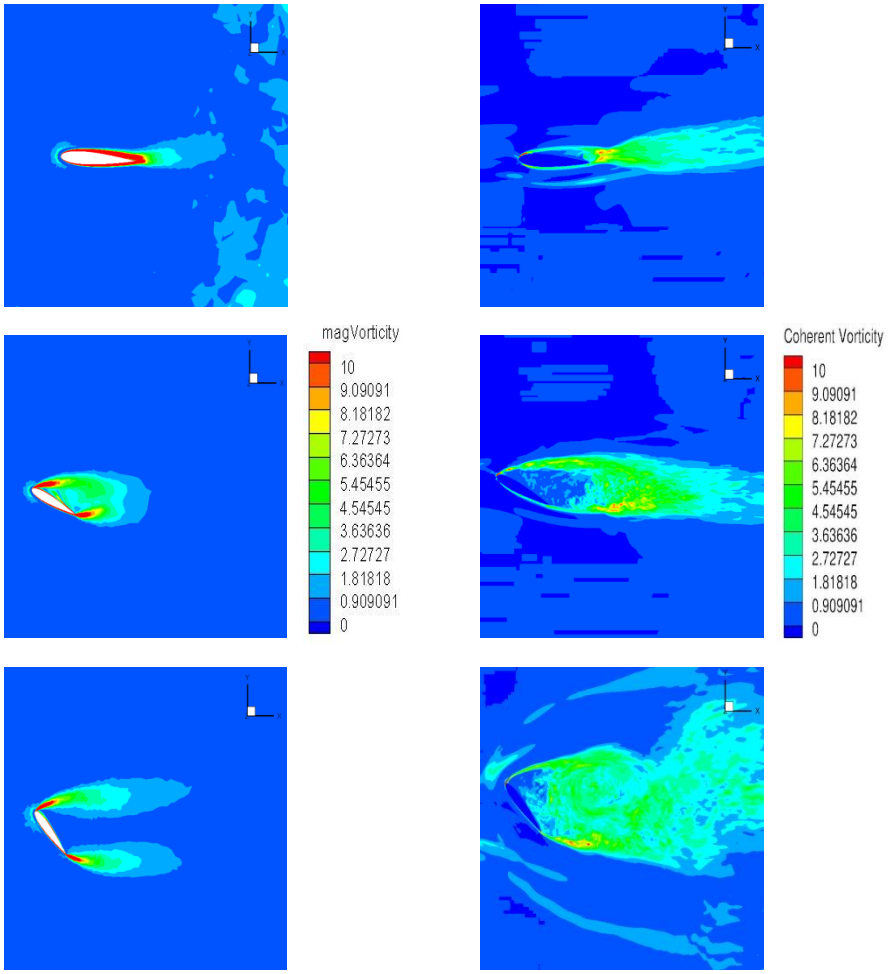

Figure 4.9. A comparison of the vorticity magnitude from OpenFOAM (left) and the coherent vorticity from GenIDLEST (right) at the 0° side of the blade (top), 25° at half the span (middle), and 50° side of the blade (bottom)

To further compare the results found from OpenFOAM and GenIDLEST, the turbulent kinetic energy was compared at three slices along the blade seen in Figure 4.10. From the time averaged results in GenIDLEST the turbulent kinetic energy is defined as $k = \frac{\overline{u'^2}+\overline{v'^2}+\overline{w'^2}}{2}$. The first slice is defined at the 0° side of the blade where there is almost zero turbulent energy extracted from the mean flow seen in

OpenFOAM. However, the results from GenIDLEST show a small region in the near wake of the blade where the turbulence is affecting the mean flow. Midway down the span at an angle of 25° there is a small region in the wake of the blade where the turbulence affects the mean flow in OpenFOAM. In GenIDLEST this effect is much larger and extends further downstream. Notably the trailing edge vortices have a large impact on the mean flow where k = 0.25. At the far end of the blade where the angle of attack is 50°, a large portion of the wake shows that the turbulence is affecting the mean flow in both OpenFOAM and GenIDLEST. Again the trailing edge vortices seem to be producing a larger turbulent kinetic energy than the leading edge in GenIDLEST. Again it is noted that the results from GenIDLEST have only been time averaged for two time units.

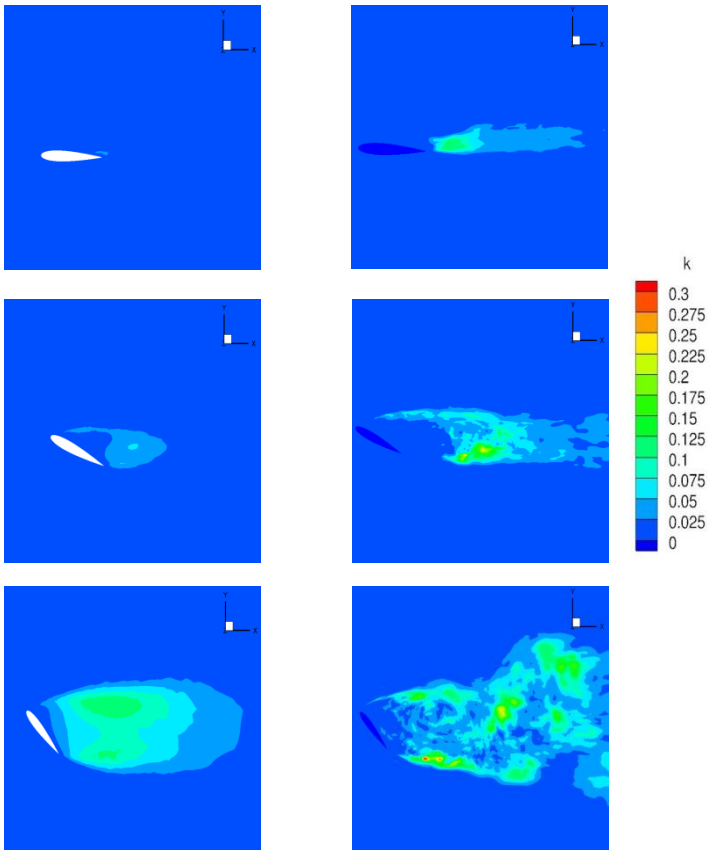

Figure 4.10. A comparison of the turbulent kinetic energy from OpenFOAM (left) and GenIDLEST (right) at the 0° side of the blade (top), 25° at half the span (middle), and 50° side of the blade (bottom)

From the previous two figures it is shown that due to the larger separation seen from the results in GenIDLEST compared to OpenFOAM, there is a lower overall lift coefficient for the maximum twist blade of 50°. These conclusions can be extended to the lower maximum angle of attack blades as well.

4.3 Effective VAT Pitching Motion

To get a more accurate representation of the improvements the twisted blade profile could have on VAT performance, an effective pitching motion was given to a twisted blade with a maximum twist angle of 20° in GenIDLEST. To match the motion of the VAT three quantities need to be replicated in the pitching motion: the effective angle of attack of the blade, the relative velocity magnitude, and the VAT frequency. To match the case of λ = 2.5, where dynamic stall had a negative impact on the efficiency of the turbine, the pitching frequency of the twisted blade, f, was set to the same value as the rotational frequency for λ = 2.5. The twisted blade was then given a pitching schedule that determines the geometric angle of attack

$$\alpha_{geo} = \alpha_0 sin\left(2\pi ft + \frac{\pi}{2}\right) \qquad \textbf{Equation 4.1}$$

where α_0 is the pitch amplitude of 15º at the zero degree side of the blade. From the pitching motion, a tip velocity can be determined

$$U_{tip} = 2\pi Rf\alpha_0 cos\left(2\pi ft + \frac{\pi}{2}\right) \qquad \textbf{Equation 4.2}$$

where R is the length of the moment arm of the blade, 0.5c.The effective angle of attack for the pitching blade is then defined as

$$\alpha_{eff} = \tan^{-1}\left(\frac{U_{tip}}{U_\infty}\right) \qquad \textbf{Equation 4.3}$$

From the tip velocity and the freestream velocity the relative velocity magnitude is defined as

$$|V_{rel}| = \sqrt{U_{tip}^2 + U_\infty^2} \qquad \textbf{Equation 4.4}$$

The comparison of the effective angle of attack and velocity magnitude between the VAT and effective pitching motion given to the twisted blade can be seen in Figure 4.11. In Figure 4.11 the effective angle of attack and relative velocity magnitude are plotted for one cycle in degrees. The start of the cycle and downstroke (α_{geo} is maximum) start at θ = 0°. The blade then travels through the downstroke and reaches the end of the downstroke/start of the upstroke at θ = 180° (α_{geo} is at the minimum value). The upstroke then ends at θ = 360° and the blade is returned to the initial position (α_{geo} is at the maximum value). Since the blade is twisted, only a slice of the blade will match the VAT effective angle of attack. For this case, the effective angle of attack is shown for the 0° side of the blade and the 20º side. In order to closely match the effective angle of attack of the VAT, the relative velocity magnitude of the pitching motion is very different from the VAT. In order to more accurately match the relative velocity magnitude either a varying inlet boundary condition or a horizontal blade motion would be required. Instead of adding further complications to the flow, the Reynolds number was increased. This was done so that the average local Reynolds number the blade sees during one cycle will match that of a VAT running at the same Reynolds number. For this case the Reynolds number was increased from 10,000 to 25,000 so that the average local Reynolds number the pitching blade sees would be approximately the same as a VAT at a Re = 10,000.

Another important parameter which we have attempted to match is the reduced frequency k, which is a measure of the rotational time scale to the time it takes for the flow to translate over the blade. Nominally, the reduced frequency, *k* is defined as

$$k = \frac{2\pi f c}{U_\infty}$$

In the framework of a VAT operating at a relatively large advance ratio, the approach velocity can be approximated by the rotational velocity to give:

$$k \approx \frac{2\pi f c}{\omega R} \approx \frac{c}{R}$$

For the VAT in this study, k ≈ 0.27. In the framework of the pitching airfoil, by keeping the frequency the same as the VAT at a value of 0.2698 for λ=2.5, and with the approach velocity approximated by U_∞=1 m/s (Re=25,000), the reduced frequency, $k \approx 0.6$, which is about a factor of two higher than in the VAT. We note that if we had endeavored to keep the reduced frequency the same between the VAT and the pitching airfoil, then we would not be able to maintain similarity in the effective angle of attack without taking other measures which would have further complicated the problem.

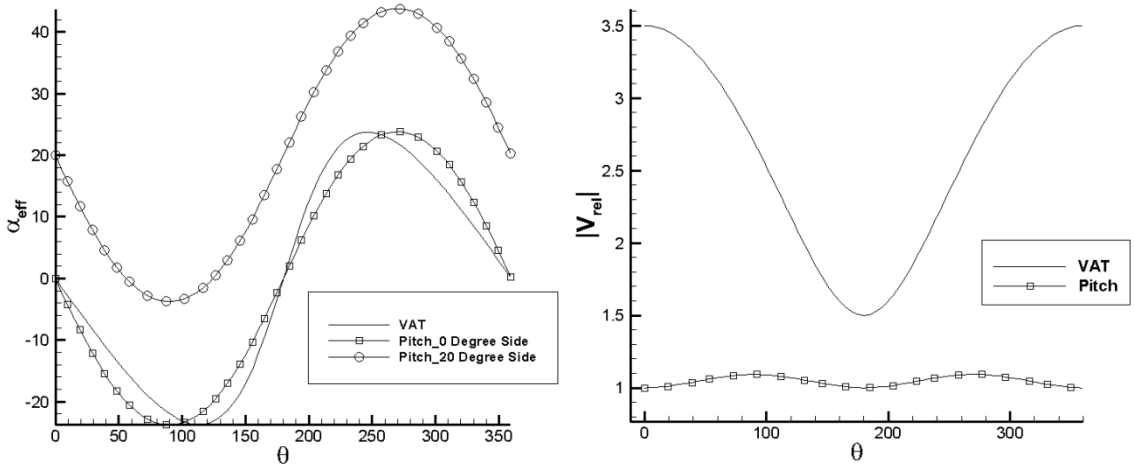

Figure 4.11. A comparison of the effective angle of attack and relative velocity magnitude between the VAT and effective pitching motion

The effective VAT pitching motion was given to both a 2D blade and a twisted blade with a maximum twist angle of 20° in order to determine if the twisted blade showed any improvements in the lift and drag coefficients. To get a fair comparison, the 2D blade motion was replicated to that of the half span slice of the twisted blade (i.e α_{eff} starts from 10° instead of 0). The forces seen by the pitching twisted blade can be seen in Figure 4.12. From the x and y forces the lift and drag can be found described as

$$F_D = F_x cos(\alpha_{eff} - \alpha_{geo}) + F_y sin(\alpha_{eff} - \alpha_{geo}) \quad \textbf{Equation 4.5}$$

$$F_L = F_y cos(\alpha_{eff} - \alpha_{geo}) - F_x sin(\alpha_{eff} - \alpha_{geo}) \quad \textbf{Equation 4.6}$$

where α_{eff} is the effective angle of attack described in Equation 4.3 and α_{geo} is the geometric angle of attack shown in Equation 4.1.

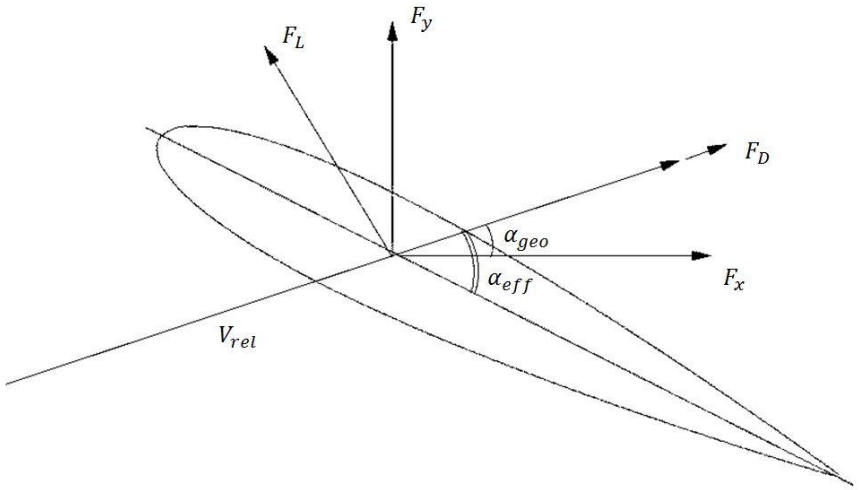

Figure 4.12. The forces seen by the twisted blade during the effective VAT pitching motion

For the twisted blade the angle of attack changes along the span of the blade, to get an accurate representation of lift and drag this must be taken into account. To take the changing angle into account in the lift and drag the blade was broken into five sections where the angle of attack was considered constant in that section. For the maximum twist of 20° blade the five sections taken were: 0 - 4 degrees, 4 – 8 degrees, 8 – 12 degrees, 12 – 16 degrees, and 16 – 20 degrees. The second assumption that was made was that the x and y force was considered to be constant along the span so that $F_x = \frac{1}{5}F_x$ and $F_y = \frac{1}{5}F_y$ in Equations 4.5 and 4.6 above. The cycle averaged lift and drag coefficients as well as the lift/drag ratio for the 2D and 3D twisted blade going through the effective VAT pitching cycle can be seen in Table 4.2. For the 2D blade the cycle average lift coefficient was found to be 0.252 and the drag coefficient was 0.0812. For the twisted blade there was a much higher lift and drag coefficient. The lift coefficient was found to

be 0.891 and the drag coefficient was 0.224. Based on the lift/drag ratio the 3D twisted blade performed much better than the 2D blade resulting in a 22% higher overall lift/drag ratio. To understand the differences between the 2D and 3D effective VAT pitching cases, the lift and drag coefficients over an entire cycle are shown for both cases are shown in Figure 4.13.

Table 4.2.The average lift and drag coefficient as well as the lift/drag ratio comparison of the 2D and 3D twisted blade going through the effective VAT pitching motion

2D/3D	Max Twist	Re #	$C_{L,avg}$	$C_{D,avg}$	C_L/C_D
2D	N/A	25,000	0.252	0.0812	3.10
3D	20	25,000	0.891	0.224	3.99

The 2D blade shows a very low lift coefficient in comparison to the 3D twisted blade on which there is a large positive lift from θ = 0 to about 150°. For the remainder of the downstroke and the beginning of the upstroke there is negative lift. At θ = 200° the lift becomes positive again and remains so for the rest of the upstroke. The drag force shows an interesting trend. For the first half of the downstroke from θ = 0° to 100° the blade generates thrust. After this point there is a positive drag coefficient for the remainder of the cycle. At the end of the downstroke θ = 180°, there is a dip in the drag before another large positive peak that corresponds to the largest effective angle of attack at θ = 280°. Vorticity contours are shown for the 2D and 3D twisted blade and various points in the pitching cycle in Figure 4.14. For the 3D twisted blade slices are taken at the 10° plane to compare to the 2D blade.

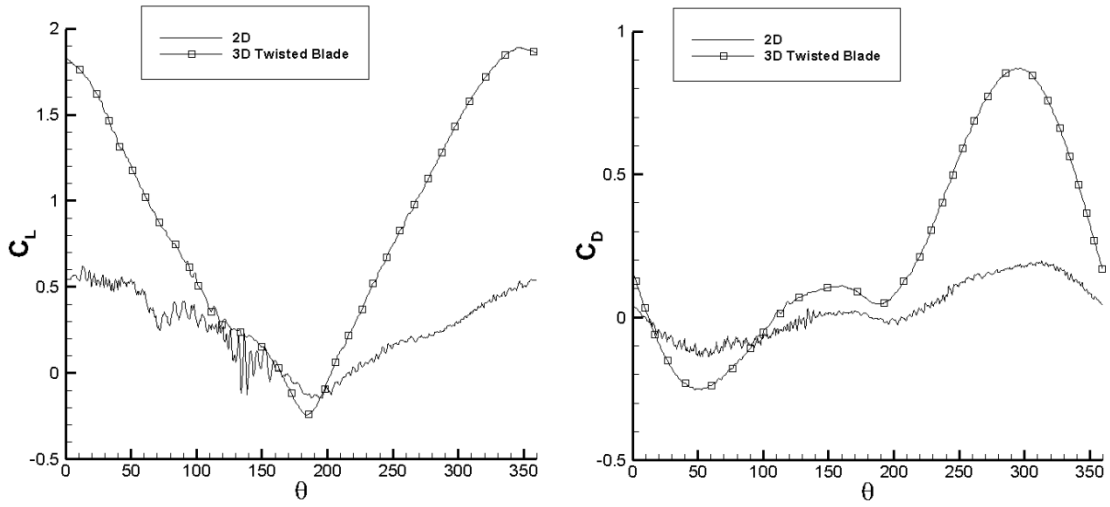

Figure 4.13. A comparison of the lift coefficient (left) and drag coefficient (right) for the 2D and 3D twisted blade going through the effective VAT pitching motion

At the start of the cycle both the 2D and 3D blades are at a positive angle of attack leading to a large lift force. The twisted blade's angle of attack increases along the span providing more lift further down the span with the flow still attached at this point. Both the 2D and 3D twisted blade shed trailing edge vortices and have a large wake. At $\theta = 90°$ there are leading edge vortices being generated in both cases. The twisted blade shows two vortices of large magnitude still attached near the trailing edge which could lead to a higher lift production. At the bottom of the downstroke ($\theta = 180°$) both blades are generating negative lift. The 2D blade has a large eddy that has detached from the blade at about c/2. The twisted blade shows detached flow as well but the eddy is much closer to the blade surface. At $\theta = 270°$ both blades are back at positive geometric angles of attack with positive lift being generated. Finally at the end of the cycle, both the 2D and 3D blades are at the end of the upstroke with similar flow as that seen at $\theta = 0°$. Both the 2D blade and the 10° slice of the twisted blade show a very similar flow. However the twisted blade generates much higher lift forces thought to be a result of much stronger vorticity that is generated in close proximity to the blade surface which augments positive force generation.

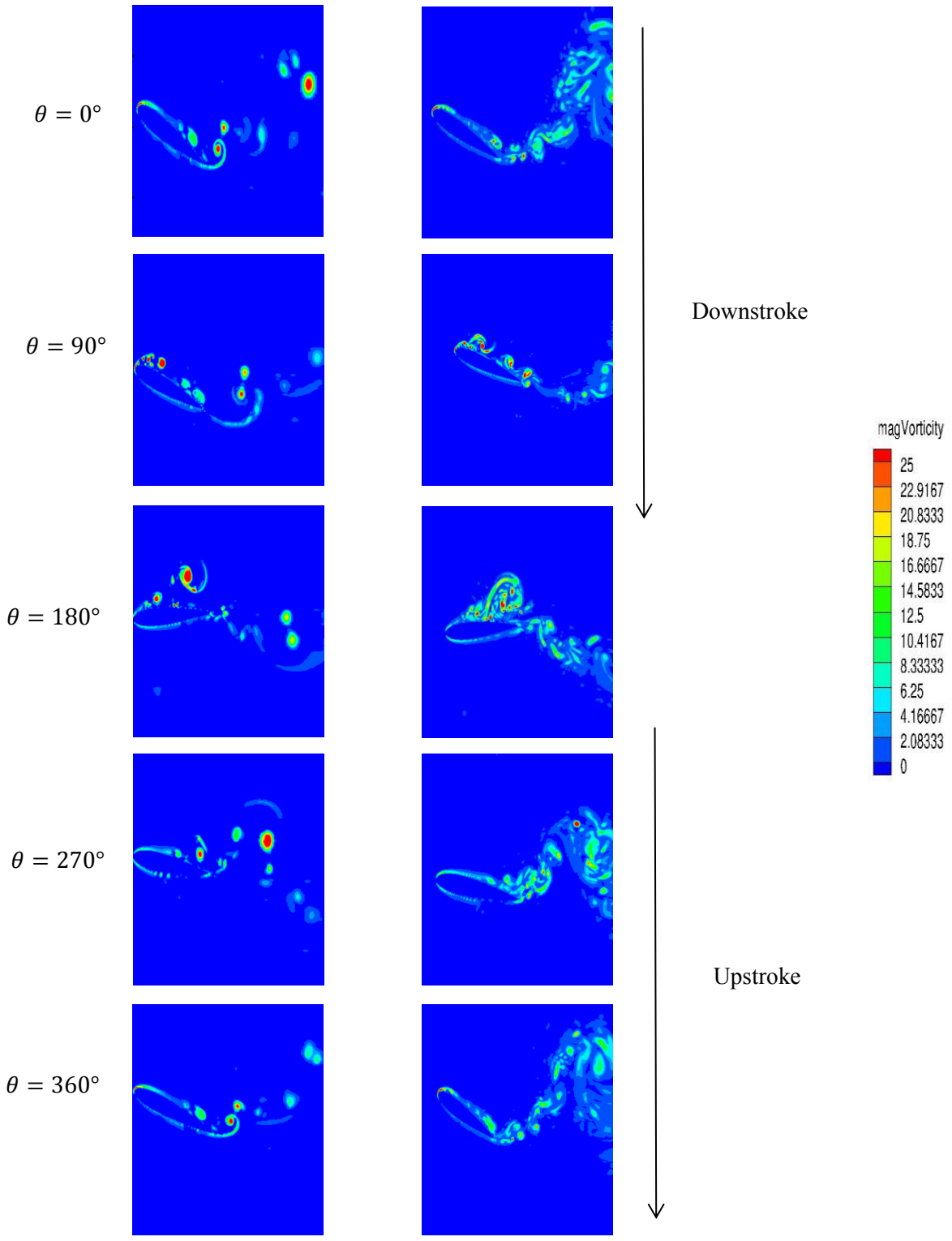

Figure 4.14. Comparing vorticity magnitude contours for the 2D (left) and 3D twisted (right) at the 10° plane at various stages of the effective VAT pitching motion

When the twisted blade was given an effective VAT pitching motion there is a large increase in the lift force and lift/drag ratio. However, when the blade was stationary it performed similar or worse than a static 2D blade at an angle of attack that was half the maximum twist angle of the blade. To determine why there was a performance increase, a comparison is done of the stationary twisted blade at a maximum twist of 20° and the twisted blade given the effective VAT pitching motion with a maximum twist angle of 20°. In Figure 4.15 are time-averaged pressure contours on the top and bottom surface of the static twisted blade. There is a large pressure force on the leading edge at the stagnation point. On the top surface of the blade there is an almost constant low pressure along the surface in the range -0.3 to -0.1. On the bottom of the blade there is a large positive pressure force (~0.3-0.5) near the leading edge that contributes to the lift. Further down the blade chord the pressure decreases to values between -0.3 to 0.1.

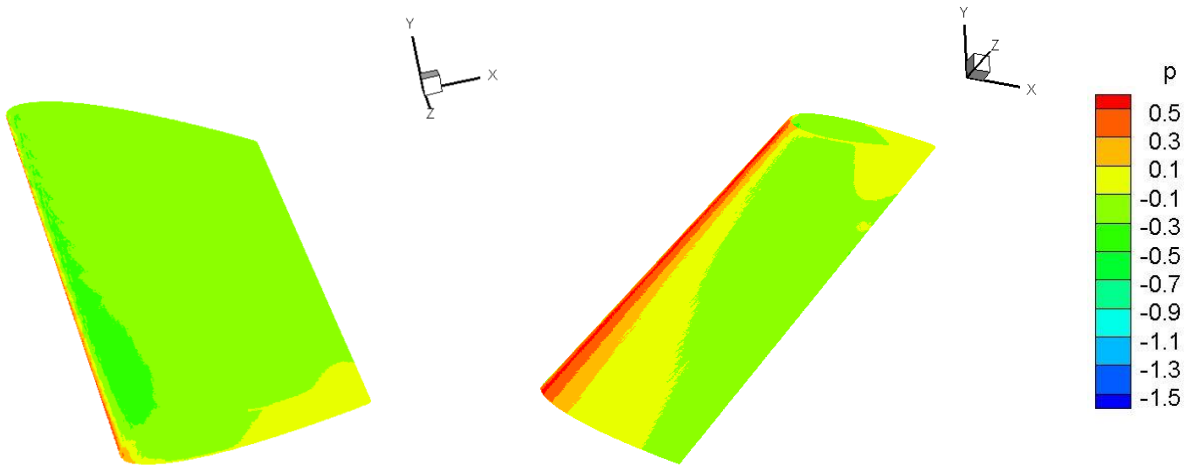

Figure 4.15. Pressure contours on the top surface (left) and bottom surface (right) of the static twisted blade with maximum twist angle 20°

Figure 4.16 shows streamlines colored by spanwise velocity over part of the downstroke and corresponding pressure contours on the top and bottom surfaces of the blade. During the downstroke a large vortex forms along almost the entire span of the blade. As the blade continues on the downstroke the vortex grows and the streamwise velocity becomes increasingly more negative. The negative spanwise flow helps to keep the vortex stable and attached to the surface and increases the lift production. The

vortex is the largest at the bottom of the downstroke and is near the trailing edge of the blade and begins to separate from the surface of the blade.

At $\theta = 45°$ the vortex is near the leading edge of the blade and causes a large negative pressure force on the top surface near the leading edge. This combined with the stagnation point being on the bottom surface of the blade due to the pitching motion gives a large pressure differential accounting for the large lift force at the start of the cycle. As the blade continues on the downstroke the vortex moves along the chord of the blade and with it, its pressure signature seen at $\theta = 90°$. The top surface of the blade still has a large negative pressure force due to the vortex at about c/2. The low pressure region due to the vortex allows the lift to stay positive through the downstroke. At the end of the downstroke/start of the upstroke ($\theta = 180°$), the vortex has separated from the blade almost entirely. Remnants of the votex pressure signature are still evident near the trailing edge of the blade on the top surface. At the same time, the bottom surface pressure reduces, largely accounting for the negative lift seen in this part of the cycle. As the blade proceeds into the upstroke, the lift force becomes positive again.

There is also a large positive lift force gained during the upstorke of the effective VAT pitching motion where there is no vortex formation on the top surface of the blade. The pressure contours at three different points during the upstroke can be see in Figure 4.17. Near the beginning of the upstroke at $\theta = 225°$, the effects of the vortex that had formed during the downstoke are only seen at the trailing edge. There is a low pressure seen on the bottom surface which accounts for the low lift coefficient seen at this point. As the uptroke continues the pressure on the top surface begins to decrease slightly at $\theta = 270°$. However, pressure on the bottom surface increases due to the increasing effective angle of attack at the 20º side of the blade. Near the end of the upstroke ($\theta = 335°$) the leading edge vortex is starting to form on the top surface of the blade, marked by the low pressure signature near the leading edge. This in combination with the large pressure seen on the bototm surface of the blade results in a large overall lift force near the end of the upstroke.

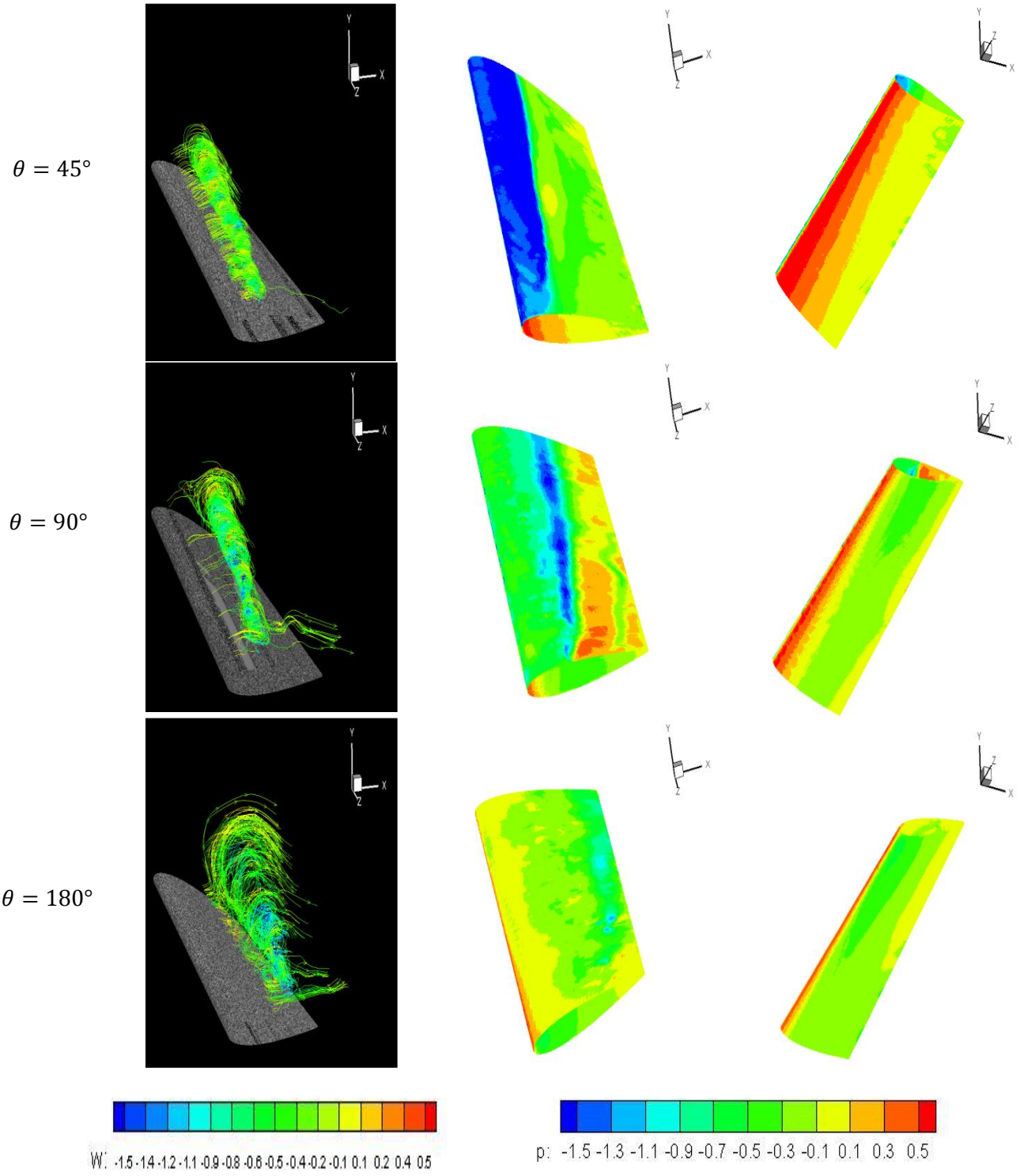

Figure 4.16. Streamlines colored by spanwise velocity and pressure distribution on the top and bottom surface of the blade during downstroke.

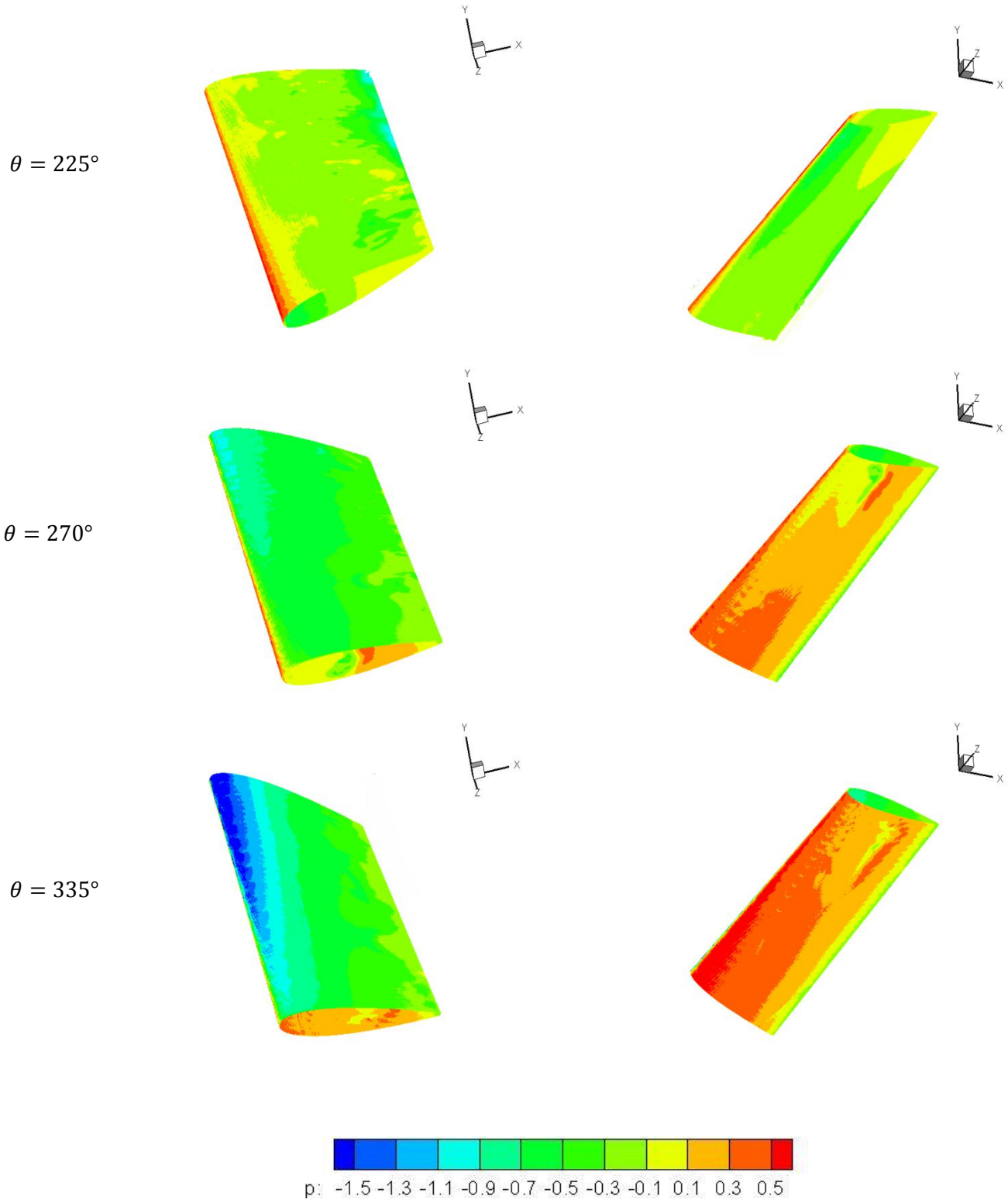

Figure 4.17. Pressure distribution on the top and bottom surface of the blade during the upstroke.

The main difference beteen the nominally 2D and 3D pitching airfoil is the vortices that form at the leading edge. Because of the 3D blade profile, the angle of attack varies along the span creating spiral vortex structures which are more stable than the nominally 2D vortices that are formed on a nominally 2D blade. It is hypothesized that the spiral structure induces a spanwise flow in the vortex and stabilizes it such that it remains coherent and induces a low pressure region on the blade surface. Judging from the performance of the static 3D twisted blade , the unsteadiness induced by the pitching motion is necessary for the blade to produce the stable leading edge vortices which are absent in the static case.

4.4 Conclusions

In an effort to reduce the negative impacts of dynamic stall and increase the efficiency of the VAT, the turbine blade profile was altered by twisting it along the span, thus changing the angle of attack. Three different blade profiles were tested in OpenFOAM using the k-ω SST RANS model and two profiles were tested with GenIDLEST using a LES with the dynamic Smagorinsky SGS model in a static setting. OpenFOAM showed a higher overall lift coefficient than the results from GenIDLEST while the drag coefficient was similar. The difference was found to be due to larger separation being predicted with GenIDLEST when results were time averaged for two time units. The results were compared with 2D static blades at an angle of attack that was half of the maximum twist angle of the twisted blades. It was shown that the stationary twisted blade had similar or worse performance in terms of lift and drag coefficients when compared to the 2D blades. To get a better representation of the impacts the twisted blade profile could have on VAT performance an effective VAT pitching motion was given to a blade with a maximum twist angle of 20°. This effective motion matched the VAT in terms of frequency and effective angle of attack, but differed from the VAT when comparing the relative velocity magnitude. The Reynolds number of the flow around the pitching blade was increased so that the average local Reynolds number the blade saw was the same for the VAT and pitching blade. The 3D twisted blade was compared to a 2D blade with the same effective VAT pitching motion and saw a 22% increase in the lift/drag ratio. To understand why the blade given the effective pitching motion performed better than the static blade,

surface contours of pressure were plotted. The stationary blade showed that there was a very small pressure differential accounting for the overall small lift coefficient of the blade. The pitching blade showed a large vortex forming on the surface of the blade during the downstroke. The vortex was characterized by a strong spanwise flow at the core which helped to stabilize the vortex during the downstroke and left a negative pressure signature that helped to increase the pressure differential on the blade surfaces. This also accounted for the large difference in the lift coefficient seen when comparing the 3D twisted blade to the 2D blade with the effective VAT pitching motion.

Chapter 5

Summary and Conclusions

In this thesis, the effects of the advance ratio, solidity, and downstream wake on the efficiency of a 2D vertical axis turbine (VAT) were investigated. 2D calculations of the VAT were completed in OpenFOAM at Re = 500,000 using the k-ω SST turbulence model. It was seen that when the turbine blades experienced dynamic stall there was a large negative impact on the efficiency of the turbine. In an effort to improve the performance of the turbine blades, the profile along the spanwise direction was altered to change the angle of attack. The flow over a static twisted blade was performed for different maximum twist angles at Re = 10,000. In an effort to see the effects of the twisted blade in a flow similar to that seen in a turbine, an effective pitching motion was then given to a blade with a maximum blade twist of 20°.

In Chapter 3, the effects of the advance ratio, solidity, and downstream wake were tested for a 2D VAT at Re = 500,000. It was found that as the advance ratio increased, the power coefficient increased until the blades experienced dynamic stall. To test solidity, the number of blades in the turbine were changed while keeping the advance ratio the same. The amount of power extracted per blade decreased with an increase in the number of blades, but overall the performance of the turbine increased due to a larger number of blades. Downstream wake effects were tested by increasing the radius of the VAT. The performance of the turbine in the second half of the cycle did not change with the radius where the wake effects would be the largest. However, there was a large impact in the first half due to trailing wakes of the blades impacting the flow. For all cases tested, the blades generate a large positive thrust that was slightly offset due to the negative impacts of the drag force in the tangential direction of the blades. When dynamic stall occurred (cases $\lambda = 2.5$ and $N = 4$) there was a large increase in the drag force produced that led to the drop in the overall efficiency of the turbine. When comparing the idealized relative velocity and ideal effective angle of attack to the actual values from the computations, there was found to be a deviation from the expected values in most cases. During the first half of the turbine there was relative good agreement for most cases, but in the second half there were dramatic differences seen due to the

blade interactions with the wakes. With the information and data the cause of dynamic stall was investigated for the cases of $\lambda = 2.5$ and $N = 4$. A single explanation for the onset of dynamic stall was not found and is thought to be due to a combination of the effective angle of attack, rotational velocity, and blade to blade complex interactions.

In Chapter 4, the profile of a turbine blade was altered by twisting it along the span, effectively changing the angle of attack along the span. This was done in an effort to reduce the effects of dynamic stall that was seen in Chapter 3. Stationary test were initially done in OpenFOAM and GenIDLEST and compared to 2D blades at equivalent angles as well. The results from OpenFOAM showed a significantly higher lift coefficient than what was seen in GenIDLEST. OpenFOAM showed a much larger lift coefficient in the presence of static stall when compared to experimental data, which is thought to be a major cause of the discrepancy between OpenFOAM and GenIDLEST. Both OpenFOAM and GenIDLEST did not show any improvement over the 2D blades that were at half of the maximum twist angle of the 3D twisted blades. To simulate the flow the blade would experience in a VAT, an effective motion was given to a twisted blade in GenIDLEST with a maximum twist angle of 20°. This effective motion matched the effective angle of attack and frequency of a turbine with an advance ratio of 2.5, but did not match the relative velocity magnitude profile. It was found that the 3D twisted blade performed much better than a 2D blade with the same motion. This was due in large part to positive lift being generated during the majority of the downstroke where the effective angle of attack was negative. A comparison of the flow structures and blade surface pressure over the static twisted blade and twisted blade with the effective VAT pitching motion was done to see why there was a large performance increase. It was found that a large helical vortex formed and was sustained on the surface of the blade during the entire duration of the downstroke that led to the positive lift generation.

In summary, the occurrence of dynamic stall was found to greatly reduce the overall efficiency of the VAT. An investigation into what caused the onset of dynamic stall was done, but a single cause could not be found. To reduce the negative effects of dynamic stall the blade profile was altered by twisting the blade along the span. This was found to greatly impact the performance of the blade when compared to a

2D blade when given an effective VAT pitching motion. Future work will focus on the cause of dynamic stall in a VAT and how the twisted blade profile can reduce the impact of dynamic stall.

Appendix A

Nomenclature

A	Turbine cross-sectional area, 2R
c	Blade chord
C_D	Drag coefficient
C_L	Lift coefficient
C_N	Normal force coefficient
C_p	Power Coefficient
C_T	Tangential force coefficient
C_τ	Torque coefficient
F_D	Drag Force
F_L	Lift Force
F_N	Normal Force
F_T	Tangential Force
$\vec{n}$	Normal vector
N	Number of blades
P	Power
R	Turbine radius
Re	Reynolds number
$\vec{t}$	Tangential vector
U_∞	Freestream velocity
V_{rel}	Relative velocity
Greek	
α	Angle of attack
θ	Azimuthal Angle
λ	Turbine advance ratio
ρ	Density

σ	Turbine solidity
τ	Torque
ω	Rotational velocity

Subscripts/Superscripts

D	Drag
eff	Effective angle of attack
geo	Geometric angle of attack
L	Lift
N	Normal
p	Power
rel	Relative
T	Tangential

Appendix B

Lift and Drag Component Calculation

Seen in Figure B.1 is decomposition of the x and y forces into lift and drag forces on the turbine blade along with the normal and tangential directions. The decomposition of the x and y forces into lift and drag can be seen in Equation B.1 and B.2 below. The lift and drag forces are then transferred to the tangential direction to see the impact on the turbine thrust production seen in Equations B.3 and B.4.

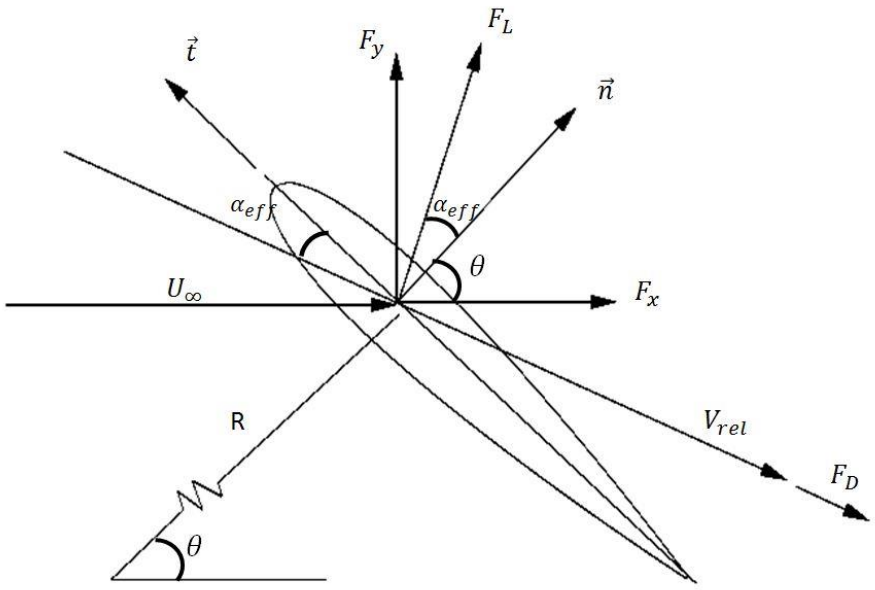

Figure B.1. Decomposition of x and y forces into lift and drag forces on a turbine blade

$$F_L = F_X Cos(\alpha_{eff} + \theta) + F_y Sin(\alpha_{eff} + \theta) \quad \textbf{Equation B.1}$$

$$F_D = F_X Sin(\alpha_{eff} + \theta) - F_y Cos(\alpha_{eff} + \theta) \quad \textbf{Equation B.2}$$

$$F_{T,Lift} = F_L Sin(\alpha_{eff}) \quad \textbf{Equation B.3}$$

$$F_{T,Drag} = -F_D Cos(\alpha_{eff}) \quad \textbf{Equation B.4}$$

Appendix C

Comparing Results from Ideal Effective Angle of Attack and the Actual Effective Angle of Attack

C.1 Advance ratio results comparing the ideal and actual effective angle of attack

In Figure C.1.1 is the comparison between the lift coefficients and lift force as well as the drag coefficient and drag force for the ideal and actual effective angle of attack for a single blade. Both the lift coefficient and lift force show the same trend for the ideal and actual effective angle of attack. The actual effective angle of attack shows a slightly higher lift coefficient and lift force than the ideal case. The largest difference is seen at $\lambda = 1.0$ where the largest difference between the ideal and actual effective angle of attack was seen. The drag coefficient shows a good comparison between the ideal and actual effective angle of attack with a large difference for $\lambda = 1.0$. The actual drag force for $\lambda = 1.0$ is much lower (about 1/3) than what is predicted from the ideal drag force. While the actual drag force for $\lambda = 2.5$ is slightly higher than what is predicted from the ideal drag force.

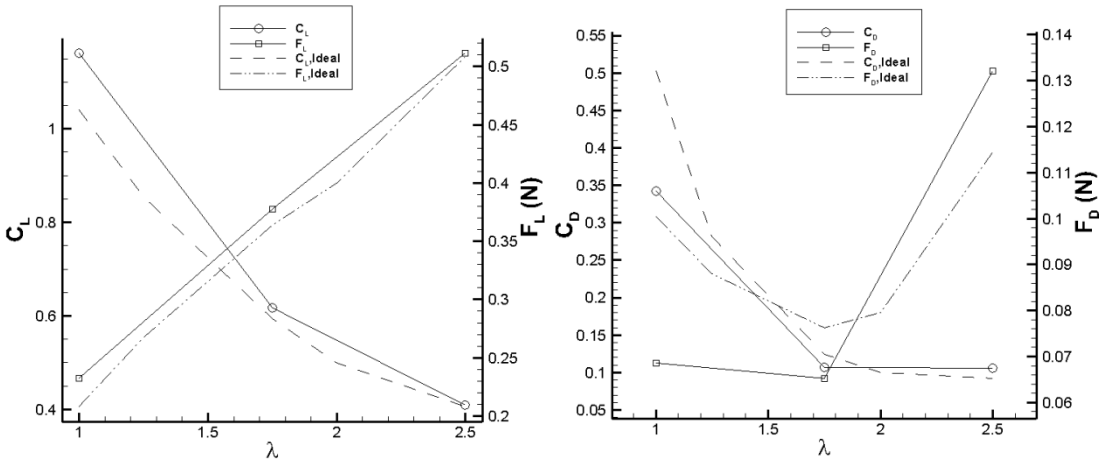

Figure C.1.1. The cycle averaged lift (left) and drag (right) for a single blade using the ideal and actual effective angle of attack

In Figure C.1.2 the components of lift and drag forces in the tangential direction and total tangential is compared using the ideal and actual effective angle of attack. For the lift, drag and total force the ideal effective angle of attack shows very good comparison with the actual effective angle of attack for the different advance ratios.

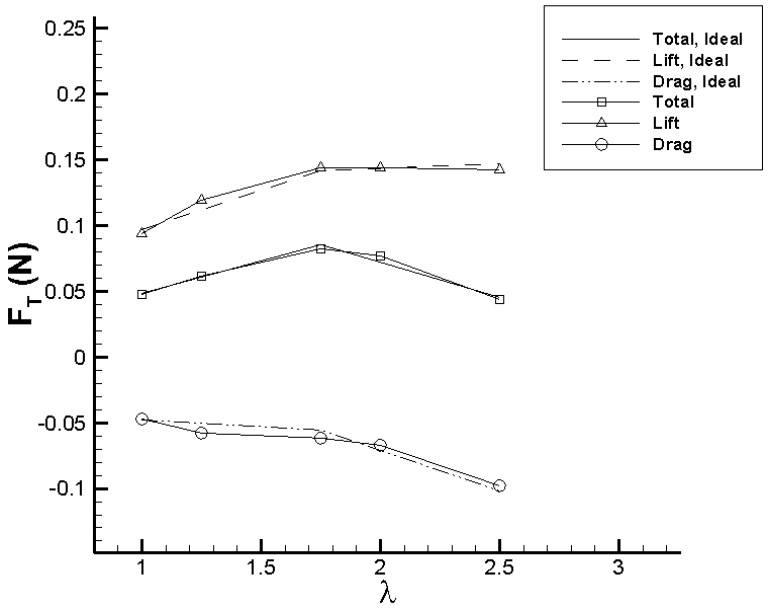

Figure C.1.2. The cycle averaged components of lift and drag forces in the tangential direction and total tangential force using the ideal and actual effective angle of attack

In Figure C.1.3 the lift component of the tangential force is compared using the ideal and actual effective angle of attack. There is good comparison in the first half of the turbine between the two effective angles of attack used for $\lambda = 1.75$ and $\lambda = 2.5$. There is an over prediction in the peak lift component for $\lambda = 1.0$ occurring at $\theta = 160°$ due to the large difference between the ideal and effective angle of attack. In the second half of the turbine there is good agreement between the two effective angles of attack.

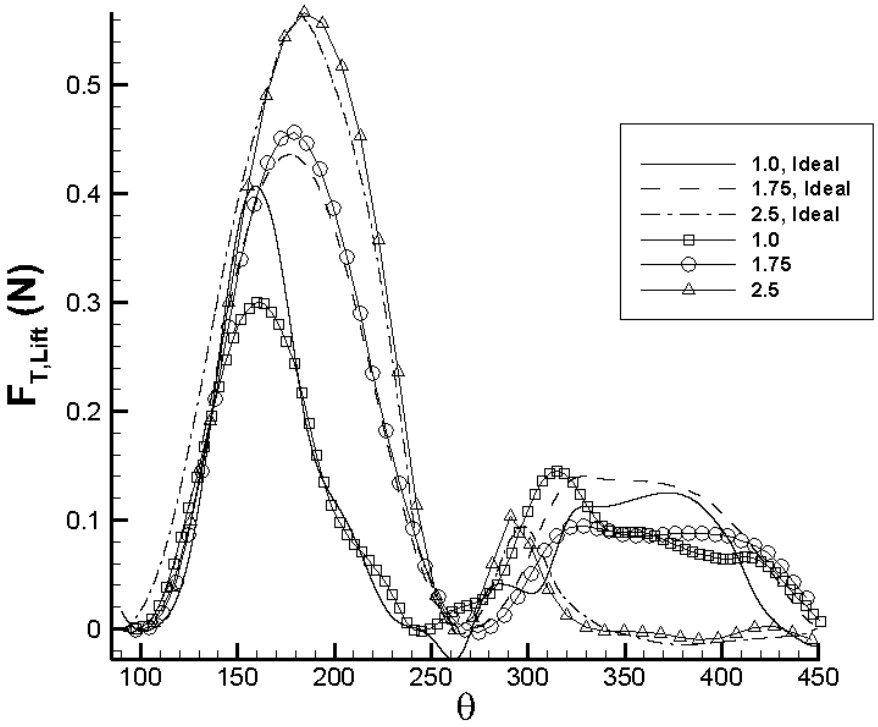

Figure C.1.3.The lift component of thrust force in the tangential direction throughout the cycle using the ideal and actual effective angle of attack

In Figure C.1.4 the drag component of the tangential force is compared using the ideal and actual effective angle of attack. As was the case with the lift component, there is good agreement between the drag calculated with the ideal and actual effective angle of attack. For $\lambda = 2.5$ the ideal case under predicts the negative impact that dynamic stall has on the thrust force generated at $\theta = 200°$. In the second half of the turbine there is good agreement between the two effective angles of attack. For $\lambda = 2.5$ there is a positive peak of the drag component occurring at $\theta = 360°$. This is not seen when using the ideal effective angle of attack and is thought to occur due to the separated vortices traveling downstream and interacting with the blade.

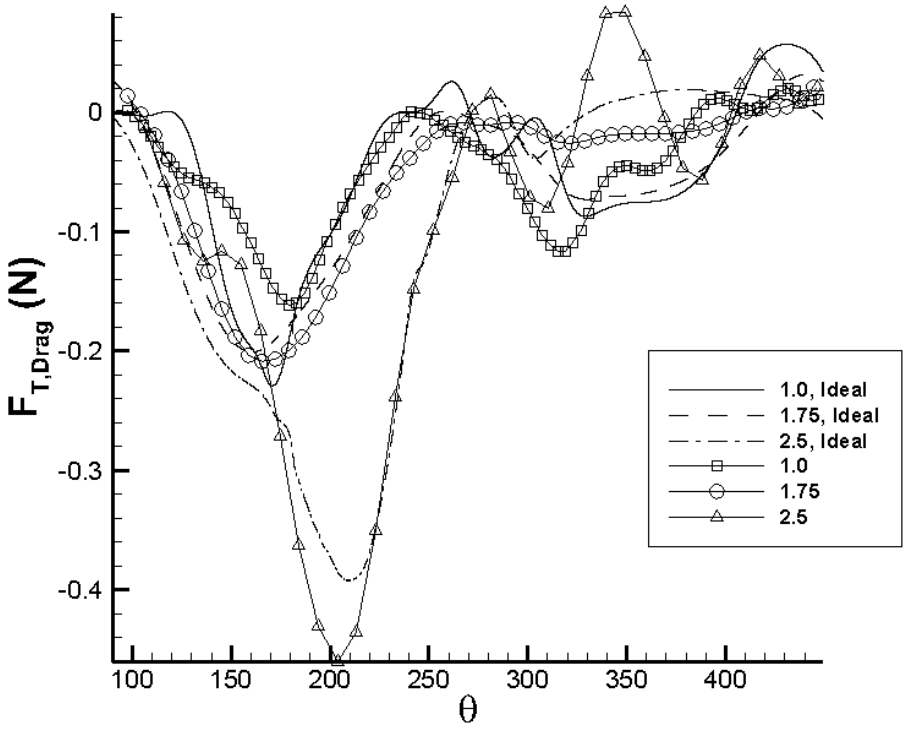

Figure C.1.4.The drag component of thrust force in the tangential direction throughout the cycle using the ideal and actual effective angle of attack

C.2 Solidity results comparing the ideal and actual effective angle of attack

In Figure C.2.1 is the comparison between the lift coefficients and lift force as well as the drag coefficient and drag force for the ideal and actual effective angle of attack for a single blade. Both the lift force and coefficient show the same trends for the ideal and effective angle of attack. The actual effective angle of attack does predict slightly higher forces. The drag coefficient and force trends are different between the ideal and actual effective angle of attack, most notably for N = 4. The ideal effective angle of attack predicts the highest overall drag coefficient of about 0.2. On the other hand, the actual effective angle of attack predicts the lowest average drag coefficient of about 0.02. This is due to the large difference seen in the ideal and actual effective angle of attack for the case of N = 4. The actual drag coefficient and drag force are also about two times larger for N = 6.

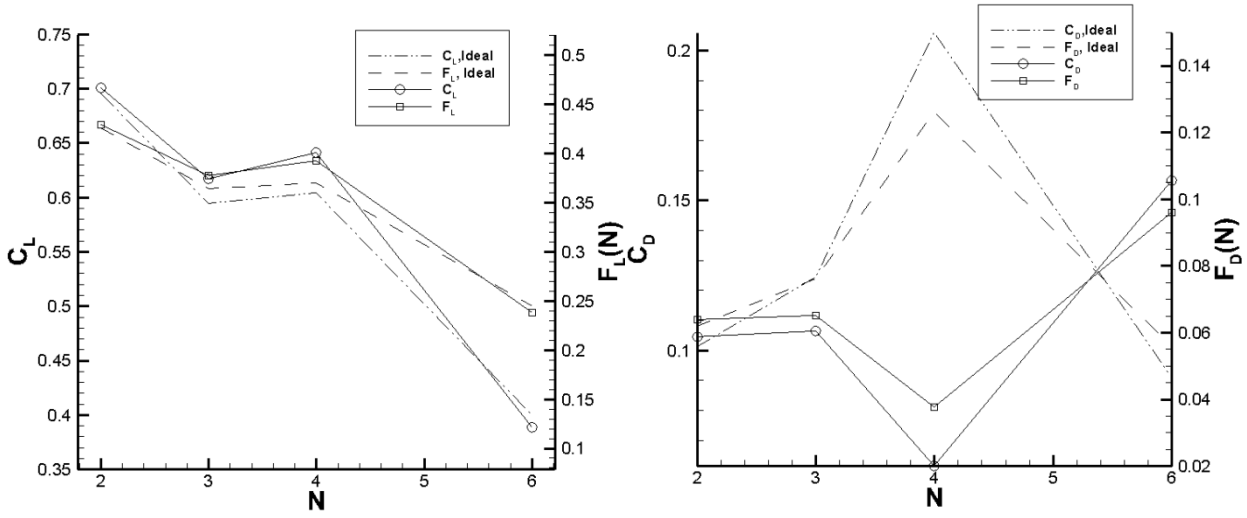

Figure C.2.1. The cycle averaged lift (left) and drag (right) for a single blade using the ideal and actual effective angle of attack

In Figure C.2.2 the components of lift and drag forces in the tangential direction and total tangential is compared using the ideal and actual effective angle of attack. There is good comparison for both the lift and drag component for all of the cases except N = 4. There is a much smaller lift force shown and smaller negative impacts of the drag force. The total thrust force predicted for the ideal and actual effective angle of attack shows very good comparison however.

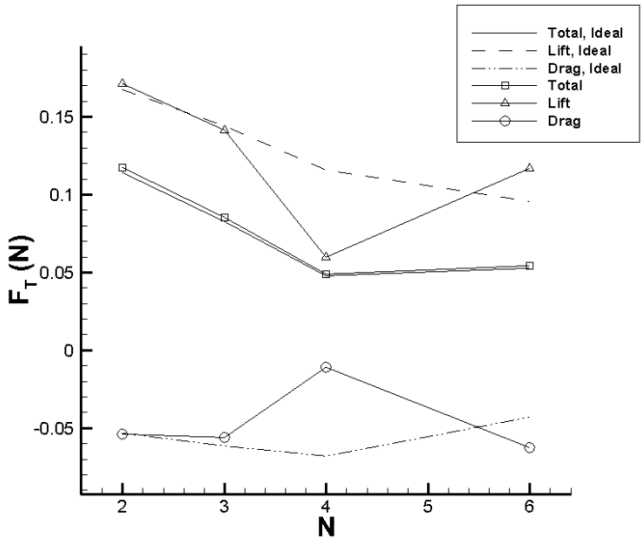

Figure C.2.2. The cycle averaged components of lift and drag forces in the tangential direction and total tangential force using the ideal and actual effective angle of attack

In Figure C.2.3 the lift component of the tangential force is compared using the ideal and actual effective angle of attack. In the first half of the cycle there is reasonably good comparison for the lift component for N = 2, 3, and 6.For N = 4 the ideal effective angle of attack largely over predicts the peak lift force in the tangential direction by almost two times. In the second half of the cycle there is a slight peak at θ = 310° that matches the trend of the ideal effective angle of attack. The negative peak seen at θ = 340° for the ideal effective angle of attack is not replicated for the actual effective angle of attack. These differences account for the difference seen for the lift component in Figure B.6 for N = 4. All other cases show good comparison in the second half of the cycle.

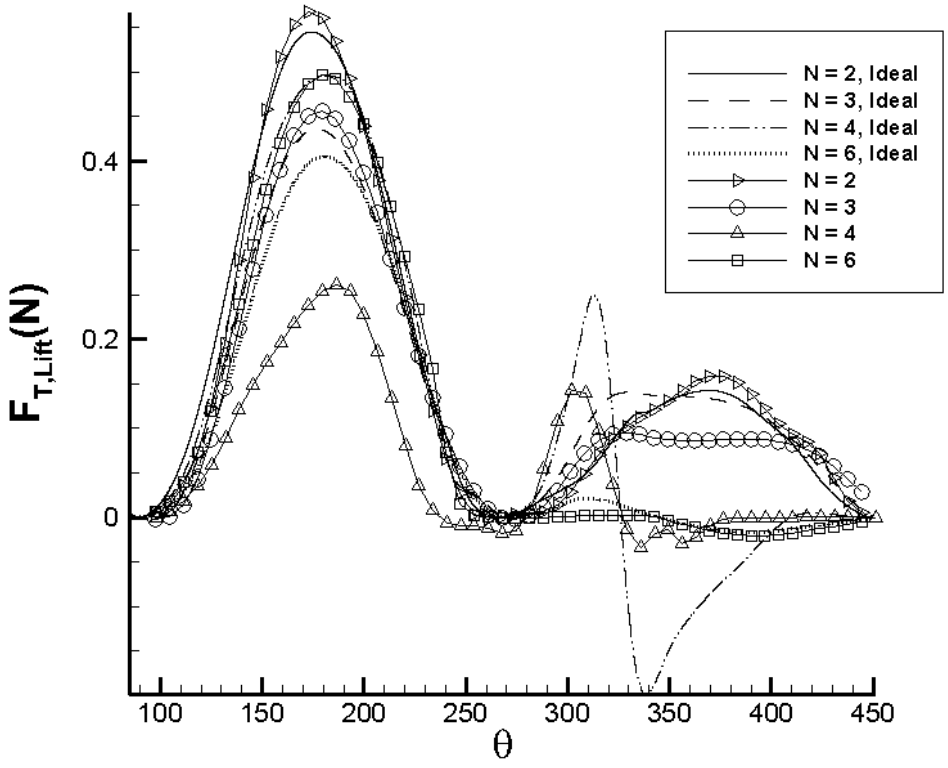

Figure C.2.3.The lift component of thrust force in the tangential direction throughout the cycle using the ideal and actual effective angle of attack

In Figure C.2.4 the drag component of the tangential force is compared using the ideal and actual effective angle of attack. N = 4 shows a very different profile from the ideal effective angle of attack. There is no large negative peak followed by a second peak due to the occurrence of dynamics stall. Instead, the drag component fluctuates throughout the cycle and for some parts contributes to a positive thrust force. This difference is due to the large difference seen in the ideal and actual effective angles of attack. It is clear that N = 4, the wakes of the blades disturb the approach flow. This also accounts for the small negative average drag component of the tangential force seen in Figure B.6. The other cases show good comparison throughout the cycle with the peak for N = 6 under predicted at θ = 170°.

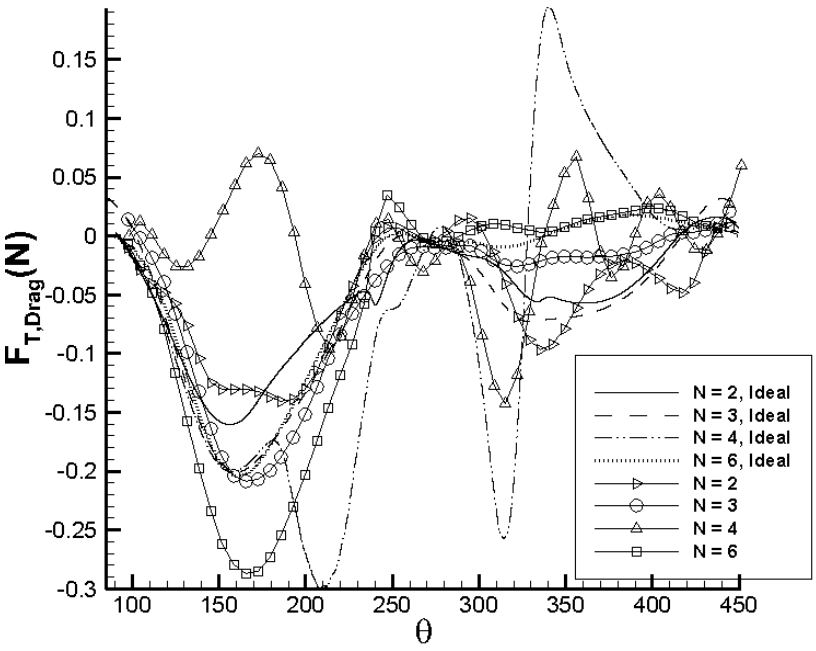

Figure C.2.4.The drag component of thrust force in the tangential direction throughout the cycle using the ideal and actual effective angle of attack

C.3 Downstream wake results comparing the ideal and actual effective angle of attack

In Figure C.3.1 is the comparison between the lift coefficients and lift force as well as the drag coefficient and drag force for the ideal and actual effective angle of attack for a single blade. The lift force compares very well between the ideal and actual effective angle of attack. The actual lift coefficient shows the same trend as the ideal lift coefficient, but if slightly higher for all values of R. The drag force from the actual effective angle of attack shows a similar trend with smaller forces. The largest difference occurring for R = 2.95 where the actual drag force seen is almost half the ideal drag force. The drag coefficient is much lower for all values of R. While the ideal drag coefficient shows an almost linear trend, the actual has a peak for R = 1.475 and then a large from at R = 2.95. These differences are due to the difference in the ideal and actual effective angle of attack.

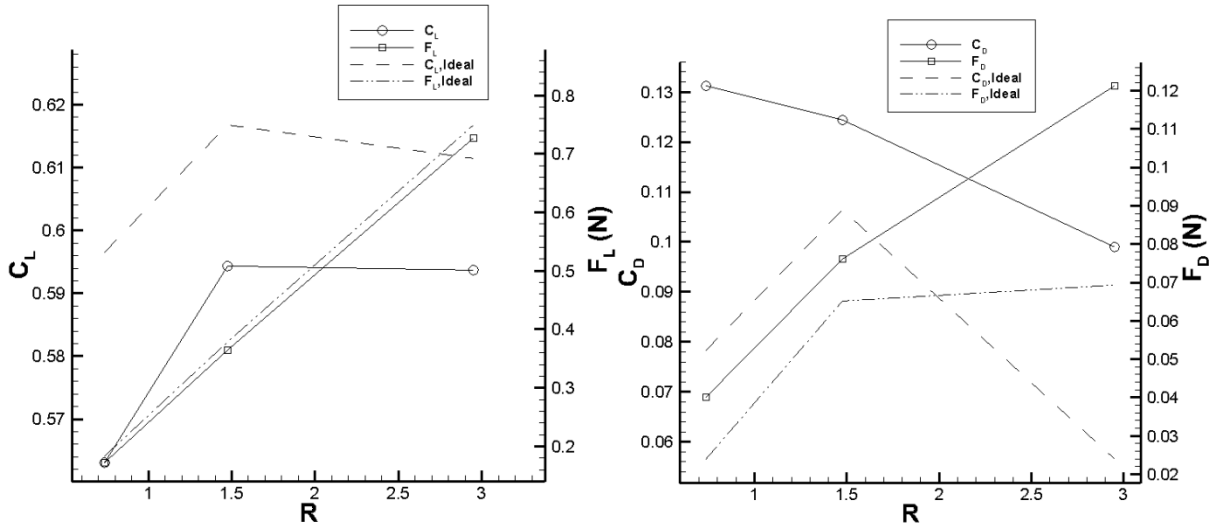

Figure C.3.1. The cycle averaged lift (left) and drag (right) for a single blade using the ideal and actual effective angle of attack

In Figure C.3.2 the components of lift and drag forces in the tangential direction and total tangential is compared using the ideal and actual effective angle of attack. The lift and drag component as well as the total force show a good comparison between the ideal and actual effective angle of attack. There is slightly lower lift force shown that what was predicted by the ideal effective angle of attack, and

smaller in magnitude drag component. The total force shows an almost exact comparison between the two effective angles of attack used.

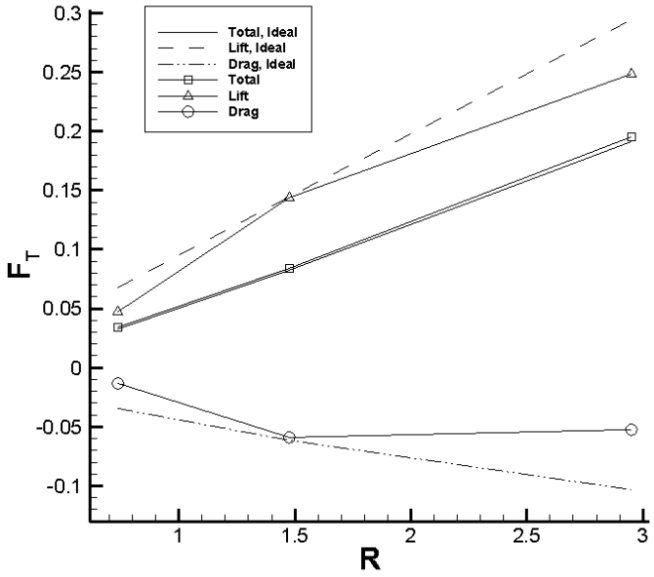

Figure C.3.2. The cycle averaged components of lift and drag forces in the tangential direction and total tangential force using the ideal and actual effective angle of attack

In Figure C.3.3 the lift component of the tangential force is compared using the ideal and actual effective angle of attack. In the first half of the cycle the ideal effective angle of attack under predicts the lift force seen for both R = 0.7375 and R = 2.95. For R = 0.7375 the actual lift force seen is 1/3 what the ideal effective angle of attack predicted. In the second half of the cycle there is good comparison between the two effective angles of attack with a slight over prediction for R = 2.95 starting at $\theta = 330°$.

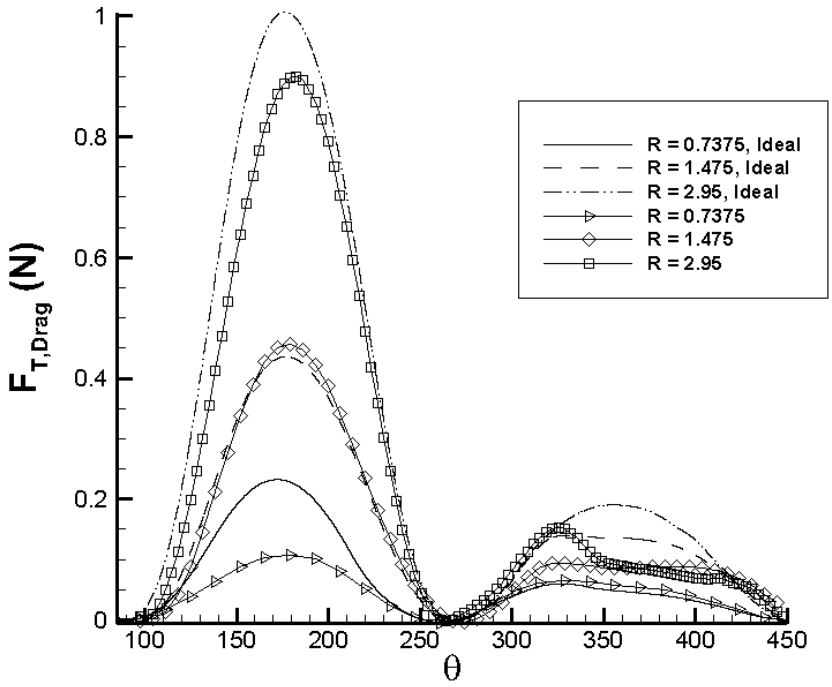

Figure C.3.3.The lift component of thrust force in the tangential direction throughout the cycle using the ideal and actual effective angle of attack

In Figure C.3.4 the drag component of the tangential force is compared using the ideal and actual effective angle of attack. There is a large difference between the peaks seen at $\theta = 160°$ for R = 0.7375 and R = 2.95. For R = 0.7375 instead of a negative peak there is a positive impact to thrust. For R = 2.95 the peak is over estimated by two times what was seen for the actual effective angle of attack. In the second half of the cycle the ideal effective angle of attack over predicts the negative impact of the drag force on thrust for R = 1.475 and R = 2.95, but shows good comparison with R = 0.7375. This is due to the large difference seen in the ideal and actual effective angle of attack. In the first half of the cycle R = 0.7375 shows bad comparison with the ideal effective angle of attack and good comparison in the second half. The opposite was show true for R = 1.475 and R = 2.95.

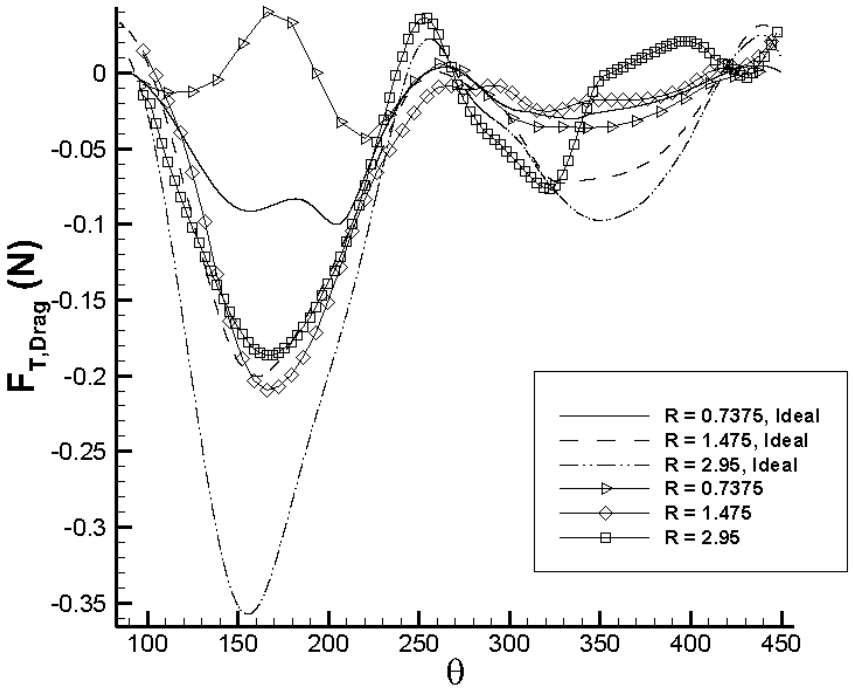

Figure C.3.4.The drag component of thrust force in the tangential direction throughout the cycle using the ideal and actual effective angle of attack

References

[1] Agency, I. E. (2014). World Energy Outlook 2014, Executive Summary.

[2] Rourke, F. O., Boyle, F., & Reynolds, A. (2010). Tidal energy update 2009. Applied Energy, 87(2), 398–409. http://doi.org/10.1016/j.apenergy.2009.08.014

[3] Iida, A., Mizuno, A., & Fukudome, K. (2004). Numerical Simulation of Aerodynamic Noise Radiated form Vertical Axis Wind Turbines. In 18th International Congress on Acoustics (pp. 1–4).

[4] Eriksson, S., Bernhoff, H., & Leijon, M. (2008). Evaluation of different turbine concepts for wind power. Renewable and Sustainable Energy Reviews, 12, 1419–1434. http://doi.org/10.1016/j.rser.2006.05.017

[5] Mertens, S., & Bussel, G. Van. (2003). Performance of an H-Darrieus in the Skewed Flow on a Roof 1. Wind Engineering, 125(November). http://doi.org/10.1115/1.1629309

[6] Kirke, B., & Lazauskas, L. (2008). Variable Pitch Darrieus Water Turbines. Journal of Fluid Science and Technology, 3(3), 430–438. http://doi.org/10.1299/jfst.3.430

[7] Kjellin, J., Bülow, F., Eriksson, S., Deglaire, P., Leijon, M., & Bernhoff, H. (2011). Power coefficient measurement on a 12 kW straight bladed vertical axis wind turbine, 36, 3050–3053. http://doi.org/10.1016/j.renene.2011.03.031

[8] Ferreira, C., Kuik, G. van, Bussel, G. van, & Scarano, F. (2009). Visualization by PIV of dynamic stall on a vertical axis wind turbine. Experimental Fluids, 97–108. http://doi.org/10.1007/s00348-008-0543-z

[9] Ferreira, C. J. S., Zuijlen, A. Van, Bijl, H., Bussel, G. Van, & Kuik, G. Van. (2010). Simulating dynamic stall in a two-dimensional vertical-axis wind turbine : verifi cation and validation with particle image velocimetry data, (May 2009), 1–17. http://doi.org/10.1002/we

[10] Takao, M., Kuma, H., Maeda, T., Kamada, Y., Oki, M., & Minoda, A. (2009). A straight-bladed vertical axis wind turbine with a directed guide vane row — Effect of guide vane geometry on the performance —. Journal of Thermal Science, 18(1), 54–57. http://doi.org/10.1007/s11630-009-0054-0

[11] Armstrong, S., Fiedler, A., & Tullis, S. (2012). Flow separation on a high Reynolds number, high solidity vertical axis wind turbine with straight and canted blades and canted blades with fences. Renewable Energy, 41, 13–22. http://doi.org/10.1016/j.renene.2011.09.002

[12] Templin, R. J. (1976). Aerodynamic performance theory for the NRC vertical-axis wind turbine. NRC Lab. report, NASA STI/Recon Technical Report N, 76-16618.

[13] Wilson, R. E., & Lissaman, P. B. S. (1974). Applied aerodynamics of wind power machhines. Oregon State University Corvallis.

[14] Paraschivoiu, I. (1988). Double-multiple streamtube model for studying vertical-axis wind turbines. Journal of Propulsion and Power, 4(4), 370–377. http://doi.org/10.2514/3.23076

[15] Bianchini, A., Carnevale, E. a., & Ferrari, L. (2011). A Model to Account for the Virtual Camber Effect in the Performance Prediction of an H-Darrieus VAWT Using the Momentum Models. Wind Engineering, 35(4), 465–482. http://doi.org/10.1260/0309-524X.35.4.465

[16] Rathi, D. (2012). Performance Prediction and Dynamic Model Analysis of Vertical Axis Wind Turbine Blades with Aerodynamically Varied Blade Pitch.

[17] Larsen, H. (1975). Summary of a vortex theory for the cyclogiro. In the second US national conferences on wind engineering research, Colorado State University

[18] Strickland, J. H., Webster, B. T., & Nguyen, T. (1979). A Vortex Model of the Darrieus Turbine: An Analytical and Experimental Study. Journal of Fluids Engineering, 101(4), 500. http://doi.org/10.1115/1.3449018

[19] Cardona, J. L. (1984). Flow curvature and dynamic stall simulated with an aerodynamic free-vortex model for VAWT. Wind Engineering, 8, 135–143.

[20] Wang, L. B., Zhang, L., & Zeng, N. D. (2007). A potential flow 2-D vortex panel model: Applications to vertical axis straight blade tidal turbine. Energy Conversion and Management, 48(2), 454–461. http://doi.org/10.1016/j.enconman.2006.06.017

[21] Almohammadi, K. M., Ingham, D. B., Ma, L., & Pourkashan, M. (2013). Computational fluid dynamics (CFD) mesh independency techniques for a straight blade vertical axis wind turbine. Energy, 58, 483–493. http://doi.org/10.1016/j.energy.2013.06.012

[22] Balduzzi, F., Bianchini, A., Maleci, R., Ferrara, G., & Ferrari, L. (2016). Critical issues in the CFD simulation of Darrieus wind turbines. Renewable Energy, 85, 419–435. http://doi.org/10.1016/j.renene.2015.06.048

[23] Balduzzi, F., Ferrara, G., Bianchini, A., Campobasso, M. S., & Gigante, F. A. (2015). Parametric and Comparative Assessment of Navier-Stokes CFD Methodologies for Darriues Wind Turbine Performance Analysis, 1–12.

[24] Castelli, M. R., Ardizzon, G., Battisti, L., Benini, E., & Pavesi, G. (2010). Modeling Strategy and Numerical Validation for a Darrieus Vertical Axis Micro-Wind Turbine. In ASME 2010 International Mechanical Engineering Congress and Exposition (pp. 1–10).

[25] Castelli, M., Betta, S. De, & Bernini, E. (2012). Effect of Blade Number on a Straight-Bladed Vertical Axis Wind Turbine. World Academy of Science, Engineering and Technology, 61, 305–311.

[26] Benedict, M. (2012). Experimental and Computational Studies to Understand the Role of Flow Curvature Effects on the Aerodynamic Performance of a MAV-Scale Cycloidal Rotor in Forward Flight (pp. 1–30).

[27] Fagley, C., Porter, C., & Mclaughlin, T. (2014). Curvature Effects of a Cycloidally Rotating Airfoil. AIAA, (January), 1–14.

[28] Benedict, M., Lakshminarayan, V., Pino, J., & Chopra, I. (2013). Fundamental Understanding of the Physics of a Small-Scale Vertical Axis Wind Turbine with Dynamic Blade Pitching: An Experimental and Computational Approach. 54th AIAA/ASME/ASCE/AHS/ASC Structures, Structural Dynamics, and Materials Conference, 1–21. http://doi.org/10.2514/6.2013-1553

[29] Carrigan, T. J., Dennis, B. H., Han, Z. X., & Wang, B. P. (2012). Aerodynamic Shape Optimization of a Vertical-Axis Wind Turbine Using Differential Evolution. ISRN Renewable Energy, 2012, 1–16. http://doi.org/10.5402/2012/528418

[30] Chen, Y., & Lian, Y. (2015). Mechanics Numerical investigation of vortex dynamics in an H-rotor vertical axis wind turbine, 2060(December), 20–32. http://doi.org/10.1080/19942060.2015.1004790

[31] Gosselin, R., Dumas, G., & Boudreau, M. (2013). Parametric study of H-Darrieus vertical-axis turbines using uRANS simulations. In 21st Annual Conference of the CFD Society of Canada (p. 16). Sherbrooke, Canada. Retrieved from http://www.lmfn.ulaval.ca/fileadmin/lmfn/documents/Articles/GosselinDumasBoudreau-CFD2013_reprint.pdf

[32] Howell, R., Qin, N., Edwards, J., & Durrani, N. (2010). Wind tunnel and numerical study of a small vertical axis wind turbine. Renewable Energy, 35(2), 412–422. http://doi.org/10.1016/j.renene.2009.07.025

[33] Liang, L. X. Z. Y. B., Jiao, X. H. L. Q. F., & Guo, J. (2012). Aerodynamic Performance Prediction of Straight-bladed Vertical Axis Wind Turbine Based on CFD, 2013.

[34] Tsai, H., & Colonius, T. (n.d.). Coriolis Effect on Dynamic Stall in a Vertical Axis Wind Turbine at Moderate Reynolds Number.

[35] Weller, H. G., & Tabor, G. (1998). A tensorial approach to computational continuum mechanics using object-oriented techniques. Computers in Physics, 12(6), 620–631. http://doi.org/10.1063/1.168744

[36] Wolfgang, V., Esch, T., & Menter, F. (2002). Heat Transfer Predictions using Advanced Two-Equation Turbulence Models.

[37] OpenFOAM guide/The PIMPLE algorithm in OpenFOAM. (2015, September 1). Retrieved December13,2015,from https://openfoamwiki.net/index.php/OpenFOAM_guide/The_PIMPLE_algorithm_in_OpenFOAM

[38] PimpleDyMFoam. (2014, May 15). Retrieved December 13,2015,from https://openfoamwiki.net/index.php/PimpleDyMFoam

[39] Farrell, P. E., & Maddison, J. R. (2011). Conservative interpolation between volume meshes by local Galerkin projection. Computer Methods in Applied Mechanics and Engineering, 200(1-4), 89–100. http://doi.org/10.1016/j.cma.2010.07.015

[40] Tafti, D. K., 2001, "GenIDLEST - A scalable parallel computational tool for simulating complex turbulent flows," Proceedings of the ASME Fluids Engineering Division (FED), ASME-IMECE, p. Vol.256.

[41] Tafti, D. K., 2011, "Time-accurate techniques for turbulent heat transfer analysis in complex geometries, Advances in Computational Fluid Dynamics and Heat Transfer," Developments in Heat Transfer, R. Amano, and B. Sunden, eds., WIT PRESS.

[42] Nagendra, K., Tafti, D. K., and Viswanath, K., 2014, "A new approach for conjugate heat transfer problems using immersed boundary method for curvilinear grid based solvers," Journal of Computational Physics, 267, pp. 225–246.

[43] Gilmanov, A., and Sotiropoulos, F., 2005, "A hybrid Cartesian/immersed boundary method for simulating flows with 3D, geometrically complex, moving bodies," Journal of Computational Physics, 207(2), pp. 457–492.

[44] He, L. (2014). A study of Immersed Boundary Method in a Ribbed Duct for the Internal Cooling of Turbine Blades. Virginia Tech.

[45] Sheldahl, R. E., & Klimas, P. C. (1981). Aerodynamic characteristics of seven symmetrical airfoil sections through 180-degree angle of attack for use in aerodynamic analysis of vertical axis wind turbines. Chemistry &, SAND80-211, 118. http://doi.org/10.2172/6548367

[46] Mccroskey, W. J. (1981). The Phenomenon of Dynamic Stall.